LA-10689-PR
Progress Report
UC-3

Los Alamos National Laboratory is operated by the University of California for the United States Department of Energy under contract W-7405-ENG-36

Applied Nuclear Science Research and Development Progress Report

June 1, 1985–November 30, 1985

Los Alamos
Los Alamos National Laboratory
Los Alamos, New Mexico 87545

The four most recent reports in this series, unclassified, are LA-9841-PR, LA-10069-PR, LA-10288-PR, and LA-10513-PR.

This work was performed under the auspices of the US Department of Energy's Division of Reactor Research and Technology, Office of Basic Energy Sciences, and Office of Fusion Energy.

LA-10689-PR
Progress Report

UC-34C
Issued: April 1986

Applied Nuclear Science Research and Development Progress Report

June 1, 1985—November 30, 1985

Compiled by
E. D. Arthur
A. D. Mutschlecner

Los Alamos
Los Alamos National Laboratory
Los Alamos, New Mexico 87545

CONTENTS

CONTENTS (Cont.)

APPLIED NUCLEAR SCIENCE RESEARCH AND DEVELOPMENT
PROGRESS REPORT

June 1, 1985-November 30, 1985

Compiled by

E. D. Arthur and A. D. Mutschlecner

ABSTRACT

This progress report describes the activities of the Los Alamos Applied Nuclear Science Group for June 1, 1985 through November 30, 1985. The topical content is summarized in the Contents.

I. THEORY AND EVALUATION OF NUCLEAR CROSS SECTIONS

A. Low-Energy Transitions for Polarized d+d Reactions [G. Hale, H. Hofmann (Institut für Theoretische Physik, Universität Erlangen, W. Germany)]

The question of whether the d+d reactions can be suppressed at low energies by polarizing the deuterons spin-parallel, which is of great interest for advanced fusion concepts, centers on knowing the magnitudes of the $^5S_2$ transitions in the reactions. Liu, Zhang, and Shuy[1] claim, based on DWBA calculations, that they are small, resulting in high suppression. The R-matrix fits to the data[2] and resonating group calculations[3] that we have done independently give relatively large $^5S_2$ transitions, resulting in little suppression. We are continuing our efforts to understand the latter results in terms of the existing experimental data and improved resonating group calculations.

The Legendre polynomial expansion for the analyzing tensors of the d+d reactions in terms of transition matrix elements and angular momentum coupling coefficients (3j and 9j symbols) reveals that the second-rank tensors T_{2M} depend at low energies only on contributions from the $^5S_2$ (not $^1S_0$) and ^3P_J transitions, and that these contributions have opposite signs.[4] Thus, nonzero values of T_{2M} at low energies suggest the presence of $^5S_2$ transitions, and their signs

are a strong indicator of whether the S- or P-wave transitions dominate. In Fig. 1, which shows R-matrix calculations for $\frac{1}{2}(A_{xx}-A_{yy})\sim T_{22}$ both with (solid curve) and without (dashed curve) the $^5S_2$ transitions, one sees that the low-energy data of Ad'yasevich[5] require the presence of dominant $^5S_2$ transitions.

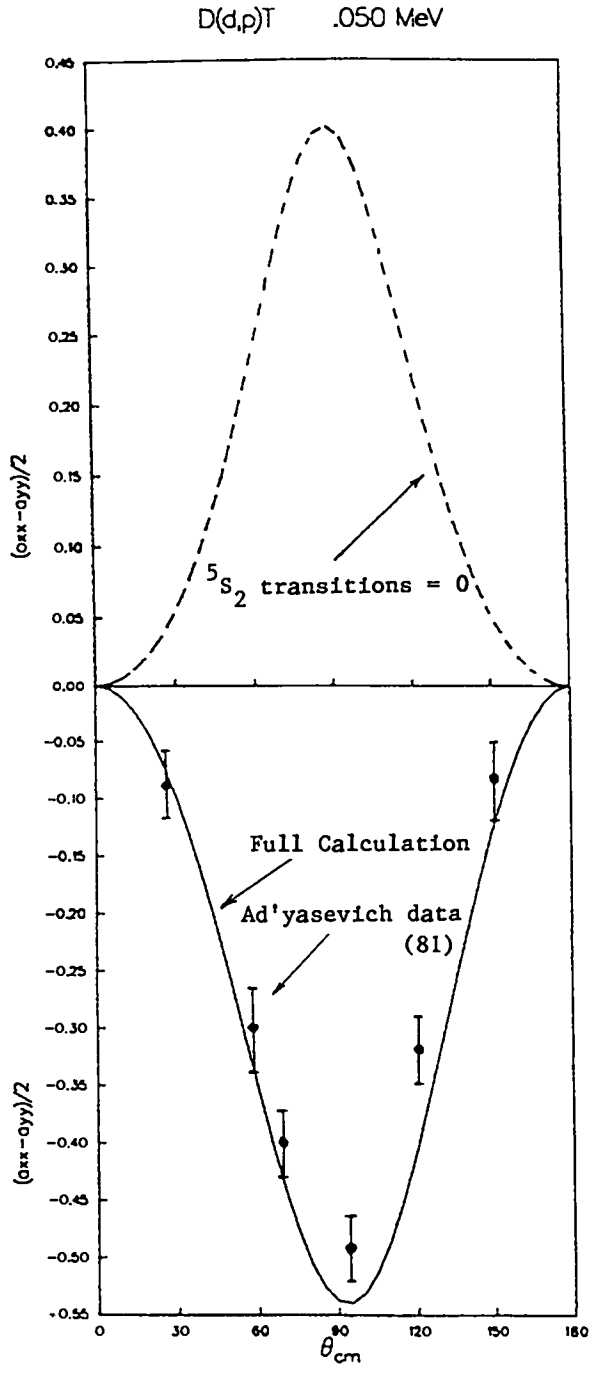

Fig. 1. R-matrix calculations of the analyzing tensor $\frac{1}{2}(A_{xx}-A_{yy})$ for the D(d,p)T reaction at E_d = 50 keV, compared with data taken from contour plots in Ref. 5. The solid curve is the full calculation and the dashed curve is without the $^5S_2$ transition.

We are also repeating the earlier resonating group calculations[3] with more realistic (non-central) nucleon-nucleon forces and including D-state contributions from the bound deuterons. Preliminary results for the $^5S_2$ transitions show excellent agreement, both in magnitude and phase, with the $^5S_2$ transition elements from the R-matrix fit. Work continues on the other transitions ($^1S_0$, ^3P_J), important at low energies.

Thus, there is evidence in presently measured analyzing-power data and in realistic four-body calculations that the $^5S_2$ transitions of the d+d reaction are large at low energies, resulting in only slight suppression of the secondary neutron- and tritium-producing reaction occurring in a reactor fueled by polarized d and ^{3}He.

B. R-Matrix Analyses of Reactions in the ^{7}Li and ^{11}B Systems (G. M. Hale)

New R-matrix analyses of reactions in the ^{7}Li and ^{11}B systems are nearing completion for use in the ENDF/B-VI standard cross-section evaluation for light-element reactions. The ^{7}Li analysis includes recent measurements of ^{6}Li(n,t)^{4}He and ^{4}He(t,n)^{6}Li angular distributions, as well as extended differential cross section and polarization data from Los Alamos for t-^{4}He scattering, that have helped determine the ^{7}Li level parameters over a wide range of excitation energies.

A model for partially including deuteron exchange in the ^{6}Li(n,t)^{4}He reaction by taking into account peripheral channel overlap effects in R-matrix theory was also tested in this analysis. It was found[6] that these effects can account for much of the behavior of the low-energy ^{6}Li(n,t) cross sections, while significantly improving the fits to t-^{4}He elastic differential cross sections at low energies.

The ^{11}B analysis includes new experimental information about the ^{7}Li(α,n)^{10}B cross section that disagrees substantially with earlier ^{10}B(n,α_0)^{7}Li measurements in the several hundred-keV neutron energy region. Unfortunately, the data for other reactions in the analysis are not sufficiently sensitive to large changes in the ^{10}B(n,α_0)^{7}Li cross section in this region to indicate which measurements are correct. Absolute measurements of ^{10}B(n,α_0) and ^{10}B(n,α_1) cross sections at energies below 1 MeV would be very useful to help resolve the discrepancy.

C. R-Matrix Analysis of Reactions in the ^{5}He System [G. Hale and D. Dodder (X-Division Consultant)]

Our R-matrix work on reactions in the ^{5}He system that began a number of years ago has been sustained by continuing interest in the d-t reaction as a fusion energy source, and by numerous experiments, particularly those made with polarized particles, that await interpretation in terms of the level structure of ^{5}He. We have obtained a solution for this problem in terms of R-matrix parameters that account for most of the known ^{5}He data at energies corresponding to E_x below 22 MeV.

The 3-channel analysis includes data for the reactions ^{4}He(n,n)^{4}He, T(d,n)^{4}He, T(d,d)T, and T(d,n)^{4}He* at neutron energies up to 27 MeV and at deuteron energies up to ~ 8 MeV. The 2500-point data set is representative of every type of measurement that has been made for these reactions, and includes many measurements with vector- and tensor-polarized deuterons, in addition to the most recent and precise measurements of the d-t reaction cross section. The overall chi-square per degree of freedom for the fit is less than 2.3.

Using an elegant new numerical subroutine for calculating Coulomb functions in the complex plane, we have begun to explore the S-matrix pole structure for ^{5}He that results from our R-matrix parameters. Above the three known lowest states of ^{5}He, we find excited states with $J^\pi = 5/2^+(2)$, $3/2^-$, $1/2^+$, $3/2^+$, and $7/2^+$, for $19.7 \leqq E_x \leqq 27$ MeV, with widths in the range $0.94 \leqq \Gamma \leqq 9.1$ MeV, as well as very broad "background" states in these and other J^π's.

It is interesting to note that most of the levels, including the well-known $3/2^+$ resonance just above the d-t threshold, have poles on more than one unphysical sheet of the many-channel Riemann energy surface. We are exploring the consequences of this fact for alpha-particle sticking probability results in μ-catalyzed d-t fusion that recently have been attracting considerable attention.

D. Bibliographic Survey of Medium Energy Inclusive Reaction Data (E. D. Arthur, D. G. Madland, D. M. McClellan)

We have completed a search of bibliographic information of currently available inclusive reaction data with particular emphasis on experimental and theoretical results for particle and gamma-ray emission. Other types of information included were entries pertaining to the use, characterization, and validation of appropriate medium-energy theoretical models, along with experimental results pertaining to damage, nuclear recoils, and radiation effects produced by medium-energy projectiles.

The search covered data for the following projectiles: p, d, t, ^{3}He, ^{4}He, and lithium ions, over an incident energy range extending from approximately 50 MeV to 1000 MeV. The search utilized the US Department of Energy RECON (Remote Console) bibliographic data system* and covered the time period from 1947-1985. Initially, approximately 17 000 possible entries were identified. Subsequently, approximately 1000 references were selected that are appropriate for describing the current state of knowledge concerning inclusive reaction data, both from an experimental and theoretical viewpoint. These references also include bibliographic information needed for assessment and validation of nuclear model capabilities.

For the selected bibliographic entries, the following information will be provided: reference, author(s), title, target materials, and descriptor(s) characterizing the content of the bibliographic entry. The processing of this information has been completed and will be used to produce an upcoming Los Alamos report describing the results of the bibliographic survey.

E. Improvement of Activation Cross Sections Needed for REAC Calculations (E. D. Arthur)

Improvements of nuclear cross-section data utilized in the REAC[7] code have been made. These improvements were motivated by calculational needs associated with determination of dose rates produced by 50-MeV protons (and associated neutrons) on beamstop materials used in design studies of the ATSU accelerator. Additionally, verification of air activation results calculated at Hanford Engineering Design Laboratory prompted part of the need for improved cross-section data.

The targets considered, reaction types, and residual nuclei of interest appear in Table I. The methods used to generate the required data included GNASH[8] calculations utilizing parameters determined from analyses of high energy neutron and proton reactions on aluminum and copper isotopes. (See other contributions to this progress report). Additionally, calculations were made using the ALICE[9] preequilibrium-evaluation code.

Figure 2 illustrates results for two major activation products occurring from neutron reactions on copper, as calculated using GNASH. The $^{65}Cu(n,2n)^{64}Cu$ cross section shown here is approximately two orders of magnitude higher for energies above 30-35 MeV than data included in the REAC library, which was based

*The Department of Energy RECON computerized information retrieval system is operated by the US Department of Energy Office of Scientific and Technical Information, Oak Ridge, Tennessee.

on results from the THRESH[10] code. The ^{60}Co production cross section agrees with the REAC data at energies below 20 MeV. Here the source of REAC data was the $^{63}Cu(n,\alpha)^{60}Co$ cross section appearing in ENDF/B-V. At higher energies, a substantial contribution to ^{60}Co production comes from the $^{65}Cu(n,2n\alpha)$ reaction sequence not included in the REAC library.

TABLE I

ACTIVATION CROSS SECTIONS CALCULATED FOR USE IN THE REAC CODE

Target	Residual Nucleus Produced	Reaction Type
^{27}Al	^{24}Na	(n,α)
^{27}Al	^{22}Mg	$(n,2n\alpha)$
^{65}Cu	^{64}Cu	$(n,2n)$
^{65}Cu	^{60}Co	$(n,2n\alpha)$
^{63}Cu	^{60}Co	(n,α)
^{40}Ar	^{40}Cl	(n,p)
^{40}Ar	^{39}Cl	$(n,np)(n,d)$
^{40}Ar	^{39}S	$(n,2p)$
^{40}Ar	^{38}S	$(n,n2p)(n,^{3}He)$
^{40}Ar	^{35}S	$(n,2n\alpha)$
^{40}Ar	^{37}S	$(n,\alpha)(n,2n2p)$
^{16}O	^{13}N	$(n,2nd)(n,t)$
^{16}O	^{15}C	$(n,2p)$
^{16}O	^{11}C	$(n,2n\alpha)$
^{14}N	^{11}C	(n,X)
^{14}N	^{7}Be	(n,X)
^{12}C	^{7}Be	(n,X)

In addition to GNASH calculations, a very useful tool for scoping studies of activation data was use of the ALICE code, which includes preequilibrium effects via the geometry dependent hybrid model. Also, the majority of parameters utilized by the code have been established and verified through reaction calculations for a variety of nuclei over a wide (up to 200 MeV) energy range. For these reasons, and because a large number of reaction paths are included in each calculation, the ALICE code is particularly attractive, particularly at higher projectile energies. Figure 3 illustrates excitation functions for activation products resulting from n + ^{40}Ar reaction calculations made with ALICE. Most of the cross sections shown agree well with ENDF/B results (where available) as well as other cross-section values currently included in the REAC code.

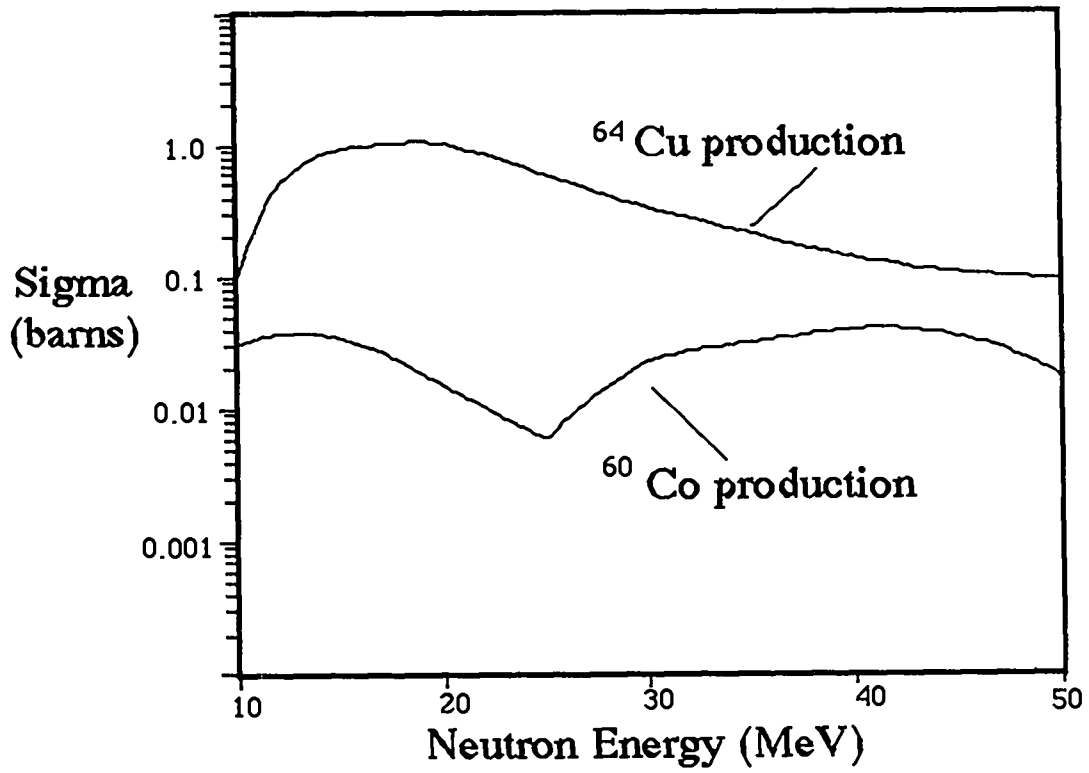

Fig. 2. Excitation functions of ^{64}Cu and ^{60}Co production determined from GNASH calculations of n + Cu reactions.

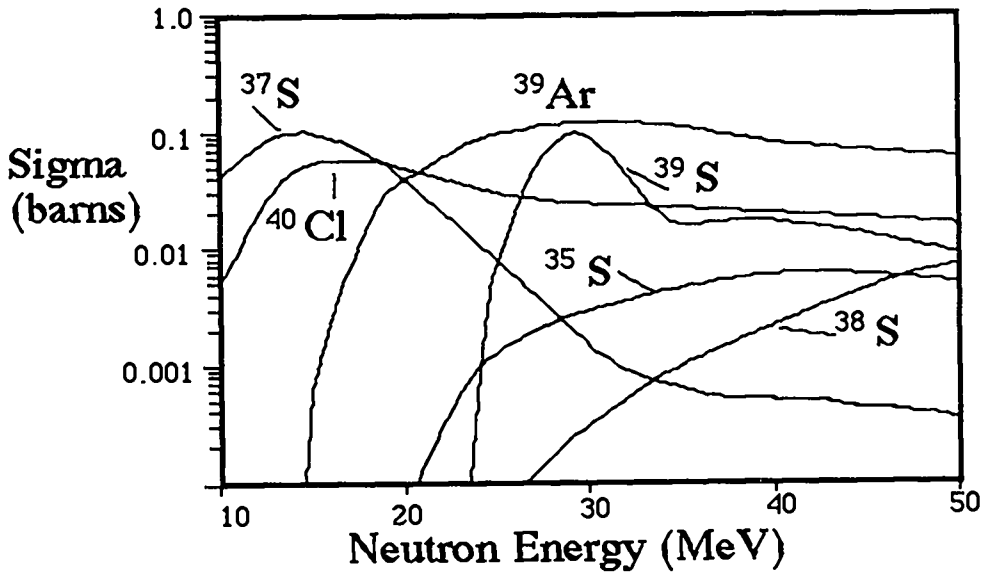

Fig. 3. Excitation functions resulting from ALICE calculations of n + ^{40}Ar reactions.

Similar calculations were also made for neutron-induced activation data on ^{14}N and ^{16}O. For binary or tertiary reactions [(n,p), (n,2n), etc.], the calculations agree reasonably with experimental data. For more complex reaction sequences such as $^{16}O(n,X)^{11}C$, calculations were first made for equivalent proton-induced reactions and were compared with data. Where necessary, the ALICE results were adjusted to better agree with such data. These same adjustments were then used in the prediction of neutron-induced data of interest.

Finally, a particularly interesting reaction for activation considerations is $^{12}C(n,X)^{7}Be$ because of the long halflife of ^{7}Be. Experimental data[11] are available for the sum of $^{12}C(p,d\alpha)^{7}Be$ and $^{12}C(p,np\alpha)^{7}Be$ reactions, which were used to adjust ALICE calculated results. However, because ALICE calculations indicated the ^{7}Be production occurring in n + ^{12}C and p + ^{12}C reactions to be almost identical, the $^{12}C(n,X)^{7}Be$ cross sections assigned to the REAC code were taken to be identical to ^{7}Be production results from p + ^{12}C reactions.

F. Calculations of Energetic Neutron and Proton Reactions on Aluminum (E. D. Arthur)

Group T-2 is presently undertaking an effort to systematically extend ENDF/B-like nuclear data evaluations to energies beyond the traditional upper limit of 20 MeV. Concurrently we will provide increased data capabilities (charged-particle emission cross sections, charged-particle induced reactions) that are allowed by new format capabilities developed primarily at Los Alamos.[12] An initial effort to produce such evaluated data libraries involves the determination of neutron and proton-induced reaction data on ^{27}Al up to incident energies of 50 MeV. This contribution will describe portions of the theoretical calculations performed to provide the required data while the Section R offers details concerning the methods used to generate the evaluated files.

Preliminary descriptions of calculations made for p + ^{27}Al reactions are contained in Ref. 13. These provide general information concerning the theoretical models and parameters used. However, for the calculations described here, more effort was devoted to determination of input parameters, particularly optical model parameters describing neutron, proton, and deuteron emission. The neutron optical model parameters were based on the global set of Wilmore-Hodgson[14] with adjustments made to better reproduce higher-energy (> 20 MeV) total cross sections. Proton optical model parameters were determined to best fit available proton reaction cross-section data,[15] as well as to accurately describe low-energy proton emission. Deuteron optical parameters were taken

from the global set developed by Perey and Perey.[16] Because of the relative sparsity of deuteron data, several sets of deuteron optical parameters were tested through comparison of calculated reaction cross sections. Very little differences were observed among the calculated results, so that the Perey parameters were retained. Finally, alpha particle optical model parameters were taken from information provided in the Perey and Perey compilation.[17] Table II summarizes the optical parameters used for the present calculation.

TABLE II

OPTICAL MODEL PARAMETERS USED IN n + ^{27}Al AND p + ^{27}Al CALCULATIONS[a]

	r	a	r_c
Neutrons			
$V = 47 - 0.25E - 0.003E^2$	1.304	0.66	
$W_{SD} = 9.52 - 0.053E$	1.257	0.48	
$V_{SO} = 7.$	1.304	0.66	
Protons			
$V = 48. - 0.32E$	1.14	0.75	
$W_{SD} = 9. - 0.2E$	1.32	0.52	
$W_{vol} = -2.7 + 0.2E$	1.32	0.52	
$V_{SO} = 6.$	1.01	0.75	
			1.2
Deuterons			
$V = 89.1 - 0.22E$	1.15	0.81	
$W_{SD} = 14.4 + 0.2E$	1.34	0.68	
			1.15
Alphas			
$V = 152.$	1.39	0.62	
$W_{vol} = 33.9$	1.39	0.62	
			1.22

[a] All well depths in MeV; geometrical parameters and charge radius, r_c, in Fermis.

In preparation for the main body of calculations, direct reaction cross sections for (p,p') scattering were calculated, as described in Ref. 13 using the B_ℓ values of Ref. 18. Additionally, the weak coupling model was assumed sufficient to describe scattering from the six states in ^{27}Al considered. A similar approach was followed for distorted wave Born approximation calculations of direct-reaction components to (n,n') scattering.

To further investigate and verify these theoretical calculations, comparisons were made with measured particle (n,p,d,α) emission spectra[19,20] at E_n = 15 MeV. These results appear in Figs. 4-7. Likewise, calculated neutron-induced gamma-ray production spectra were compared with experimental data[21] measured at 20 MeV. This comparison appears in Fig. 8. For proton-induced reaction calculations, the comparisons described in Ref. 13 were extended through use of particle emission spectral data measured by Bertrand and Peelle[22] at proton energies of 62 MeV. Figure 9 provides an example of a comparison of our calculated proton emission spectra with these data. Finally, Fig. 10 provides examples of calculated neutron and gamma-ray emission spectra produced by 50-MeV neutron interactions with ^{27}Al.

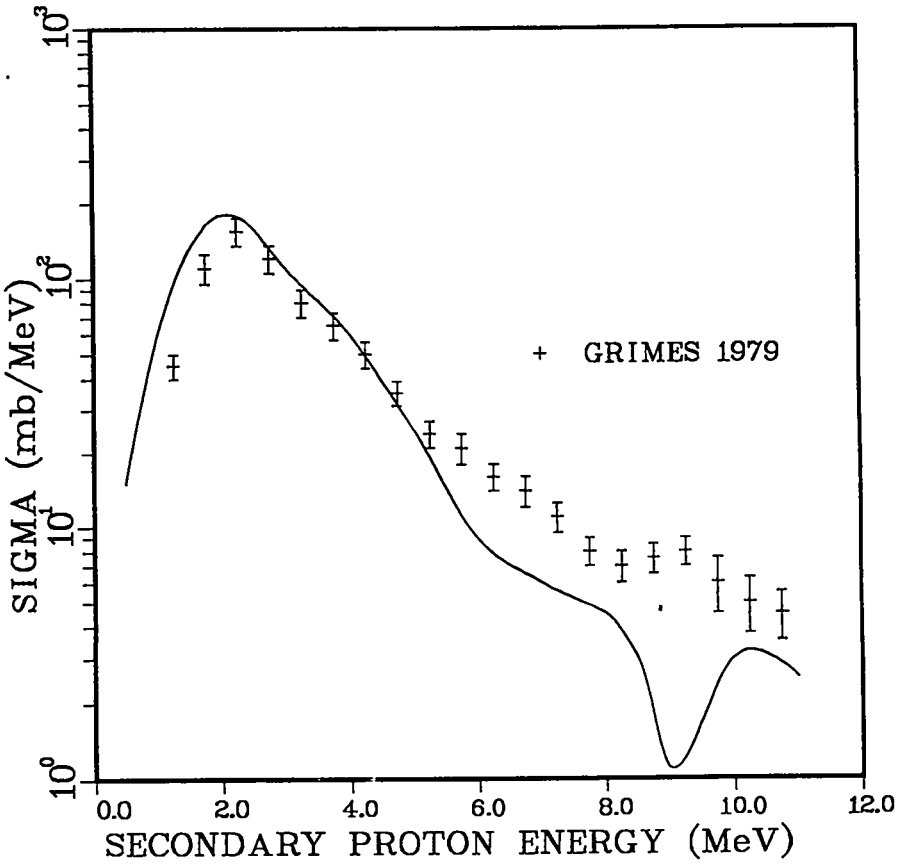

Fig. 4. Comparison of calculated proton emission spectra produced by 15-MeV neutron interactions on ^{27}Al with the data of Ref. 19.

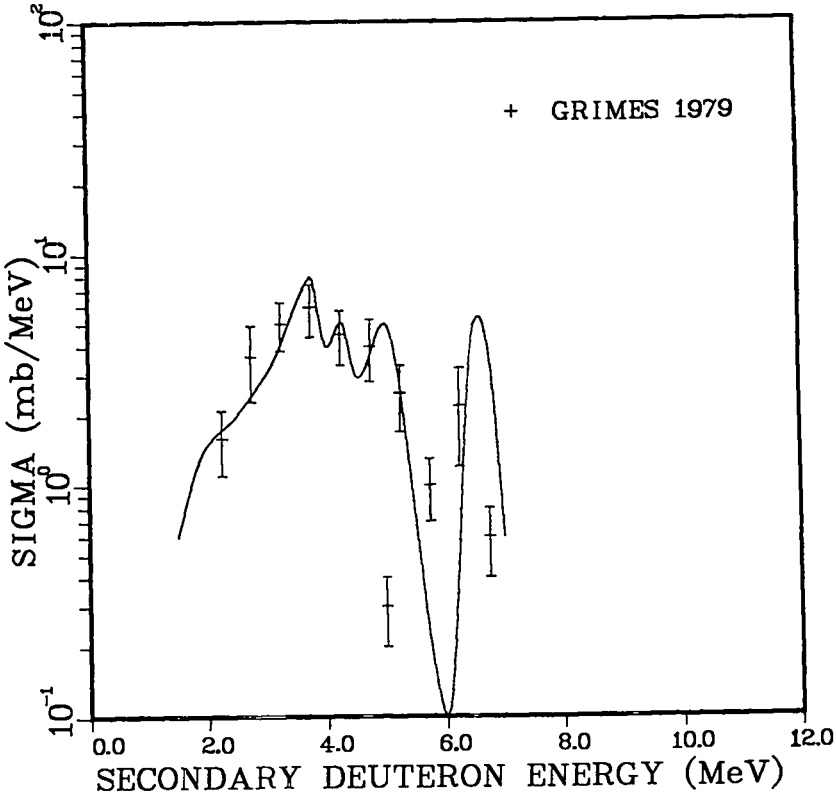

Fig. 5. Comparison of calculated deuteron emission spectra produced by 15-MeV neutron interactions on ^{27}Al with the data of Ref. 19.

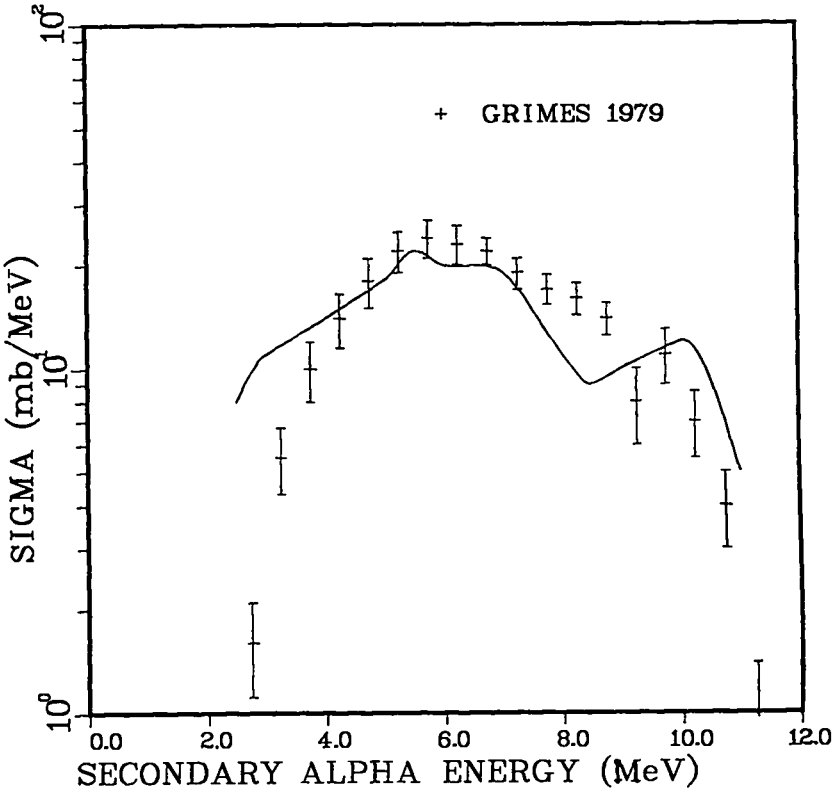

Fig. 6. Comparison of calculated alpha-particle emission spectra produced by 15-MeV neutron interactions on ^{27}Al with the data of Ref. 19.

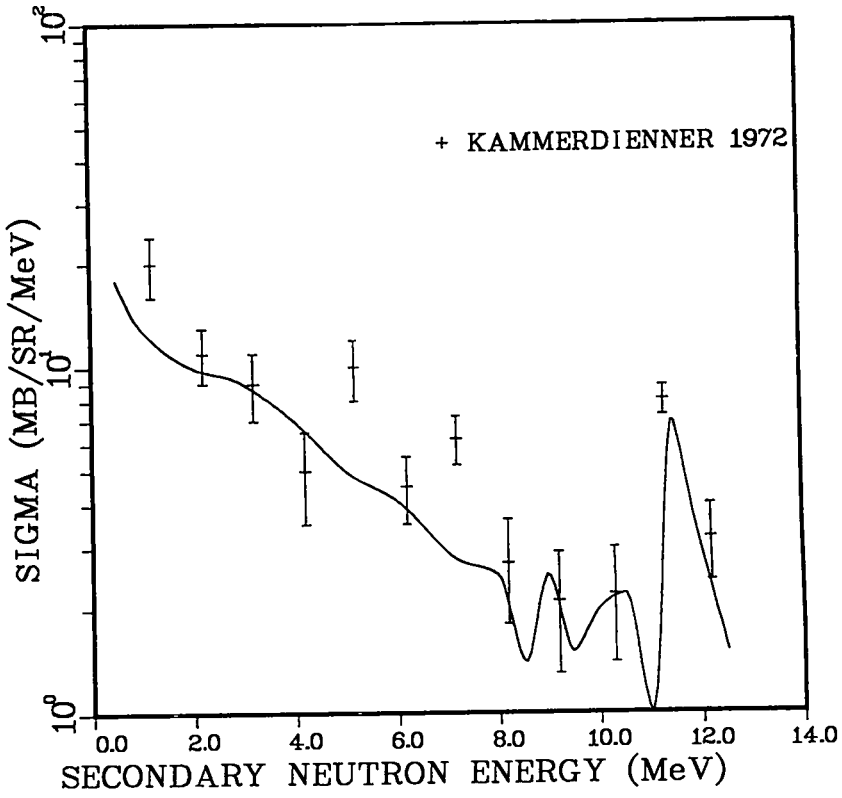

Fig. 7. Comparison of the calculated neutron emission spectra resulting from the 15-MeV neutron reactions on ^{27}Al with the Kammerdiener data.[20]

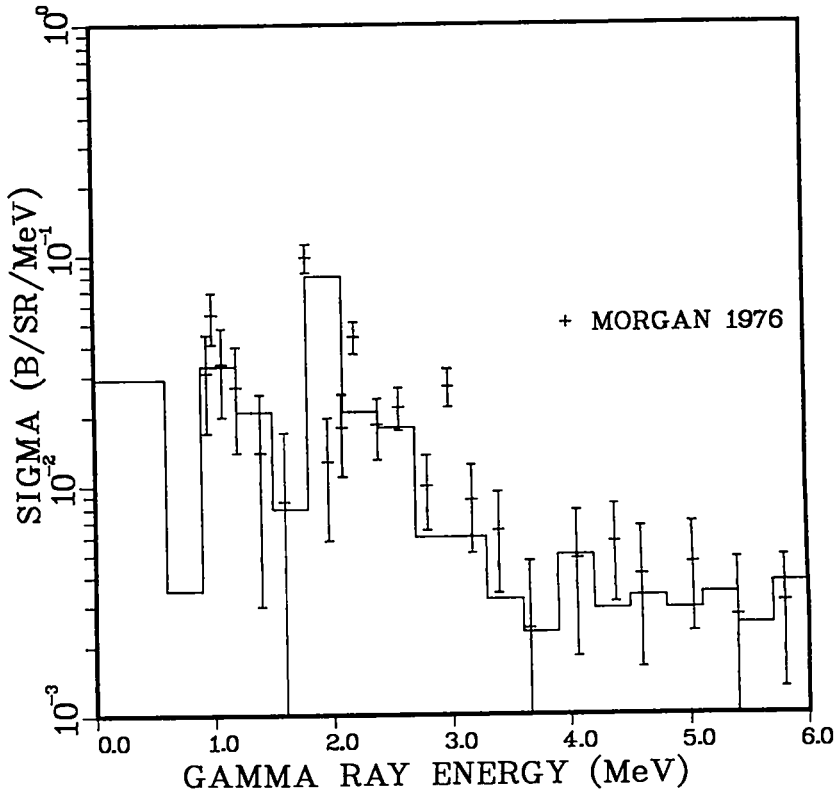

Fig. 8. The calculated gamma-ray production spectrum produced by 20-MeV neutrons on ^{27}Al is compared with the data of Morgan.[21]

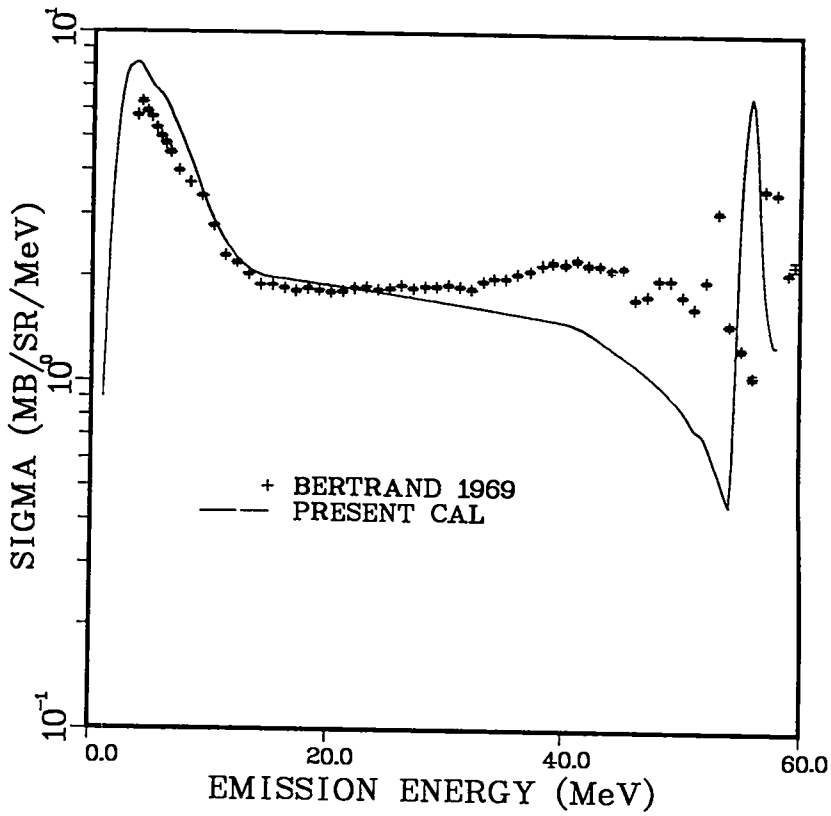

Fig. 9. The 30° proton emission spectrum calculated for 60-MeV proton reactions on aluminum is compared with the data of Bertrand and Peelle.[22]

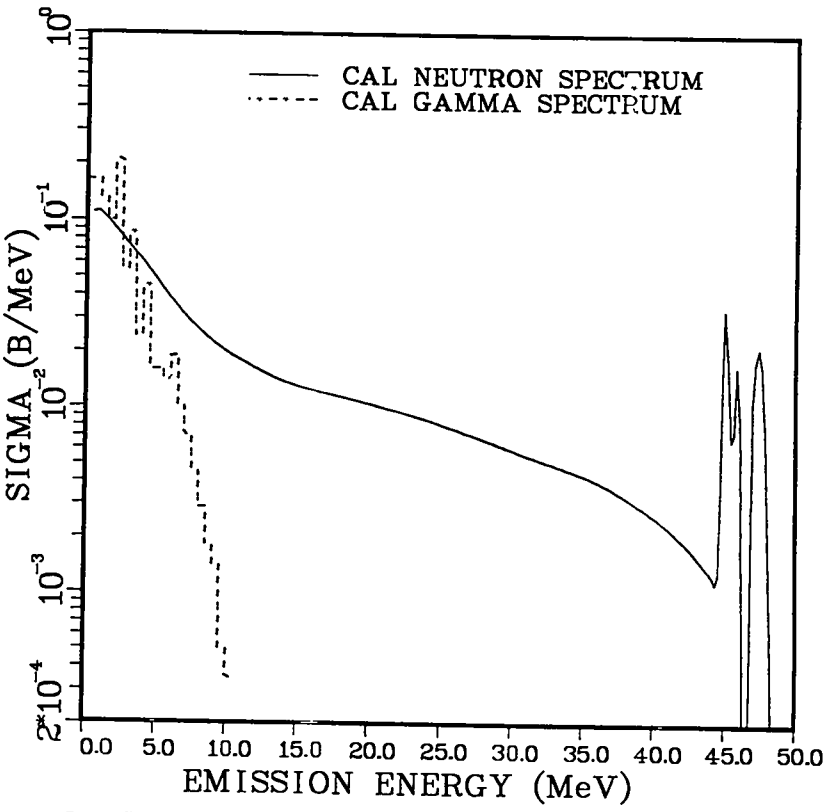

Fig. 10. Examples of calculated neutron and production spectra produced by 50-MeV n+^{27}Al reactions.

G. Improved Optical Model for Neutron Reactions on Iron from 0.1 to 100 MeV (E. D. Arthur)

Neutron optical model parameters originally derived for calculations[23] of n + ^{54,56}Fe reactions to E_n = 40 MeV have been improved, and their range of applicability extended to 100 MeV. The original parameters of Ref. 23 overpredicted (by approximately 10%) new reaction cross-section data measured after their determination. As a result, they were not suitable for extensions of the calculations of Ref. 23 to higher incident energies. A parameter set applicable to 100 MeV was derived by Prince,[24] but the form of the imaginary potential appeared to be unduly complicated, consisting of three piecewise continuous segments for $0.5 < E_n < 100$ MeV.

In order to preserve the quality of fits to lower energy total cross section and elastic scattering data, the new parameter determination utilized identical geometry and initial surface derivative well depths as the parameters of Ref. 23. However, the energy dependence of both the real and imaginary surface well depths was changed significantly. The volume imaginary form was altered completely. The geometry parameters were changed to agree with those of the real potential. Secondly, the volume imaginary well depth of Ref. 23 was not particularly realistic because the W_{vol} term became greater than zero at an energy of about 0.8 MeV. In the new parameter set, the volume term does not contribute until an incident energy around 9 MeV is reached.

The resulting parameter set appears in Table III, while in Figs. 11 and 12 comparisons are made with total cross sections up to 100 MeV, and with reaction cross section data to 50 MeV. The agreement with total cross sections below 40 MeV is quite good and is comparable to the fit achieved in Ref. 23. A similar quality of fit occurs out to the maximum energy considered, 100 MeV. Figure 12 compares reaction cross sections calculated using these parameters with values obtained using the older data set. The higher energy behavior is much improved while maintaining agreement with lower energy data.

In summary, improved optical model parameters were determined that describe neutron reactions on iron from 0.1 to 100 MeV. To do so, it was sufficient to use a standard Woods-Saxon surface derivation potential form rather than a more complicated form such as that of Ref. 24. These parameters should thus be suitable for Hauser-Feshbach preequilibrium calculations in which one needs to simultaneously describe phenomena sensitive to both the low- and high-energy behavior of the neutron optical potential.

TABLE III

IMPROVED NEUTRON OPTICAL MODEL PARAMETERS FOR IRON[a]

	r	a
$V = 49.747 - 0.297E - 0.0003E^2$	1.287	0.56
$W_{vol} = -1.6 + 0.18E$	1.287	0.56
$V_{SO} = 6.2$	1.12	0.47
$W_{SD} = 6 + 0.42E$	1.345	0.47
Above $E_n = 6$ MeV		
$W_{SD} = 8.52 - 0.224\ (E-6)$	1.345	0.47

[a]All well depths are in MeV; geometrical parameters are in Fermis.

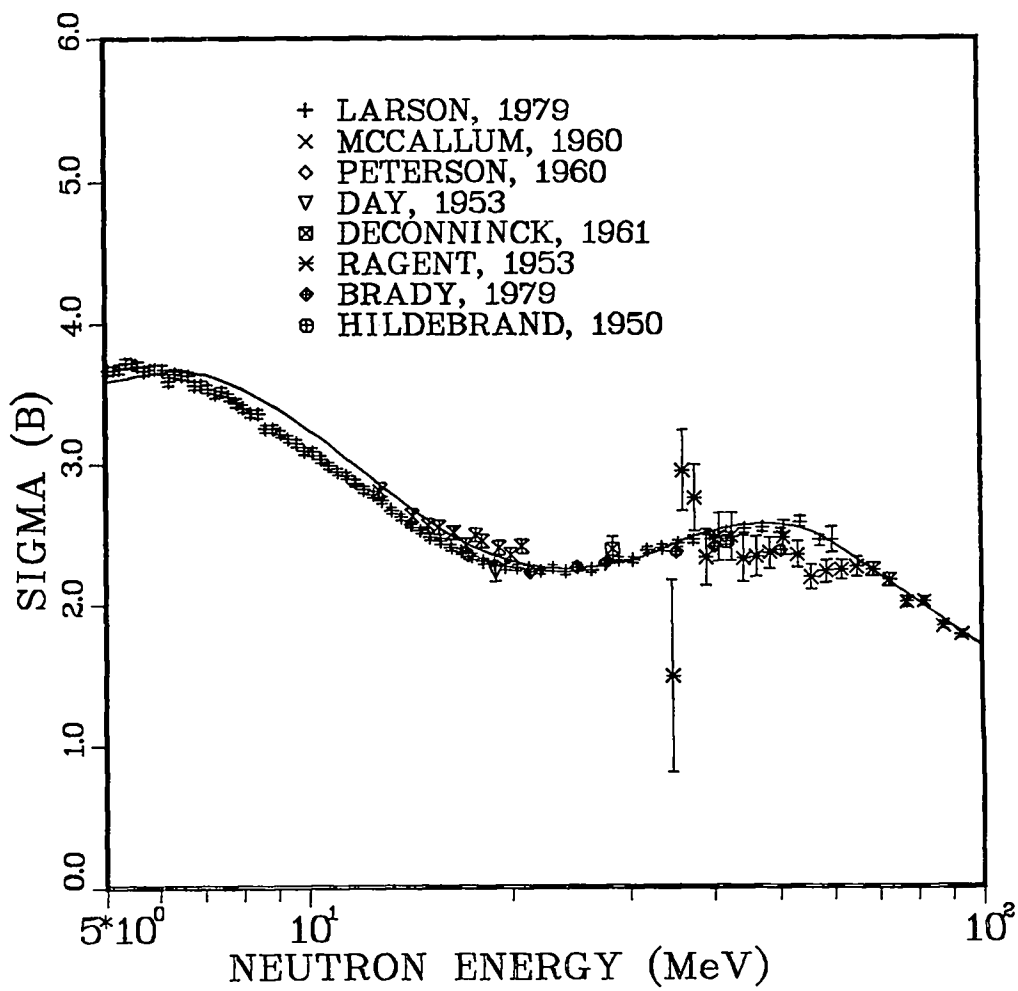

Fig. 11. Comparison of neutron total cross sections calculated using the parameters of Table III with experimental data available up to E_n = 100 MeV.

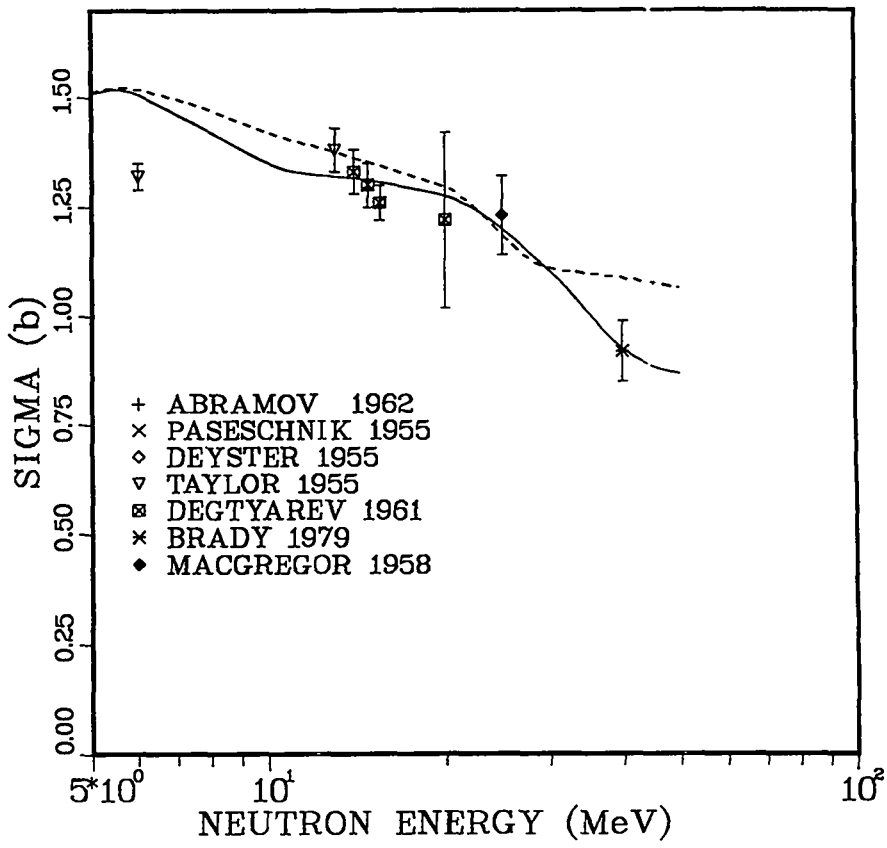

Fig. 12. Comparison of reaction cross sections calculated using the present parameters with available experimental data and with values obtained using the parameters of Ref. 23 (dashed curve).

H. Calculation of Higher Energy Neutron and Proton Reactions on $^{54,56}Fe$

(E. D. Arthur)

As part of our effort to extend nuclear data libraries to energies above 20 MeV, we have redone our 1980 calculations[23] of neutron reactions on iron isotopes. In the process, we extended them to include more reaction paths, along with careful determination of charged-particle (p,d,α) emission spectra. In addition, we used the model parameters determined from the higher energy neutron reaction analysis to calculate cross sections, particle emission (n,p,d,α) and gamma-ray emission data produced by proton reactions for incident energies up to 60 MeV.

The calculations employed the GNASH preequilibrium statistical model code[8] and utilized parameter determination techniques similar to those described in Ref. 23. Major differences were use of the extended neutron optical model parameters described in Section G, as well as use of the Perey global deuteron optical model potential[16] to describe deuteron emission.

Because a substantially different neutron optical model was employed, the distorted wave Born approximation (DWBA) calculation of direct reaction components to (n,n') scattering was repeated. As in Ref. 23, these DWBA results were normalized using the B_ℓ values determined from (p,p') scattering measurements.[25]

However, significant differences were obtained in the magnitude of these DWBA components at higher incident energies, due mainly to substantial differences in neutron optical parameters at energies above 30 MeV. These differences are illustrated in Fig. 13 where excitation functions for scattering from the 0.846 MeV 2^+ states in ^{56}Fe are compared as calculated using the improved neutron optical parameters (solid curve) and those of Ref. 23 (dashed curve).

Most of the comparisons for neutron reaction data made in Ref. 23 were repeated for the present calculations. Comparable agreement was obtained. Figure 14 illustrates an additional data type included now that was not previously considered. The example shown compares the calculated deuteron emission spectra produced by 15-MeV neutrons on ^{56}Fe with data measured by Grimes et al.[26]

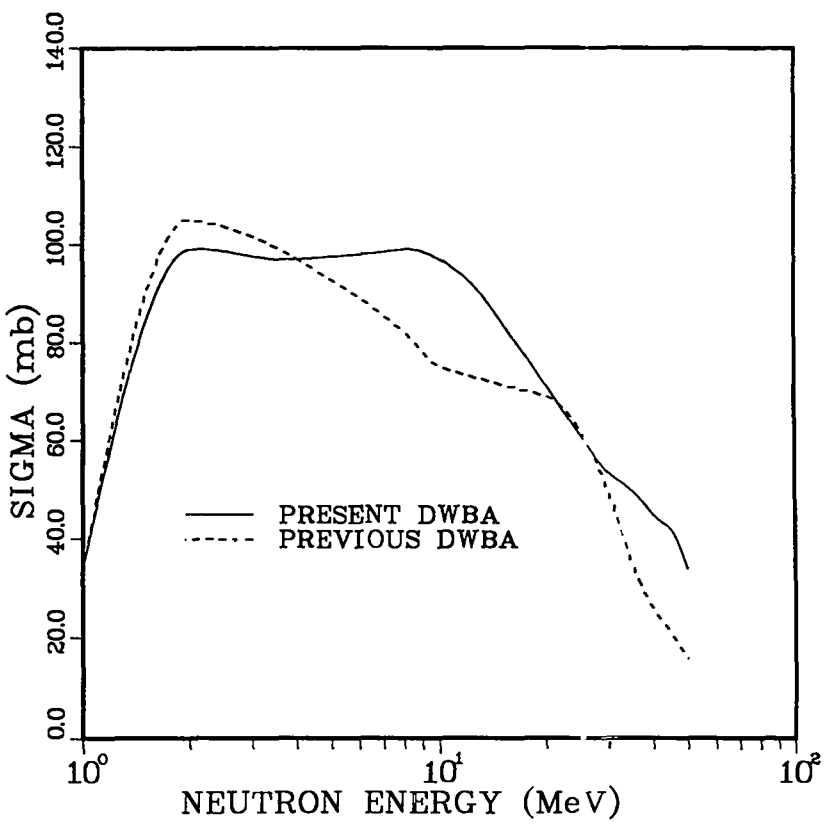

Fig. 13. Comparison of excitation functions produced from DWBA calculations of (n,n') scattering from the 0.846 MeV 2^+ level in ^{56}Fe. The solid curve utilizes the parameters of Sec. G, while the dashed curve results from the parameters of Ref. 23.

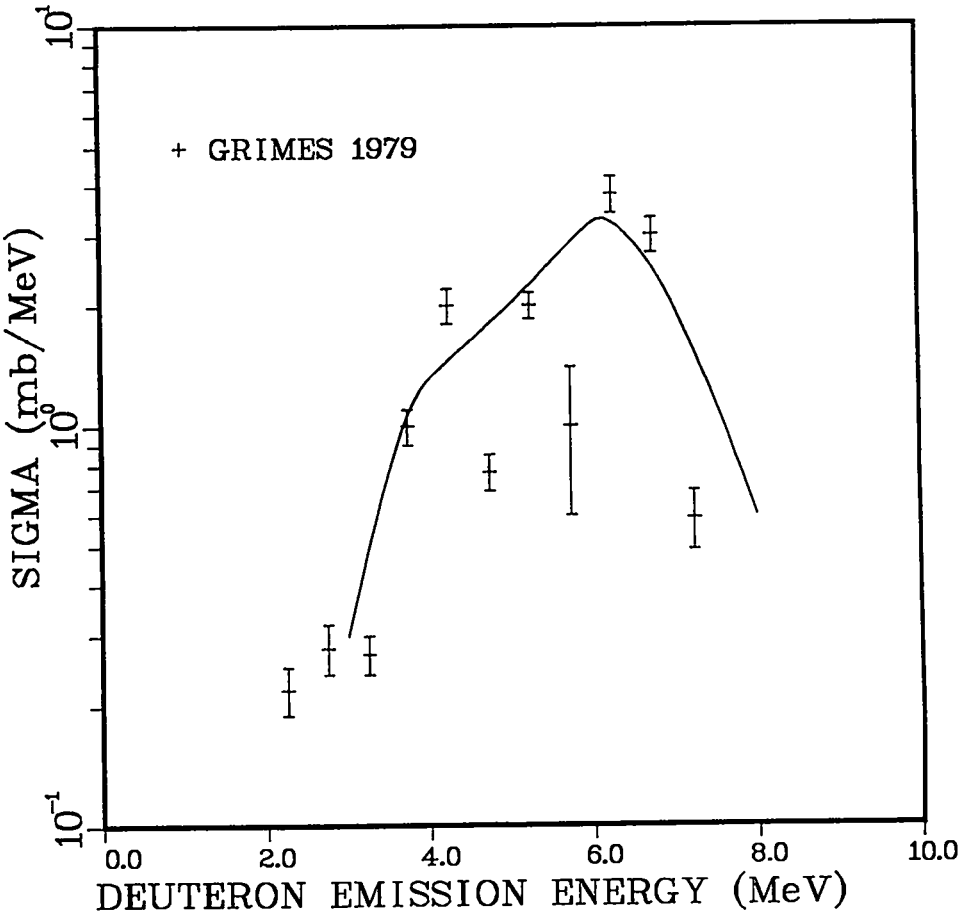

Fig. 14. Comparison of calculated deuteron emission spectra produced by 15-MeV neutrons on ^{56}Fe with data measured by Grimes et al.[26]

For proton induced reactions, the DWBA calculations were repeated using the modified Perey proton optical parameters of Ref. 23 along with the Mani $^{4}B_{\ell}$ values.[25] Direct reaction components calculated at E_p = 60 MeV were comparable in magnitude to results obtained for (n,n') scattering using the improved neutron optical model parameters described previously.

Although calculation of proton-induced cross sections and spectra has been completed for energies up to 50 MeV, extensive verification of the results has not been completed. However, initial comparisons have been made with charged-particle emission spectra measured by Bertrand and Peelle[27] for 62-MeV proton reactions on ^{56}Fe. Such results are shown in Figs. 15-17 for proton, deuteron, and alpha-particle emission, respectively. Such verification efforts will continue with the ultimate goal being production of neutron and proton induced reaction libraries on iron up to incident energies of 50 MeV.

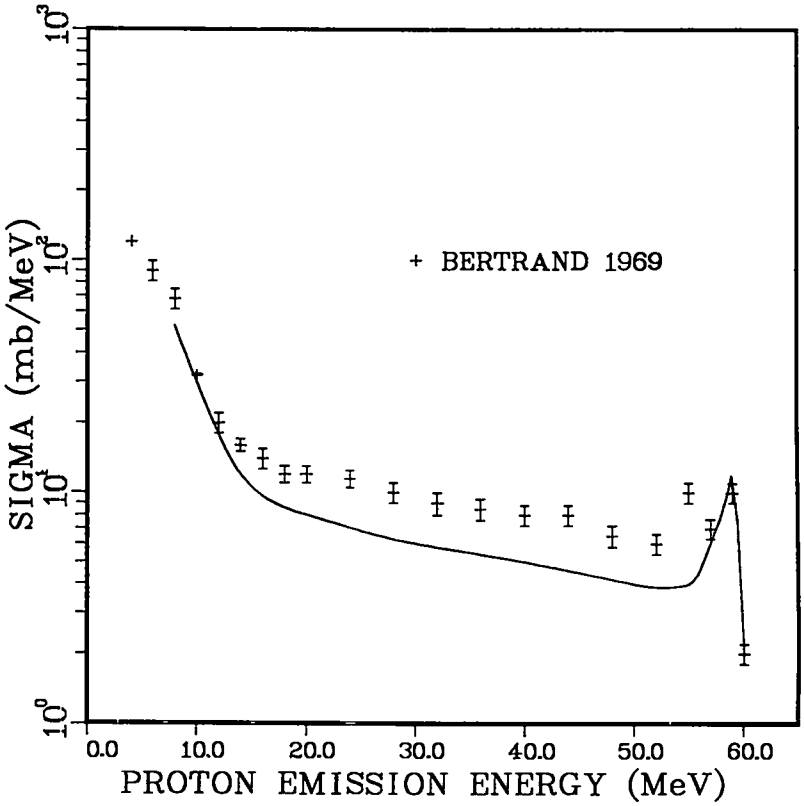

Fig. 15. Calculated proton total emission spectra for 60-MeV proton reactions on ^{56}Fe are compared with the data of Ref. 27.

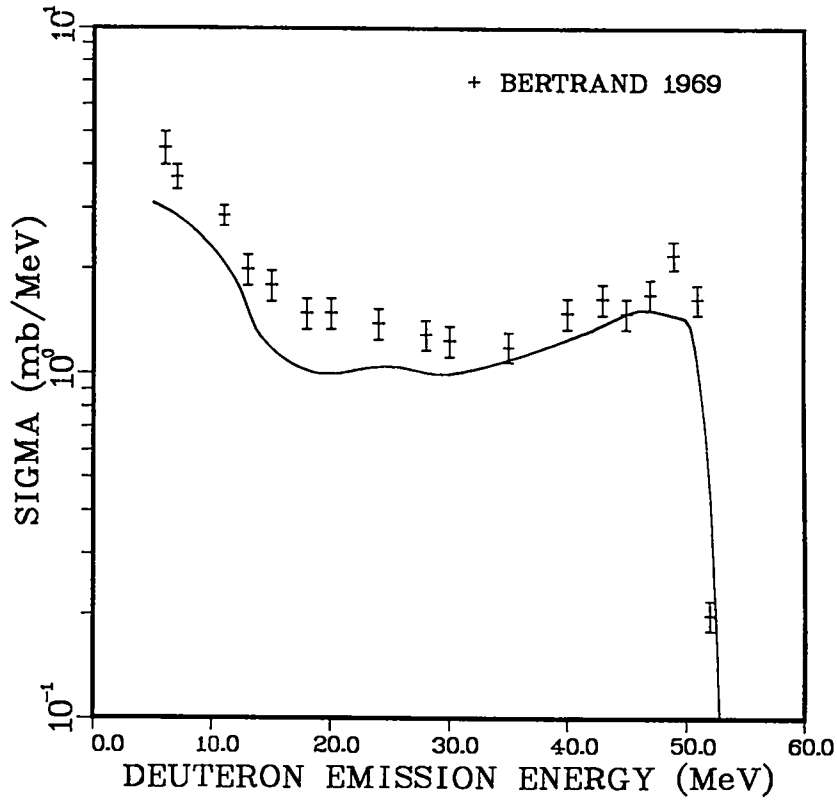

Fig. 16. Calculated total deuteron emission spectra for 60-MeV proton reactions on ^{56}Fe are compared with the data of Ref. 27.

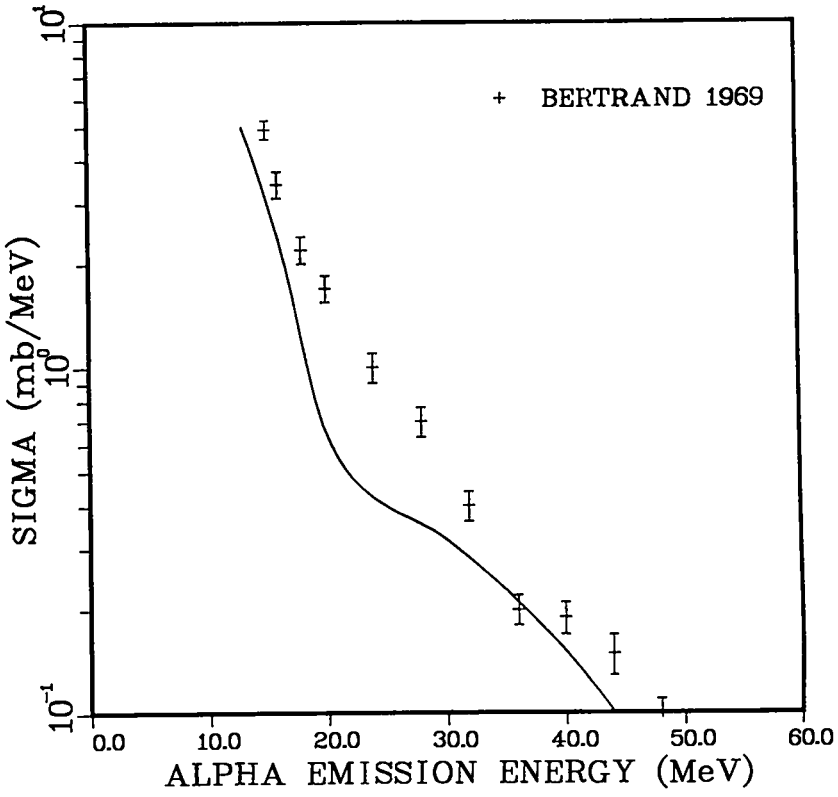

Fig. 17. Calculated total alpha particle emission spectra for 60-MeV proton reactions on ^{56}Fe are compared with the data of Ref. 27.

I. Calculations of Higher Energy Proton and Neutron Reactions on $^{58,60,62}Ni$ (E. D. Arthur)

Hauser-Feshbach, preequilibrium, direct-reaction, and optical model calculations were made for incident neutron energies between 20 and 50 MeV to provide basic data required for extension of ENDF/B neutron libraries up to E_n = 50 MeV. Similarly, data necessary for production of libraries describing energetic proton reactions on nickel isotopes were also calculated. The techniques used for parameter determination were similar to those described in Ref. 23 and were developed by R. C. Harper* during a 1980 collaboration with T-2. Although most parameters were determined and verified by Harper, further work was done to reconfirm their validity through calculations with improved model code versions, as well as extension of their use to a systematic study of proton induced reactions on nickel isotopes. Also, the reaction chains used for proton and neutron calculations were extended to include sixty residual nuclei reached through n, p, d, and α emission from ten compound nuclei.

*R. C. Harper--present address: Sparta Incorporated, Huntsville, Alabama.

Optical model parameters determined for neutrons, protons, deuterons, and alphas appear in Table IV. For the neutron optical model, simultaneous fits were made to total cross sections from 1 to 50 MeV, elastic angular distributions above 6 MeV, as well as to resonance parameter data (S_0, S_1, R'). For protons, a modified form of the Perey[17] proton optical model parameters was adjusted to reproduce higher energy p + ^{59}Co reaction cross-section data. The parameters utilized for alpha particle emission were those of Lemos, as described in Ref. 23. Deuteron emission was calculated using the global parameters of C. Perey and F. Perey.[16]

TABLE IV

OPTICAL MODEL PARAMETERS USED FOR CALCULATION OF NUCLEON INDUCED REACTIONS ON ^{58,60,62}Ni[a]

	r	a
Neutrons		
$V = 50.06 - 0.3721E$	1.287	0.56
$W_{vol} = -0.0941 + 0.197E$	1.287	0.56
$V_{SO} = 6.2$	1.12	0.47
$W_{SD} = 4.87 + 0.27E$	1.345	0.47
Above $E_n = 6$ MeV		
$W_{SD} = 6.497 - 0.225\ (E-6)$		
Protons		
$V = 57.12 - 0.55E$	1.25	0.65
$W_{SD} = 13.5 - 0.1E$	1.25	0.47
$W_{SO} = 7.5$	1.25	0.47
$r_c = 1.25$		
Deuterons		
$V = 94.95 - 0.22E$	1.15	0.81
$W_{SD} = 14.4 + 0.2E$	1.34	0.68
$r_c = 1.15$		
Alphas		
$V = 193. - 0.15E$	1.37	0.56
$W_{vol} = 21. + 0.25E$	1.37	0.56
$r_c = 1.4$		

[a]All well depths in MeV; geometrical parameters and charge radius, r_c, in Fermis.

Distorted wave Born approximation (DWBA) calculations were made to determine direct reaction contributions to inelastic neutron and proton scattering from collective levels in ^{58,60,62}Ni. Deformation parameters available from (p,p') data were used to normalize these results. Figure 18 compares results of such DWBA calculations to experimental data[28,29] from 14-MeV neutron inelastic scattering on natural nickel, which excited the first 2^+ level of each respective isotope.

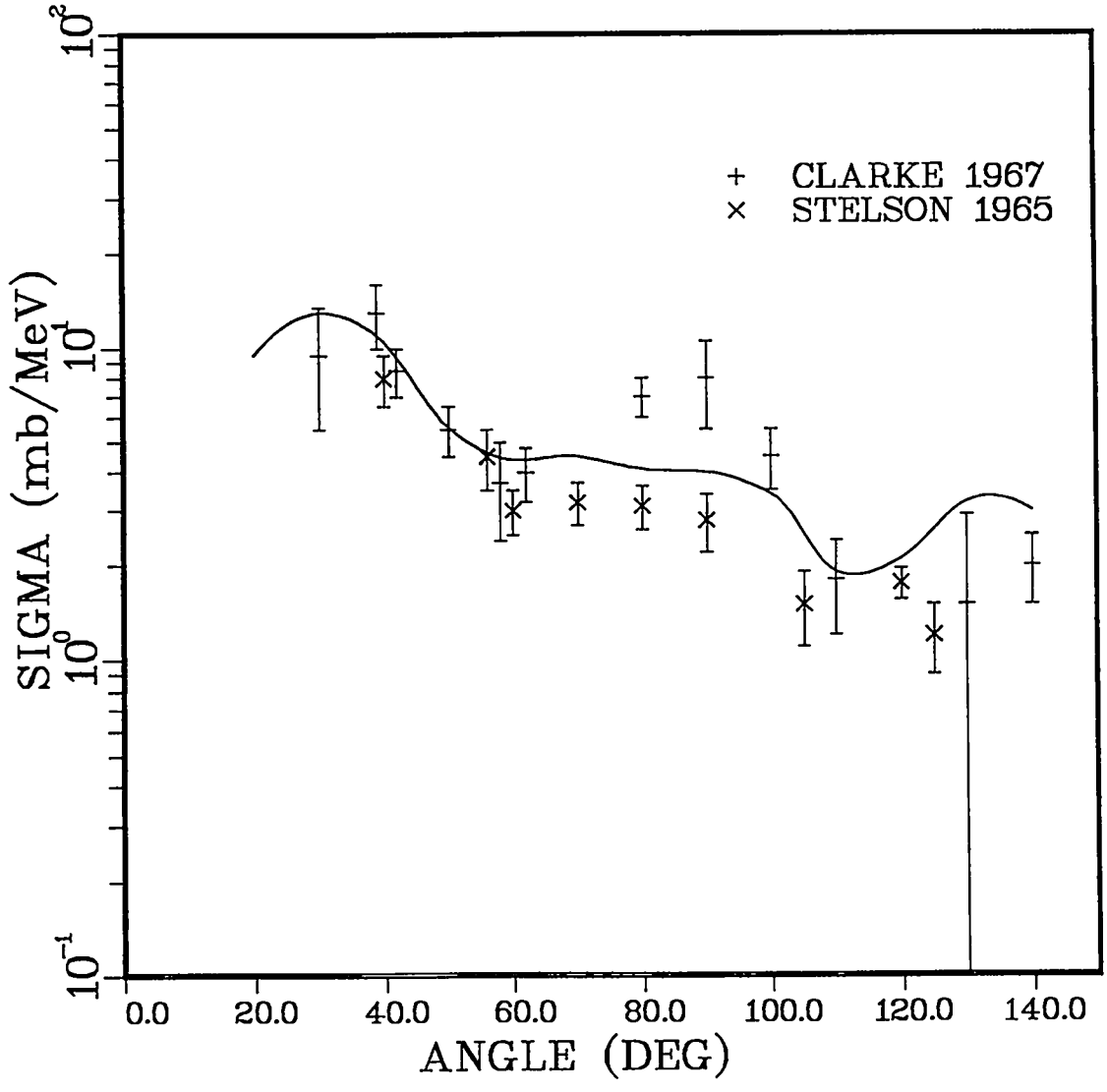

Fig. 18. Comparison of the angular distribution calculated using DWBA methods with data[28,29] measured for excitation of the first 2^+ state in nickel by 14-MeV neutron inelastic scattering.

Confirmation of model parameters, as well as calculated model results, was made through comparison with various neutron reaction cross-section data [(n,p), (n,2n), (n,xp), (n,xα), for example] available for these three nickel isotopes. Additionally, data available for (p,xn), (p,2p), (α,p) and (α,xn) reactions on nearby nuclei were also used. As an example, Figure 19 illustrates charged-particle emission spectra calculated for 15-MeV neutron reactions with ^{58}Ni. These are compared with data measured by Grimes et al.[26] Figure 20 compares calculated gamma-ray production induced by 15-MeV neutrons on ^{58,60,62}Ni with data measured by Dickens et al.[30] for 14- through 17-MeV neutrons incident on natural nickel. Finally, Fig. 21 illustrates results obtained for proton-induced reactions where calculated ^{58}Ni(p,pn) and (p,2p) excitation functions are compared with data.[31,32]

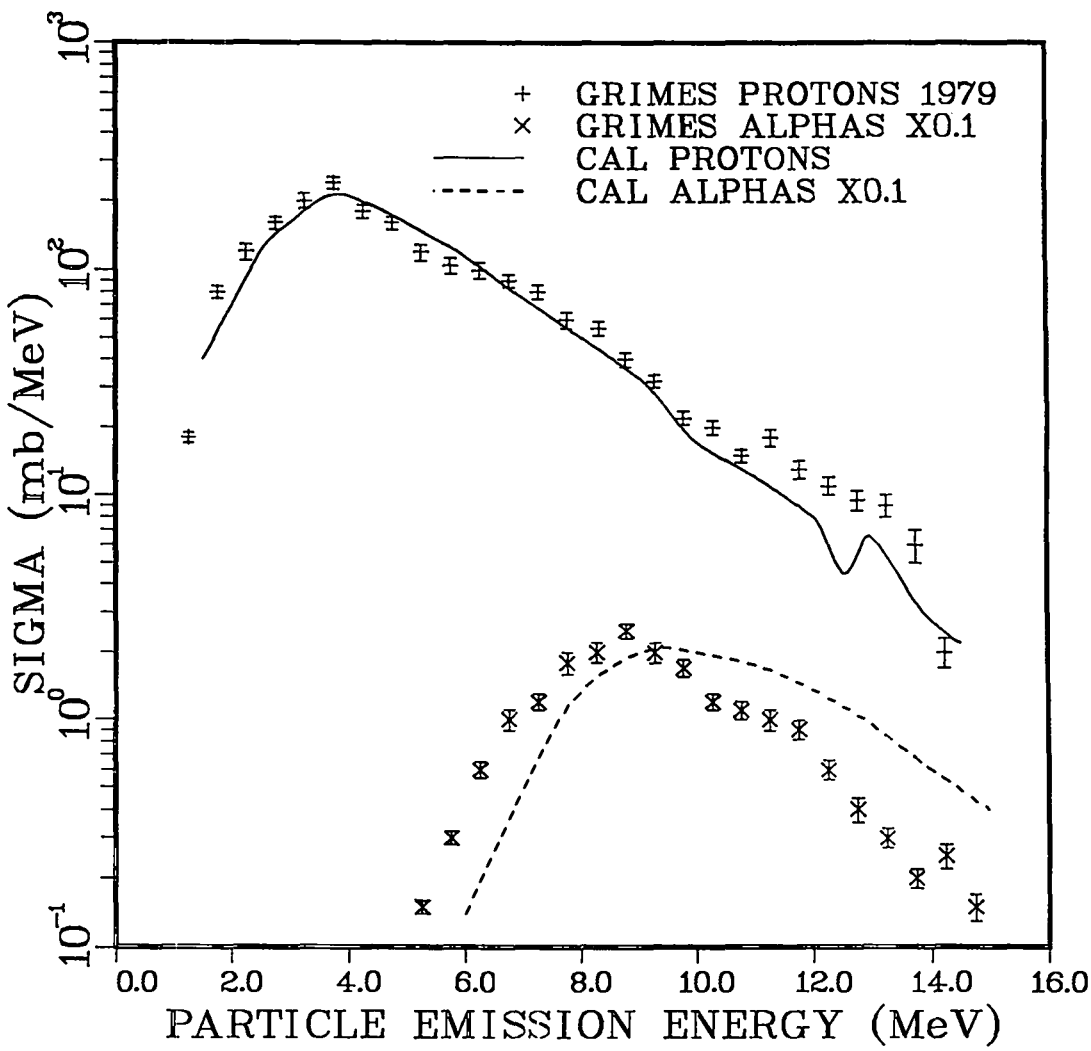

Fig. 19. Comparison of calculated charged-particle spectra produced by 15-MeV neutron reactions on ^{58}Ni with data measured by Grimes et al.[26]

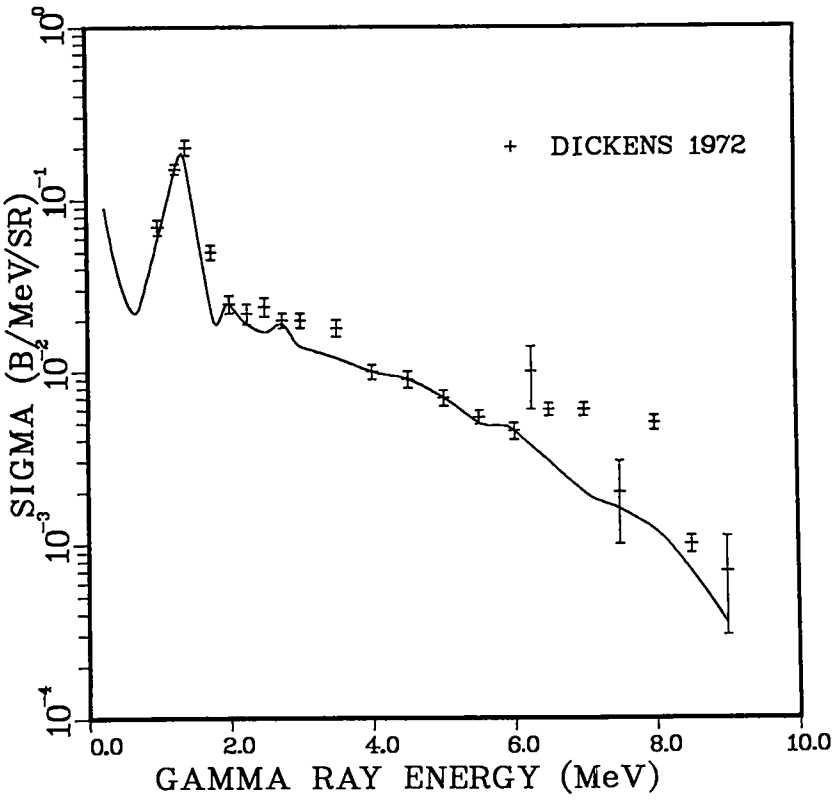

Fig. 20. Comparison of calculated gamma-ray production spectra for 15-MeV neutron interactions on nickel with the data of Dickens et al.[30]

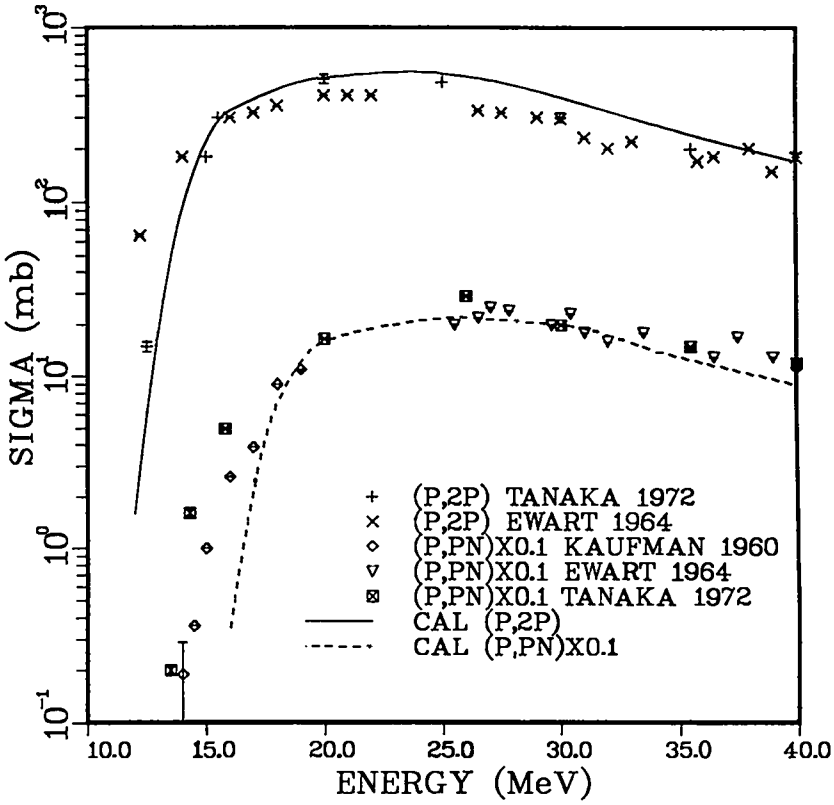

Fig. 21. Calculated ^{58}Ni (p,pn) and (p,2p) excitation functions are compared with data.[31,32]

J. Calculation of (p,X) and (n,X) Reactions on $^{63,65}Cu$ up to E_i = 50 MeV

(E. D. Arthur)

Our analysis of proton reactions on copper isotopes reported in Ref. 33 has been extended to include features required for higher energy calculations of neutron and proton reactions up to 50 MeV. These features include additional comparisons with experimental data, more careful determination of direct reaction components to inelastic scattering, as well as consideration of deuteron emission in compound-nucleus decays.

In order to include direct reaction contributions to (p,p') and (n,n') reactions, distorted wave Born approximation (DWBA) calculations were made using the neutron or proton optical model parameters described in Ref. 33. Secondly, ℓ = 2 transfers were assumed for scattering from the lowest $3/2^-$, $1/2^-$, $5/2^-$, and $7/2^-$ states in ^{63}Cu and ^{65}Cu, while the weak coupling model was used to determine relative cross sections for excitation of these levels. Finally, the overall normalization of the calculations were made using the (p,p') scattering data of Ref. 34. Figures 22 and 23 illustrate results obtained for 14-MeV proton scattering from ^{63}Cu and ^{65}Cu, respectively.

Deuteron emission was calculated using the Perey and Perey global optical model[16] parameters for deuterons. Initial verification comparisons were made with charged-particle emission spectra measured by Grimes et al.[26] for 15-MeV neutron reactions on copper. Also new results measured by Holler et al.[35] for 27-MeV $^{65}Cu(p,Xn)$ spectra provide a test of the calculated neutron emission spectra for energetic protons. Figure 24 compares our calculations for angle-integrated neutron spectra to these data where good agreement occurs. Further testing of neutron and proton reaction data is under way in preparation for the production of higher energy neutron and proton data files using these calculated results.

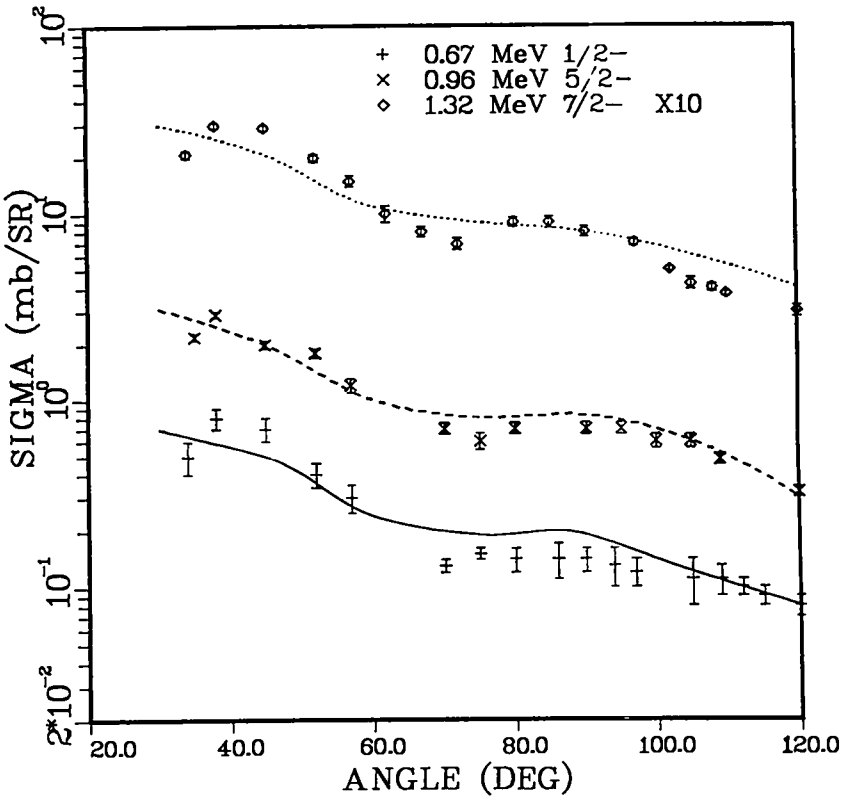

Fig. 22. Comparison of results obtained from DWBA calculations of ^{63}Cu(p,p') with the data of Ref. 34.

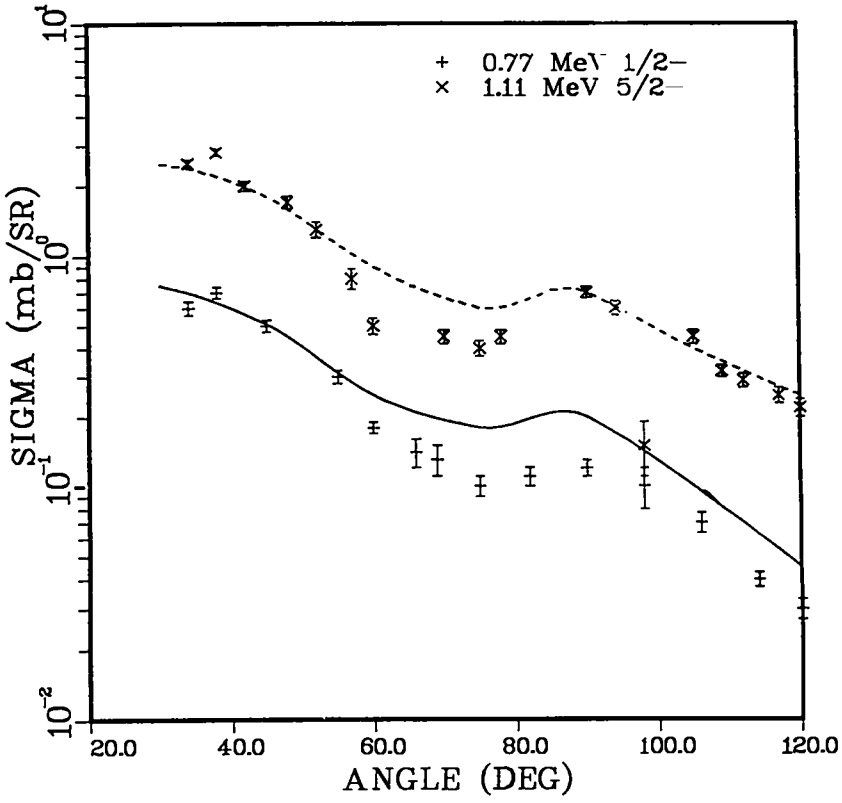

Fig. 23 Comparison of results obtained from DWBA calculations assuming ℓ = 2 transfers with the data of Ref. 34 for ^{65}Cu(p,p').

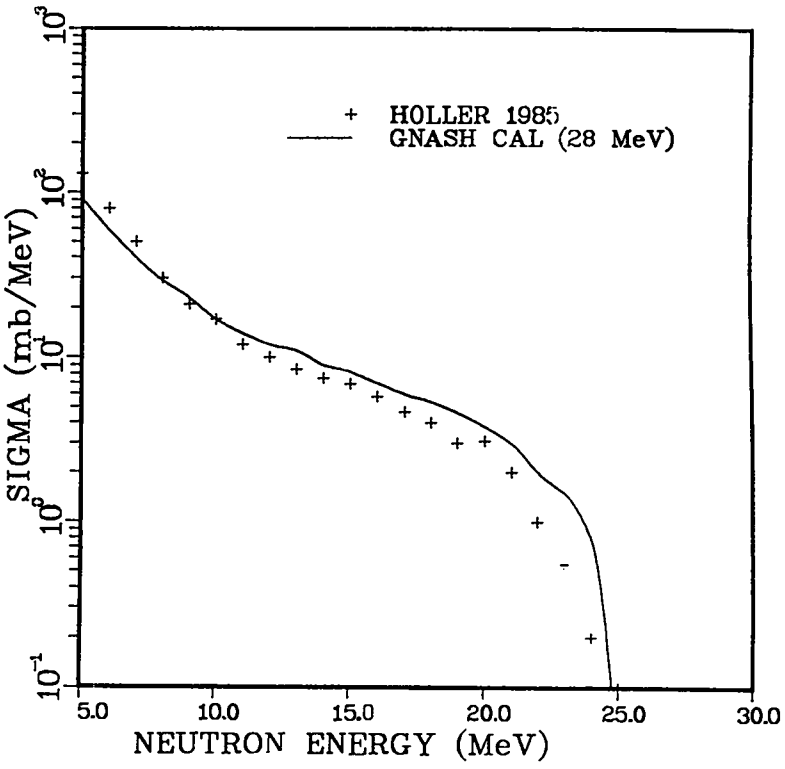

Fig. 24. Calculated neutron emission spectra produced by 27-MeV protons on ^{65}Cu are compared with the data of Holler et al.[34]

K. Extension of Theoretical Calculations of Nucleon Induced Reactions on Tungsten Isotopes to 50 MeV (E. D. Arthur)

Parameters utilized for our calculations of neutron reactions on tungsten isotopes (Ref. 36) have been extended and further verified for use at energies up to 50 MeV. A major effort was devoted to determination of Lane consistent[37] neutron and proton optical model parameters suitable for the description of nuclear reactions on tungsten or nearly deformed nuclei.

To perform the optical model studies, the coupled-channel code ECIS[38] was utilized with complex form factors and the coupling of the first three members of the ground state rotational band for the even tungsten isotopes. As a first step, calculations were made of n + ^{184}W total cross sections up to E_n = 50 MeV using the deformed optical model parameters of Ref. 36. Because of the lack of quality total cross sections for tungsten isotopes, comparisons were made with the n + ^{165}Ho data of Ref. 39. These initial comparisons indicated that the energy dependence of the real potential of Ref. 36 was too strong, so that this coefficient was lowered from -0.4 to -0.25. In addition, the volume imaginary potential form was charged to W_{vol} = -1.8 + 0.12E. These parameters produced good agreement with n + ^{165}Ho total cross section data up to E_n = 70 MeV. This comparison appears in Fig. 25. Using these parameters as a basis, proton optical parameters were derived and utilized in comparisons with proton elastic and

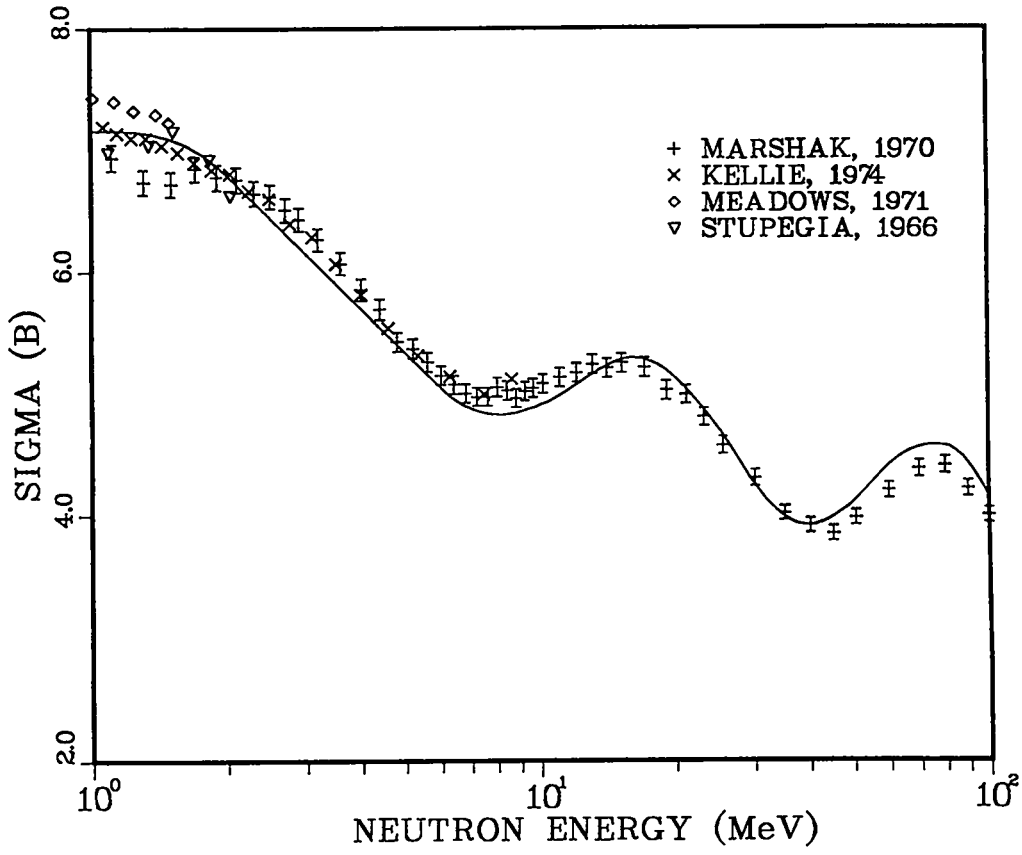

Fig. 25. Comparison of n + ^{165}Ho total cross sections calculated using the adjusted neutron optical parameters described in the text.

inelastic scattering data at 16 and 55 MeV.[40,41] Good agreement was obtained as illustrated in Figs. 26 and 27. Finally, GNASH[8] calculations were made of ^{182,184}W(n,2n) cross sections to further test the neutron optical parameters described above. As a result of these calculations, the imaginary volume potential was adjusted to W_{vol} = -0.7 + 0.12E. This was necessary to correct a significant underprediction of 13-14 MeV (n,2n) data. A comparison of the calculated ^{184}W(n,2n) results using these adjusted parameters with the Frehaut data[42] appears in Fig. 28. Finally, Table V lists the neutron and proton optical model parameters utilized for calculation of proton and neutron reactions on ^{182}W and ^{184}W up to 50 MeV.

Comparisons of calculations made using these optical parameters are under way for ^{183}W and ^{186}W. Preliminary results indicate the need for additional parameter adjustment in order to adequately describe ^{186}W(n,2n) data while maintaining a compatibility for higher energy calculations.

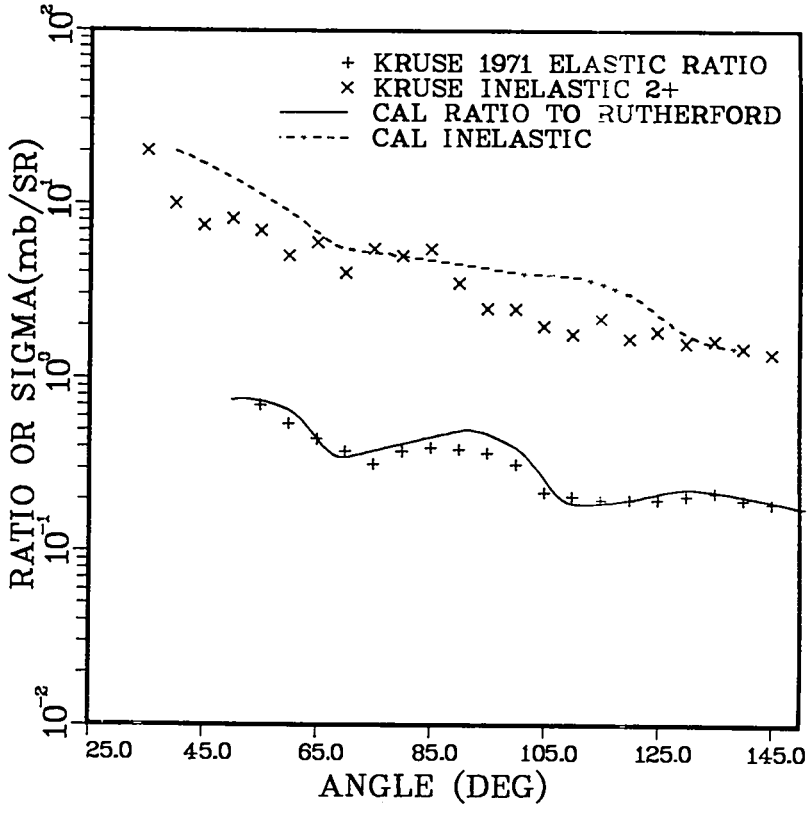

Fig. 26. Comparison of calculated elastic and inelastic scattering angular distributions for 16-MeV proton interactions on ^{184}W with the data of Ref. 40.

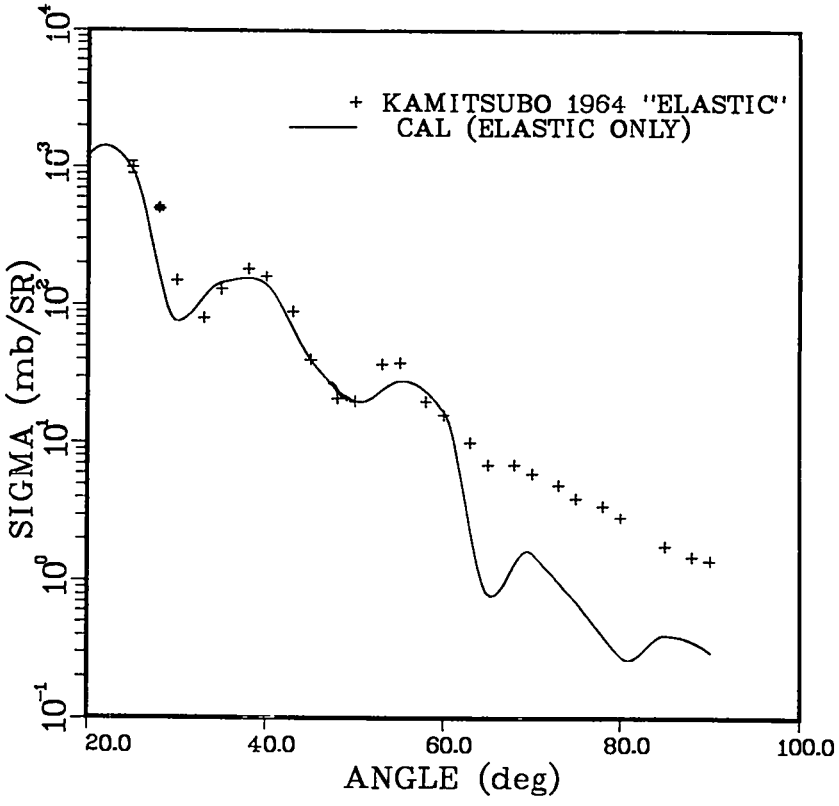

Fig. 27. "Elastic" scattering angular distributions calculated for 55 MeV proton reactions on ^{184}W are compared with the data of Ref. 41.

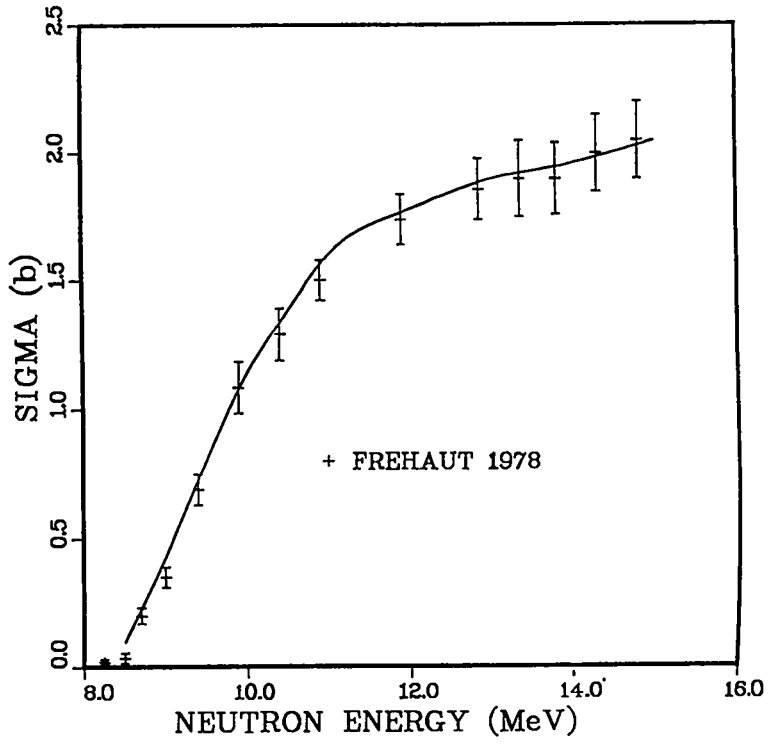

Fig. 28. Calculated $^{184}W(n,2n)$ cross sections using the neutron optical parameters of Table V are compared with the Frehaut[42] data.

TABLE V

DEFORMED OPTICAL MODEL PARAMETERS USED FOR $^{182,184}W$ CROSS-SECTION CALCULATIONS[a]

		r	a
Neutrons			
V	= 46.66 - 0.25E	1.26	0.61
W_{vol}	= -0.7 + 0.12E	1.26	0,61
V_{SO}	= 7.5	1.26	0.61
W_{SD}	= 3.4 + 0.76E	1.24	0.45
	Above E_n = 45 MeV		
W_{SD}	= 6.82 - 0.1E		
Protons			
V	= 58.065 - 0.25E	1.26	0.61
W_{vol}	= -1.8 + 0.12E	1.26	0.61
V_{SO}	= 7.5	1.26	0.61
W_{SD}	= 6.95 - 0.76E	1.24	0.45
	Above E_n = 4.5 MeV		
W_{SD}	= 9.95 - 0.1E		
r_c	= 1.25		
β_2	= 0.209		
β_4	= -0.056		

[a]All well depths in MeV; geometrical parameters and charge radius, r_c, in Fermis.

L. Systematic Recalculation of Cross Sections for Neutron Reactions on Yttrium Isotopes [J. Hurd (INC-11) and E. D. Arthur]

We have begun an effort to systematically re-evaluate data required for calculations of neutron reactions on yttrium isotopes. These new results will then be used to redetermine nuclear cross-section data originally reported in Ref. 43. Although several isolated calculational efforts have occurred over the past several years to improve specific types of reaction data, new information, particularly that reported in Ref. 44, indicates the need for a complete recalculation.

As an initial step, we have systematically evaluated and updated nuclear level information for yttrium isotopes (^{86,87,88,89}Y) and strontium isotopes (^{86,87,88,89}Sr). This was accomplished using information available from the most recent Nuclear Data Sheets[45] as well as examination of relevant experimental information available since 1980.

With this update of nuclear level information in hand, we have begun verification of improved neutron optical model parameter sets. This will be followed by investigation of gamma-ray strength functions using recent ^{86}Sr(p,γ) data.* At that time, preparations should essentially be complete so that final Hauser-Feshbach, preequilibrium, and perhaps distorted-wave calculations can begin.

M. Comparison of Calculated ^{239}Pu(n,2n) Cross Sections with New Experimental Data (E. D. Arthur)

In Ref. 46 we reported, as part of a larger theoretical analysis of n + ^{239}Pu cross sections, calculated ^{239}Pu(n,2n) cross sections to 20 MeV. At that time reliable data** existed only for neutron energies around 14 MeV. Recently, new measurements of the ^{239}Pu(n,2n) cross section have been reported by Frehaut et al.,[47] which are compared with our theoretical predictions in Fig. 29. The theoretical calculations (performed in 1983) are verified by these new measurements. Also verified is the theoretical technique used to determine multichance fission cross section components that compete with multiple neutron emission. These techniques, as reported in Ref. 48, incorporated consistent analyses of data available from charged-particle induced fission probability measurements, which are linked through appropriate theoretical models to calculation of (n,xf) data.

*R. Gilmore, INC-11, Los Alamos National Laboratory provided this information in 1984.

**Information supplied by R. Lougheed, Lawrence Livermore National Laboratory in 1985.

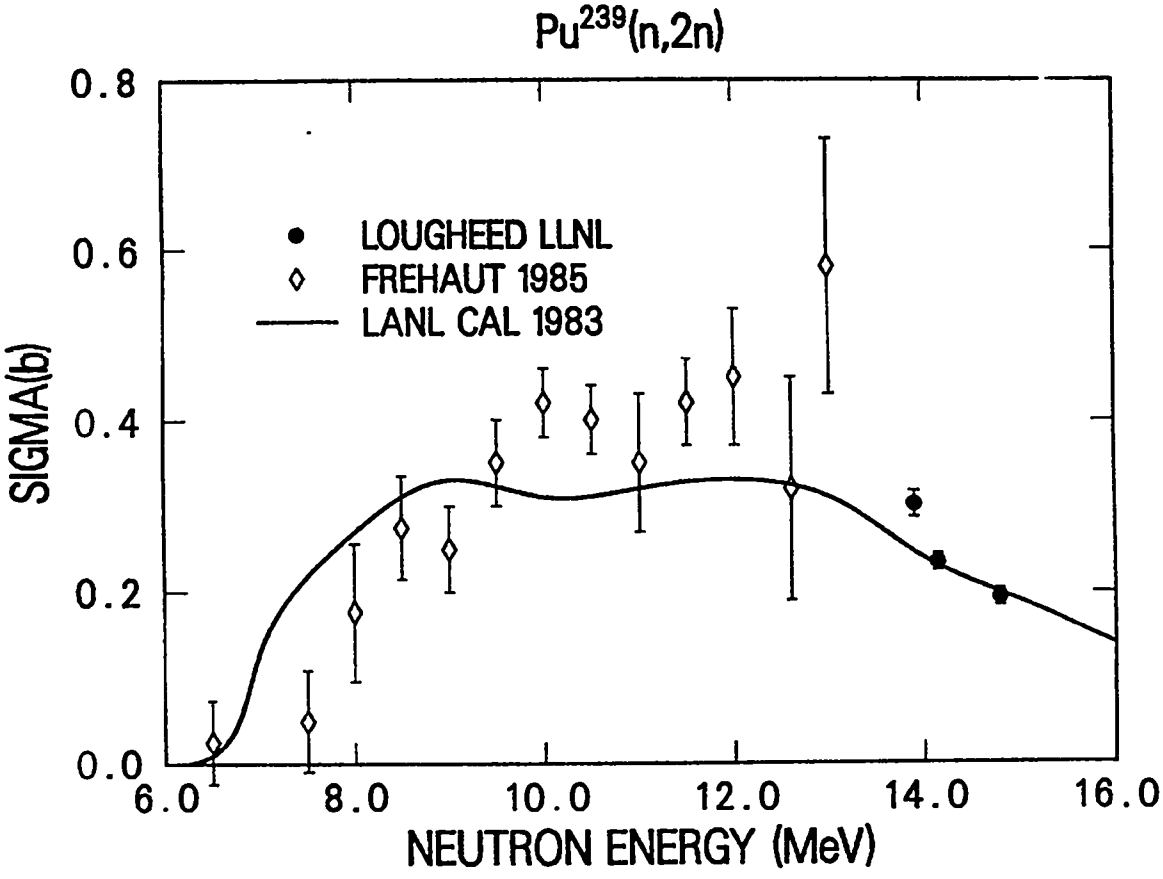

Fig. 29. Theoretical calculations of ^{239}Pu(n,2n) cross sections reported in Ref. 46 are compared with new data measured by Frehaut et al.[47]

N. Global Spherical Optical Model Potentials for Neutrons (P. G. Young)

In a review of global and local optical model parameterizations,[49] the performance of seven global neutron potentials in describing experimental s- and p-wave neutron strengths (S_0,s_1), potential scattering radii (R'), and neutron total cross sections (σ_{total}) was examined. The spherical optical model (SOM) potentials considered here are summarized in Table VI.[50-56] The oldest potential considered is the 1963 Moldauer potential[50] and the most recent is the 1985 potential of Walter and Guss,[56] still under development.

Figures 30 and 31 compare values of S_0 and S_1 calculated from the global parameterizations* in Table VI with values inferred from experimental data.[57] Similarly, Fig. 32 compares calculated R' values with "measurements." Note that the Engelbrecht and Fiedeldey potential[52] is not included but is equivalent to the Moldauer[50] potential at low energies. The SOM computer code SCAT79, developed by Bersillon,[58] was used in all the spherical optical calculations.

*All S_0, S_1, and R' calculations in this paper are for 10-keV neutrons.

TABLE VI

NEUTRON SOM GLOBAL POTENTIALS[a]

Reference	Potentials	r_i, a_i (fm)	c_i (fm)
Moldauer, 1963[50]	V_R = 46.0	1.16, 0.62	0.6
E ≲ 1 MeV	W'_D = 14.0	1.16, 0.50	1.1
A > 40	V_{SO} = 7.0	1.16, 0.62	0.6
Note: Based on fits to s_0, σ_T, and $\sigma_E(\theta)$ data for neutrons below 1 MeV, A = 40-150.			
Wilmore and Hodgson, 1964[14]	V_R = 47.01-0.267E-0.0018E^2	1.322-(7.6-4)A+(4.0-6)A^2-(8.0-9)A^3, 0.66	0
E ≲ 15 MeV			
A > 40 MeV			
	W_D = 9.52-0.053E	1.266-(3.7-4)A+(2.0-6)A^2-(4.0-9)A^3, 0.48	0
Note: Derived from the non-local, energy-independent potential of Perey and Buck.[51]			
Engelbrecht and Fiedeldey, 1967[52]	V_R = 46.0 exp[-0.0067E-(2.0-6)E^2]	1.16, 0.62	0.6
	W'_D = 14.0 exp[-0.017E-(1.2-4)E^2]	1.16, 0.50	1.1
E = 0-155 MeV	W_V = 0.126E exp[-0.001102$E^{1.28}$]	1.16, 0.62	0.6
A = 40-210	V_{SO} = 7.0 exp[-0.0067E-(2.0-6)E^2]	1.16, 0.62	0.6
Note: Developed from a non-local potential similar to Perey and Buck[51] but including volume absorption. Constrained to match Moldauer[50] potential at $E_n \sim 0$.			
Becchetti and Greenlees, 1969[53]	V_R = 56.3-0.32E-24.0η	1.17, 0.75	0
	W_D = 13.0-0.25E-12.0η	1.26, 0.58	0
E < 50 MeV	W_V = 0.22E-1.56	1.26, 0.58	0
A > 40	V_{SO} = 6.2	1.01, 0.75	0
Note: Starting from a proton potential based on fits to extensive $\sigma_E(\theta)$, $P(\theta)$ data for E_p = 10-40 MeV and A = 58-208, fit neutron σ_T and $\sigma_E(\theta)$ for E_n = 1-24 MeV, A = 56 - ^{209}Bi.			

[a]Energies in MeV; η = (n-Z)/A; exponential notation example: (7.6-4) = 7.6 x 10^{-4}.

TABLE VI (Cont.)

Reference	Potentials		r_i, a_i (fm)	c_i (fm)
Patterson et al.,	V_R = 55.8-0.32E-17.7η		1.17, 0.75	0
1976[54]	W_D = 9.6-0.22E-(18.1-0.31E)η		1.32, 0.51+0.7η	0
E = 7-24 MeV	W_V = -1.4+0.22E		1.32, 0.51+0.7η	0
A = 27-209	V_{SO} = 6.2		1.01, 0.75	0
Note: Using Lane model,[37] determined isoscalar potential from Becchetti and Greenlees[53] analysis and isovector potential from (p,n) angular distributions at E_p = 25-45 MeV, A = 48-208. Neutron data used only for comparisons.				
Rapaport et al.,	V_R = 54.19-0.33E-(22.7-0.19E)η		1.198, 0.663	0
1979 (Set A)[55]	W_D = 4.28+0.4E-12.8η	E ≦ 15	1.295, 0.59	0
E = 7-26 MeV	= 14.0-0.39E-10.4η	E > 15		
A = 40-208	W_V = 0	E ≦ 15	1.295, 0.59	0
	= -4.3+0.38E	E > 15		
	V_{SO} = 6.2		1.01, 0.75	0
Note: Fit neutron elastic angular distributions between 7-26 MeV for singly or doubly closed shell nuclei only in the range A = 40-208.				
Walter and Guss,	V_R = 52.56-0.31E-(16.5-0.081E)η	E<40	1.219, 0.688	0
1985[56]	= 52.56-12.4 [1+ℓn (E/40)]			
E = 10-80 MeV	+ {16.5-3.24 [1+ℓn(E/40)]}η	E>40		
A > 53	W_D = 10.85-0.157E-14.94η	E>9.9	1.282, 0.512	0
	W_V = -0.963+ 0.153E	E<39.4	1.38+3.76/A, 0.557-0.462/$\sqrt{A}$	0
	= -0.963+0.153E · [1-0.33ℓn (E/39.4)]	E>39.4		
	V_{SO} = 5.767-0.015E+2η		1.103, 0.560	0
	W_{SO} = 0.791-0.018E		1.364, 0.632	0
Note: Using Lane model formulation, fit neutron σ_T, $\sigma_E(\theta)$, $A(\theta)$ between 10 and 40 MeV, and proton $\sigma_E(\theta)$, $A(\theta)$ between 20 and 85 MeV for A = 54-209.				

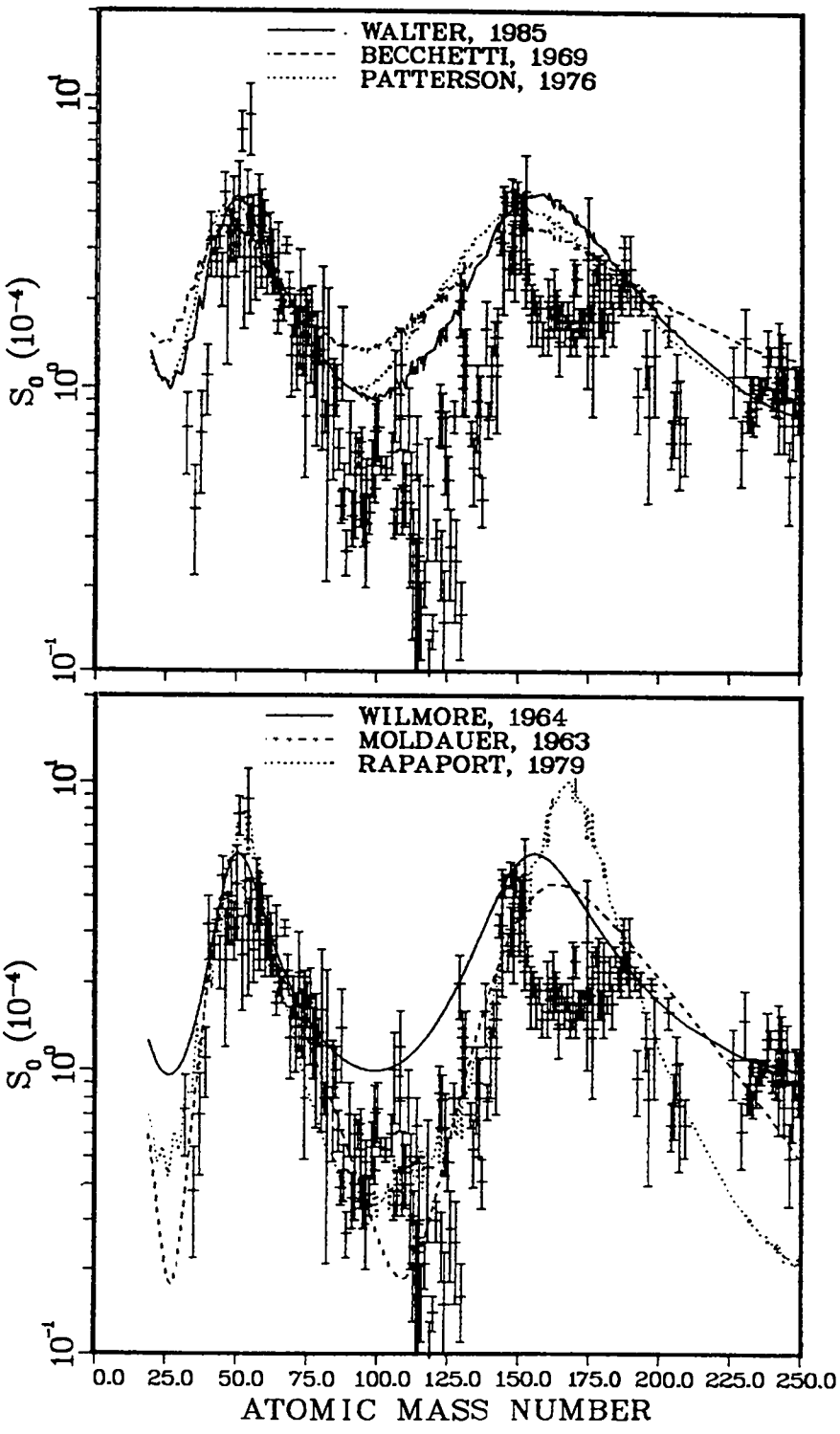

Fig. 30. Comparison of calculated s-wave neutron strength functions for six global SOM potentials with experimental values for A = 20-250.

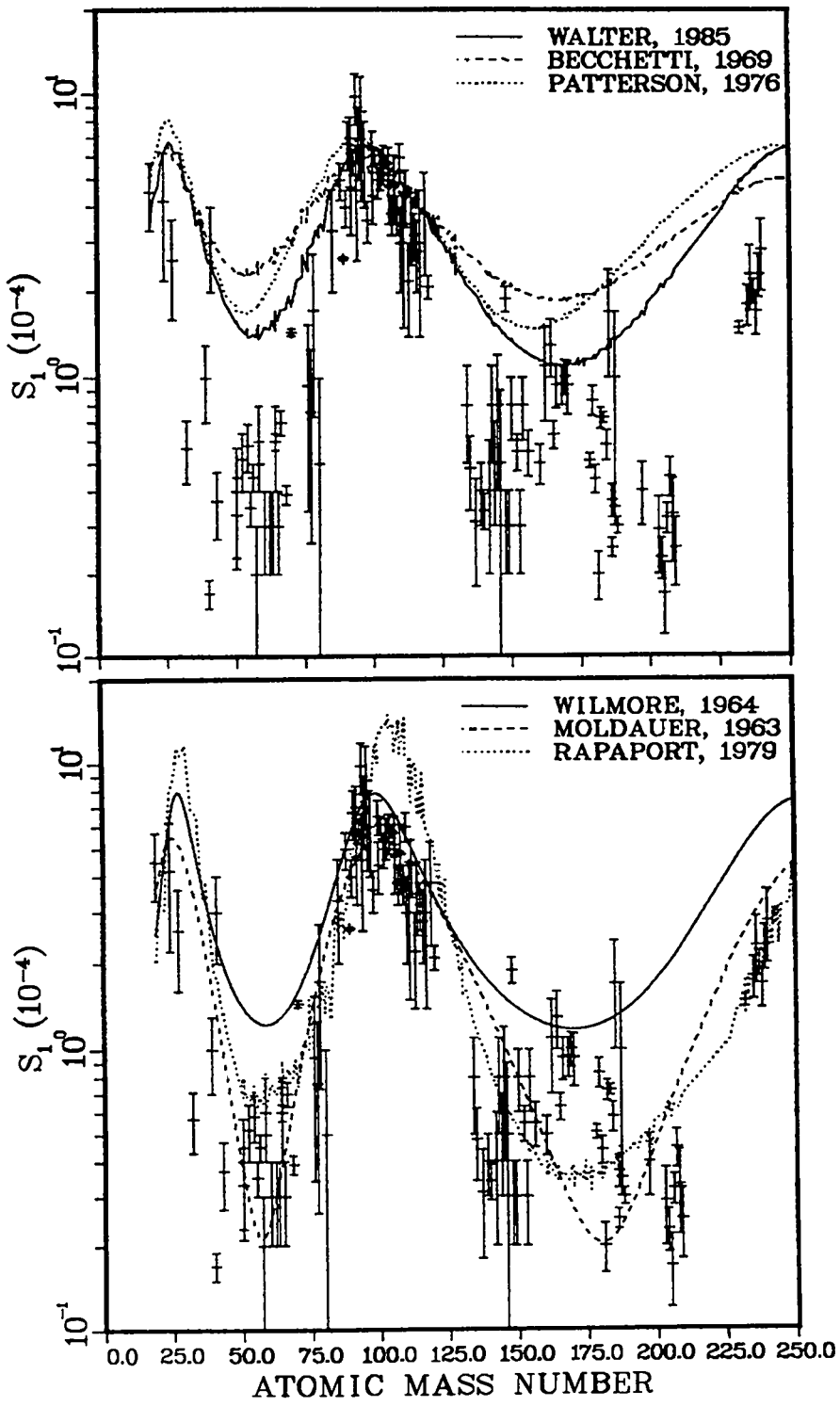

Fig. 31. Comparison of calculated p-wave neutron strength functions for six global SOM potentials with experimental values for A = 20-250.

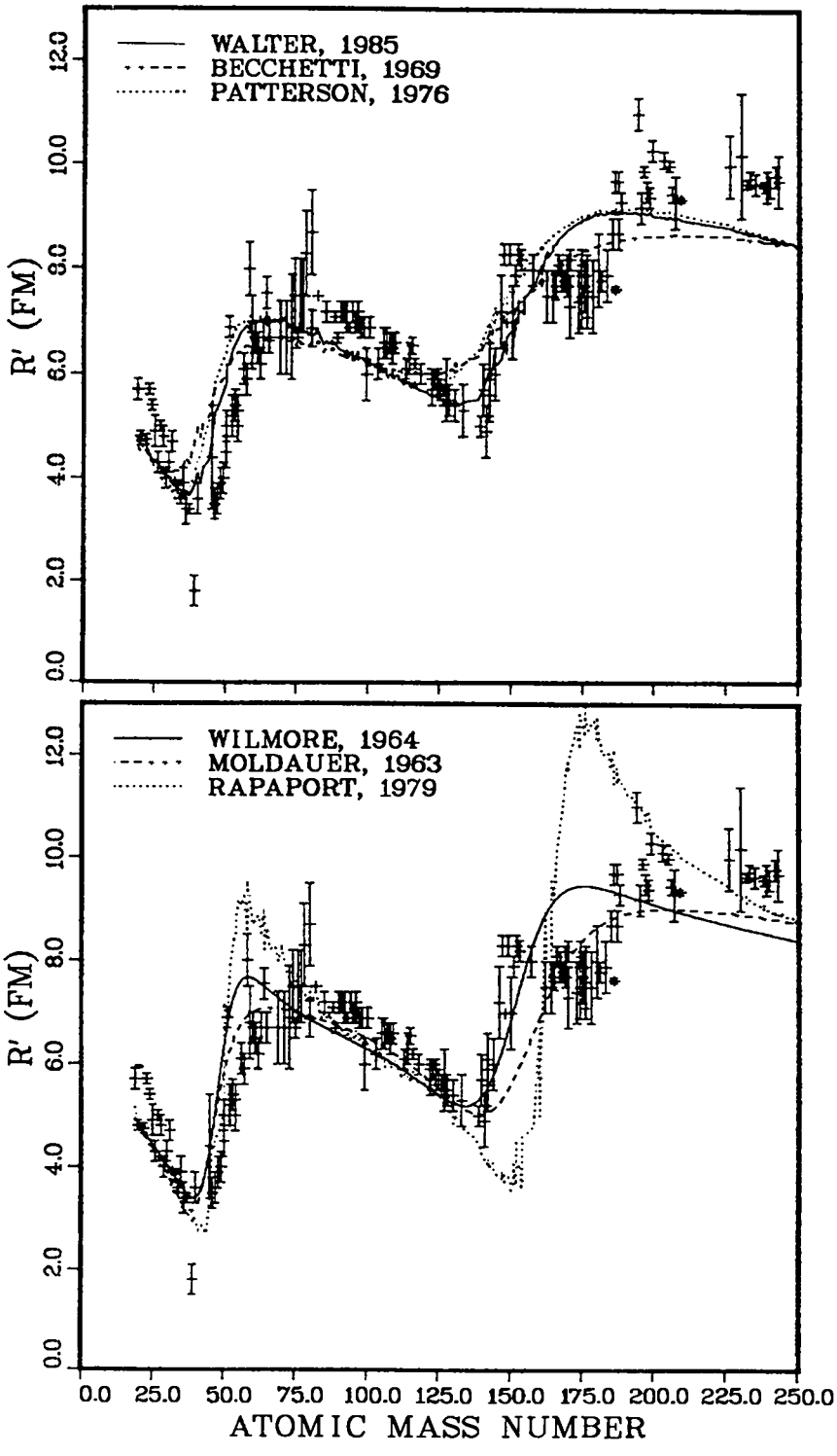

Fig. 32. Comparison of calculated potential scattering radii for six global SOM potentials with experimental values for A = 20-250.

Overall, the Moldauer potential appears to best reproduce the S_0, S_1 and R' experimental results. This is not surprising, of course, because that analysis focussed on low neutron energies and used S_0 in its fits. The largest deviations from experiment are seen in the rare earth and actinide regions, where static deformations are large. Concentrating on the mass range below 150, where the spherical potentials have more validity, it appears that the three newer potentials of Patterson et al.,[54] Rapaport et al.,[55] and Walter[56] reasonably represent the measurements. In general, these three potentials appear to reproduce the data about as well as the Wilmore and Hodgson potential, and somewhat better than Becchetti and Greenlees.

Neutron total cross sections calculated from the potentials of Table VI are compared with experimental data[59] for Ca and ^{89}Y in Figs. 33 and 34. Also included are calculations with the regional potential of Kawai,[60] developed and used for structural materials. The measurements have been rather grossly averaged to reduce some of the structure effects. None of the potentials follow the experimental values for Ca particularly well below ~ 4 MeV. At higher energies several potentials do reasonably well, especially those of Moldauer, Walter, Patterson, and Rapaport. The same low energy problems occur for Ni (see Sec. 0) except they are less severe and are mainly below 3 MeV.

Similar comparisons for the total cross sections of ^{150}Nd and ^{238}U are given in Figs. 35 and 36, together with the regional fission product potential of Igarasi[61] and the regional (SOM) actinide potential of Madland and Young,[62] which stops at 10 MeV. These nuclei have significant static deformations, so the large deviations seen in Figs. 35 and 36 are not surprising, with the general features of minimum undershoot and maximum overshoot. In the case of ^{238}U, reasonable agreement with experiment is seen only for the actinide spherical potential of Madland and Young.

In summary, the newer global potentials of Patterson, Rapaport, and Walter (and particularly the latter two) appear to follow the low-energy S_0, S_1, R' data, and the σ_T results for $A < 150$, $E \leq 20$ MeV as well as or better than the pre-1970 potentials. Of the older global sets, the Wilmore potential has the most overall consistency with the σ_T data to 20 MeV. To draw any finer distinctions, it is necessary to look in more detail at the potentials.

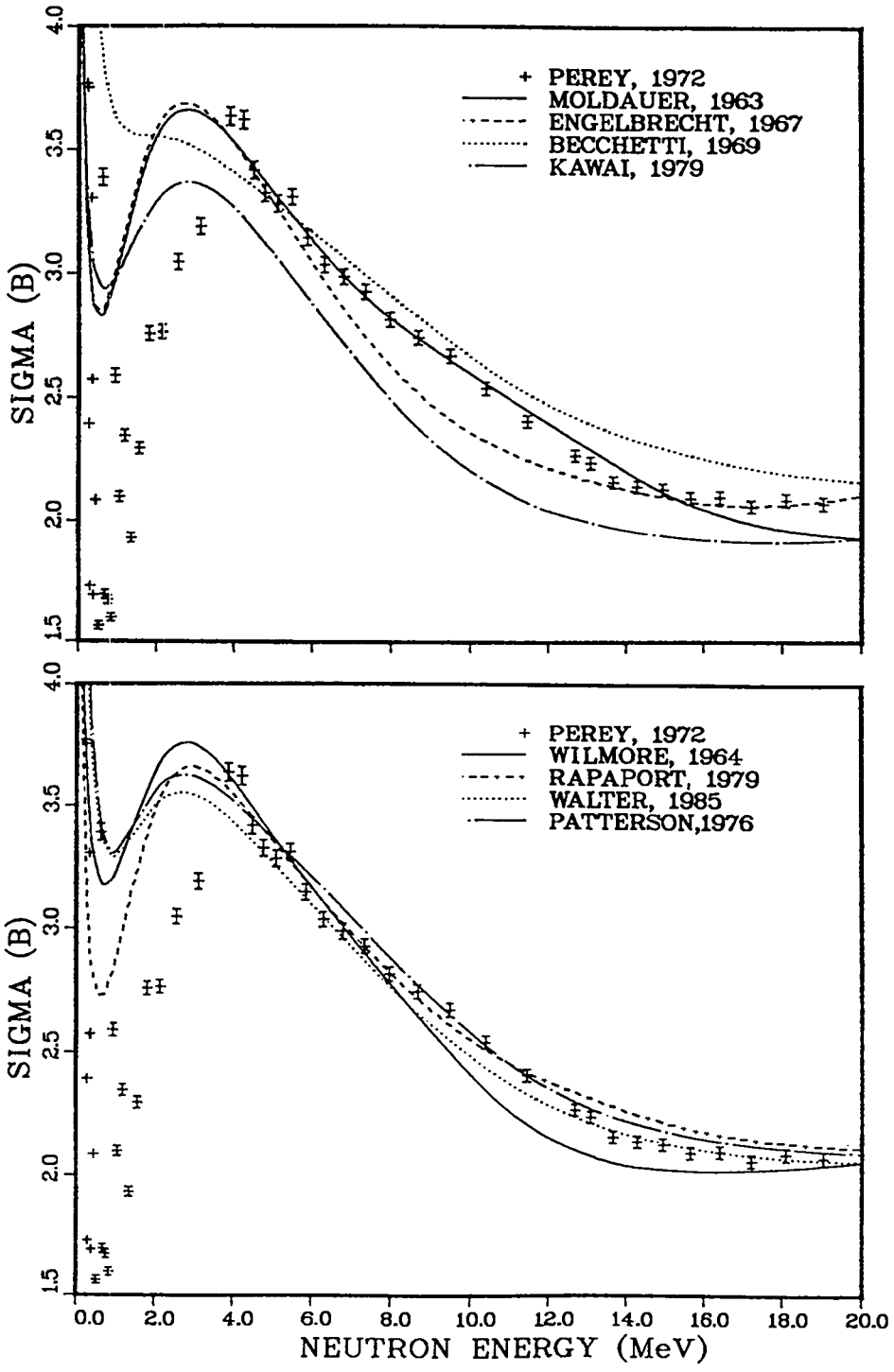

Fig. 33. Comparison with Ca experimental total cross-section data of 8 SOM potentials for neutron energies between 0.5 and 20 MeV.

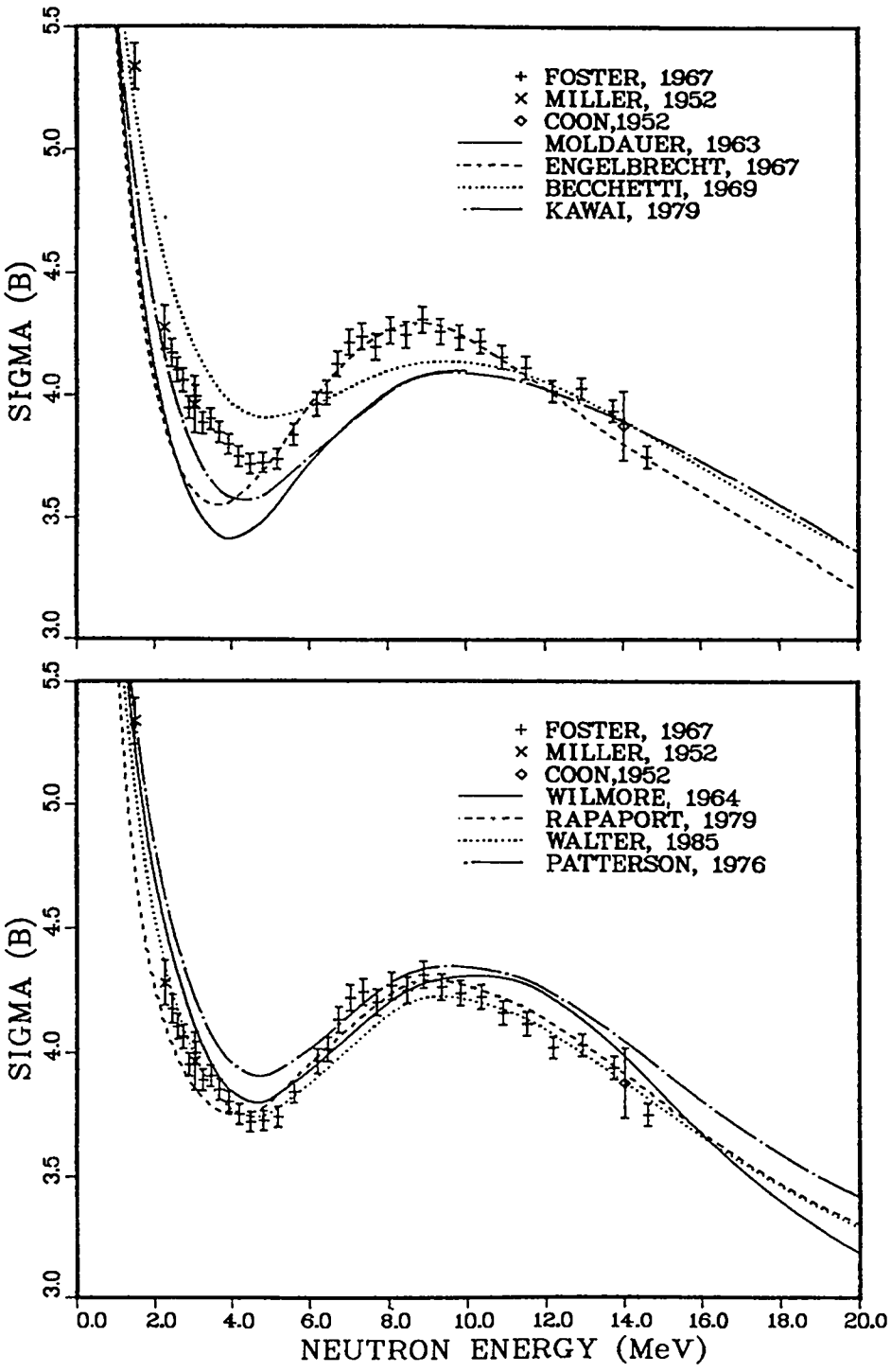

Fig. 34. Comparison with ^{89}Y experimental total cross-section data of 8 SOM potentials for neutron energies between 0.5 and 20 MeV.

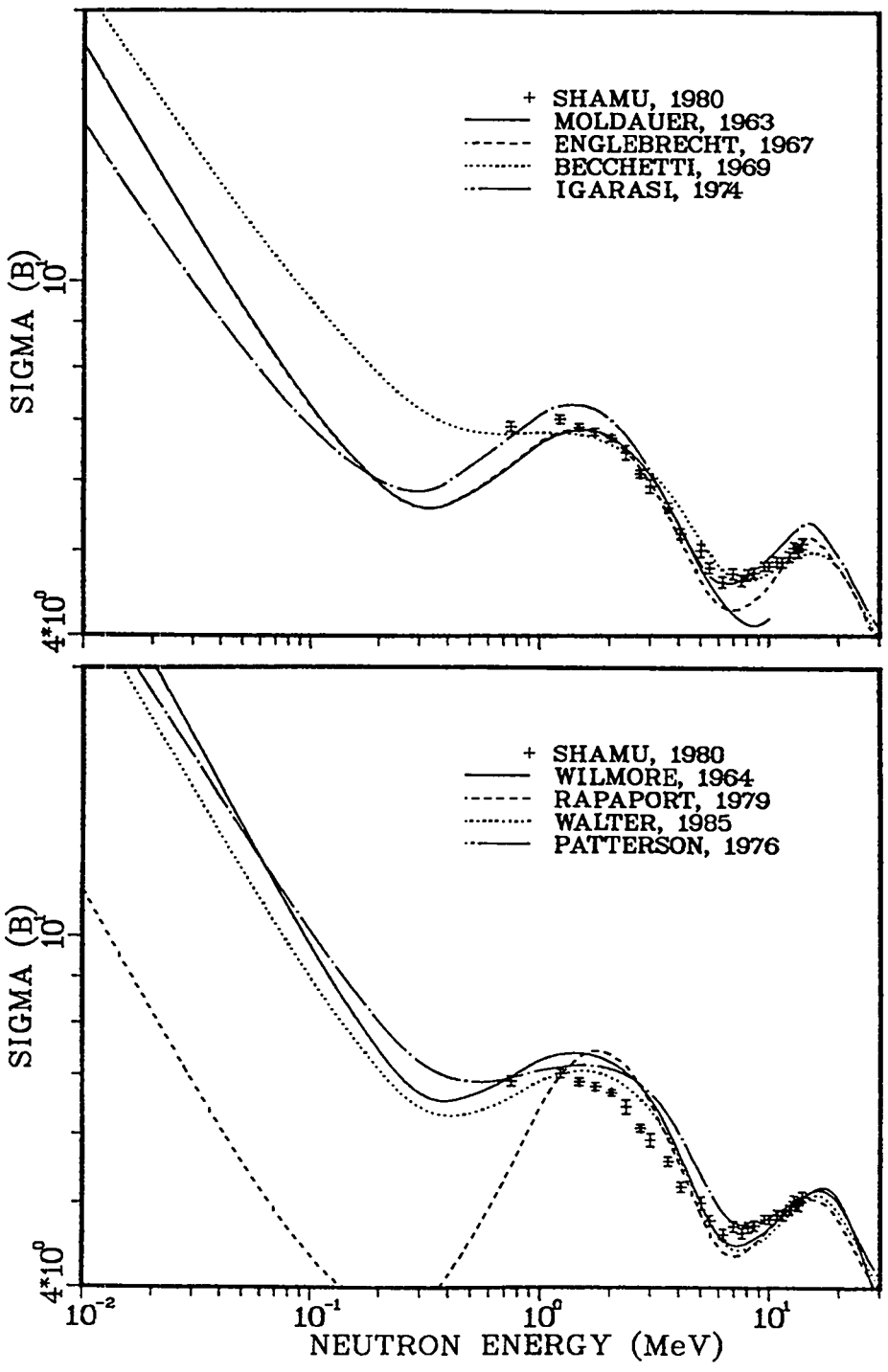

Fig. 35. Comparison with ^{150}Nd experimental total cross-section data of 8 SOM potentials for neutron energies between 0.01-30 MeV.

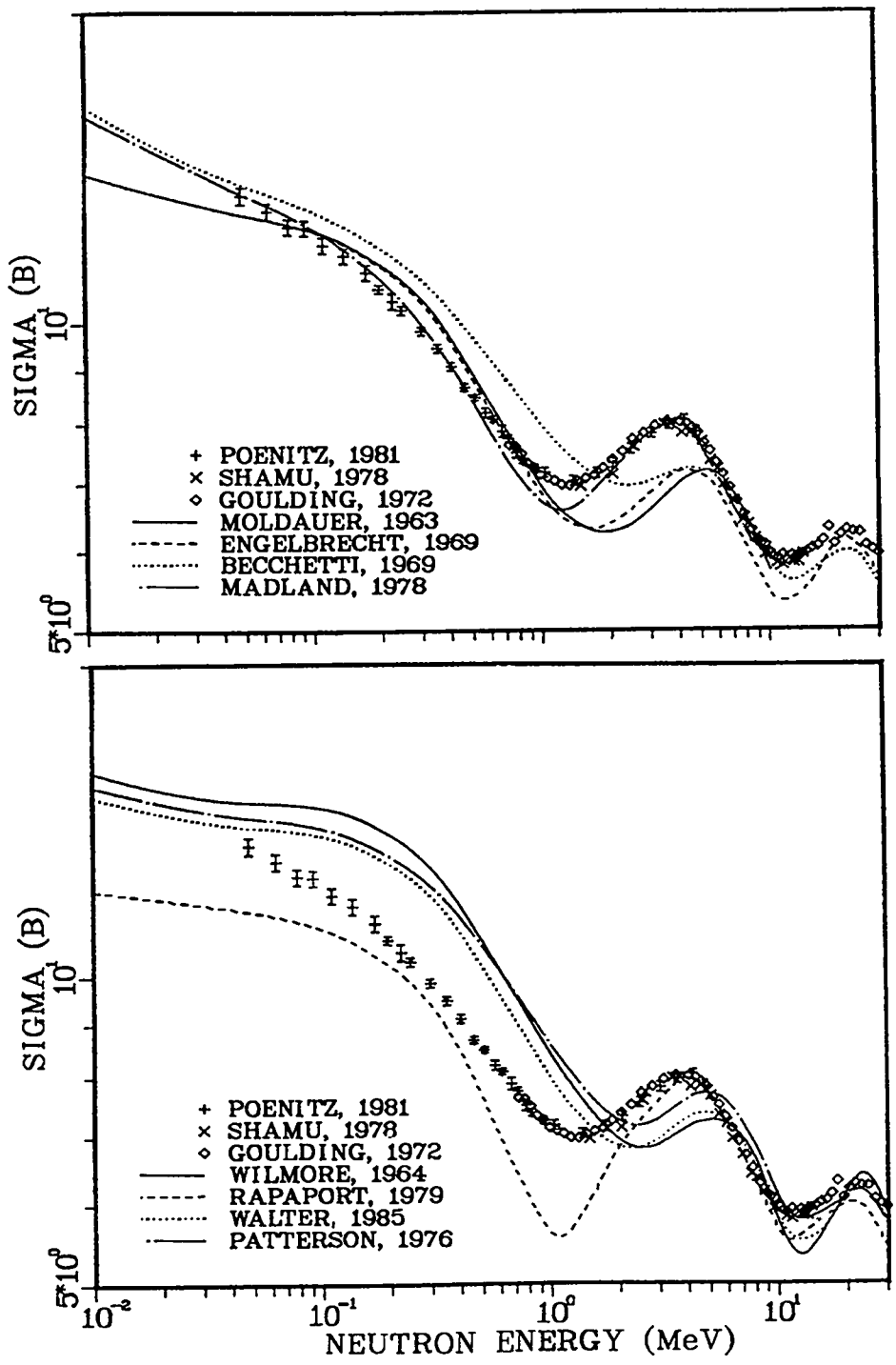

Fig. 36. Comparison with ^{238}U experimental total cross-section data of 8 SOM potentials for neutron energies between 0.01-30 MeV.

O. Performance of Global Optical Potentials in Calculations of n + ^{58}Ni Reactions (P. G. Young)

To examine the global optical model potentials of Sec. N more closely in the structural material region, detailed calculations of n + ^{58}Ni reactions were performed.

Figure 37 includes comparisons of ^{58}Ni total, shape elastic, and reaction cross sections, calculated with the potentials of Table VI, at neutron energies between 10 keV and 20 MeV. Large differences (20-30%) are evident among the various potentials. The weakest agreement with σ_T measurements is at low energies, where the Becchetti potential in the upper part of the figure and all the potentials in the lower part are ~ 20% higher than experiment from 0.7-2.0 MeV. Significant differences also occur among the calculated shape elastic and reaction cross sections. The most obvious outrider in the comparisons is the high Becchetti reaction cross section at most energies and the relatively low Becchetti shape elastic cross section from ~ 2-10 MeV.

The differences in reaction cross sections seen in Fig. 37 should be manifest in calculations of specific partial reaction cross sections. To quantify these effects, Hauser-Feshbach statistical-theory calculations were performed for each of the potentials illustrated in Fig. 37, as well as for three local potentials. The COMNUC[63] and GNASH[8] code systems were utilized for the calculations with no attempt being made to optimize parameters. Width fluctuation corrections were included at neutron energies below 5 MeV, and channels for outgoing protons and alphas, in addition to neutrons and gammas, were provided at all energies. Experimentally-observed discrete levels were included for each residual nucleus, matched smoothly to continuum level representations using the Gilbert and Cameron[64] formalism and Cook[65] parameter tables. Direct reaction contributions were estimated for low-lying ^{58}Ni levels using a single set of DWBA calculations with the Harper[66] local potential. Optical model parameterizations for protons and alphas from Harper's ^{58}Ni analysis[66] were utilized to calculate charged-particle transmission coefficients. A giant-dipole resonance shape was used for the E1 gamma-ray strength function, with a single normalization factor based on ^{58}Ni(n,γ) measurements near 100 keV. The comparison calculations were made by changing inputted neutron transmission coefficients from the various spherical potentials, leaving all other parameters constant.

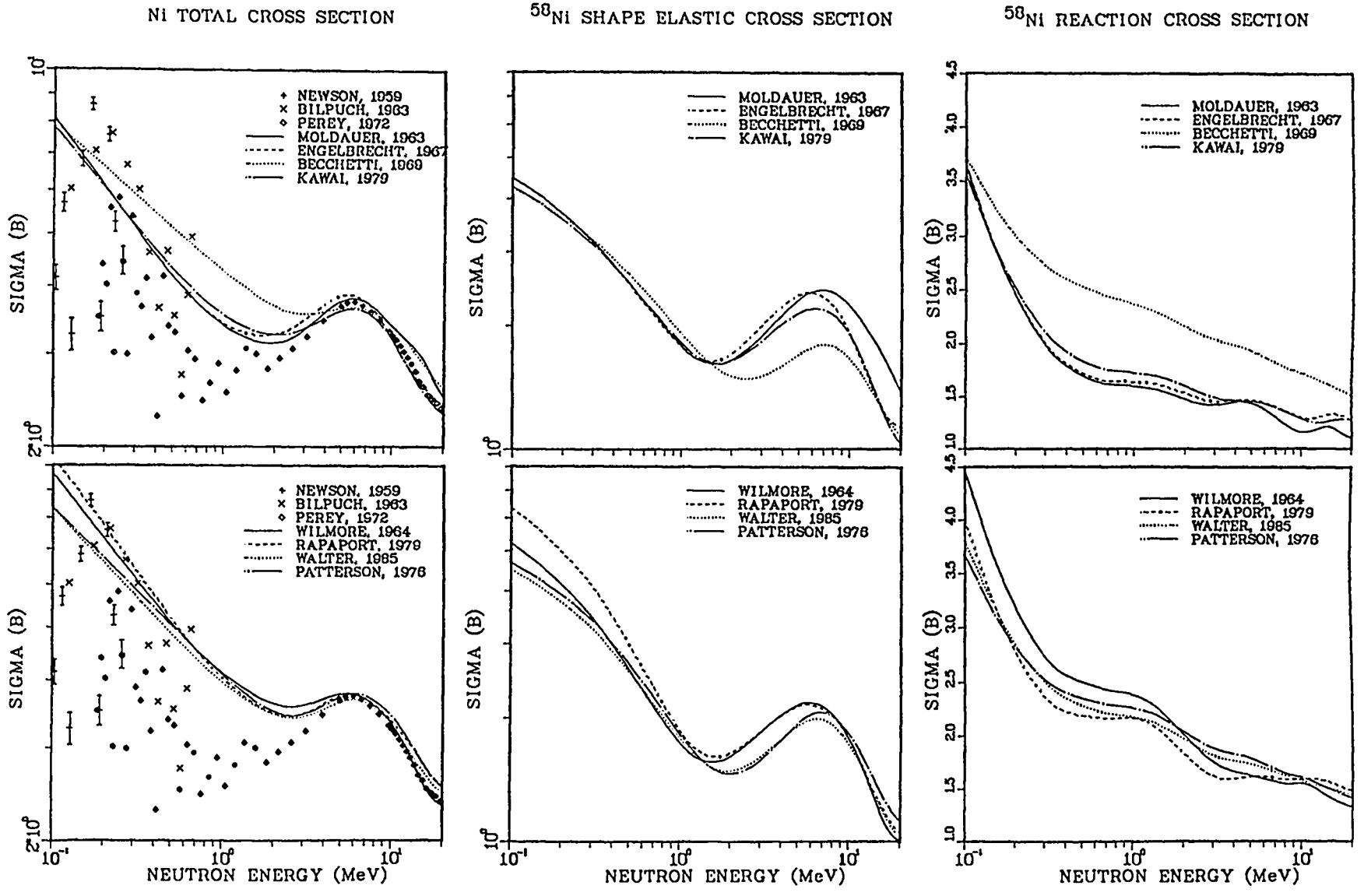

Fig. 37. Comparison of ^{58}Ni total, shape elastic, and reaction cross sections calculated with 8 SOM potentials for neutron energies 0.1-20 MeV. The experimental σ_T data are for natural Ni.

Calculated results for the ^{58}Ni(n,n') reaction to the first excited state of ^{58}Ni are shown in Fig. 38, together with the Ni total cross section in the MeV region. Calculations with the potentials of Delaroche,[67] Strohmaier,[68] and Harper,[66] all of which were developed specifically for ^{58}Ni, are included with the global potentials. As would be expected, there is a tighter envelope for the local potentials than for the global ones. There is a clear grouping of the (n,n') calculations into higher values (Becchetti, Wilmore, Rapaport, Walter, Patterson, Delaroche) and lower values (Moldauer, Engelbrecht, Kawai, Strohmaier, and Harper).

A similar grouping of the calculations into "higher" and "lower" values is seen in Fig. 39 for the (n,2n) cross sections, except that the differences are larger, reaching a factor of 2. Realizing the importance of lower energy neutron transmission coefficients in (n,2n) calculations, the qualitative correspondence of the (n,n') and (n,2n) results is understandable. The situation is less well defined for the (n,np) calculations on the right side of Fig. 39, where the results cluster somewhat tighter. The major outrider in these calculations is the result with the Becchetti potential.

The results in Figs. 38 and 39 for the local potentials, while having significantly less spread than the global potential results, are also divided into the "high" and "low" (n,n') and (n,2n) cross-section values. The experimental data are similarly divided and do not resolve this issue.

Overall, these calculations illustrate the uncertainties inherent in using unoptimized global potentials in reaction calculations. Figs. 38 and 39 indicate that the Becchetti neutron potential is not appropriate for ^{58}Ni calculations and that the Moldauer potential should not be used at higher energies, probably not above 5 MeV. In their present form the Patterson, Rapaport, and Walter potentials lead to over-predictions of the ^{58}Ni(n,2n) cross section and, less definitively, the Engelbrecht potential results in underprediction of the (n,2n) cross section. The calculated (n,2n) is more sensitive than the (n,np) cross section, as well as the (n,γ), (n,p), and (n,α) cross sections, which are not shown.

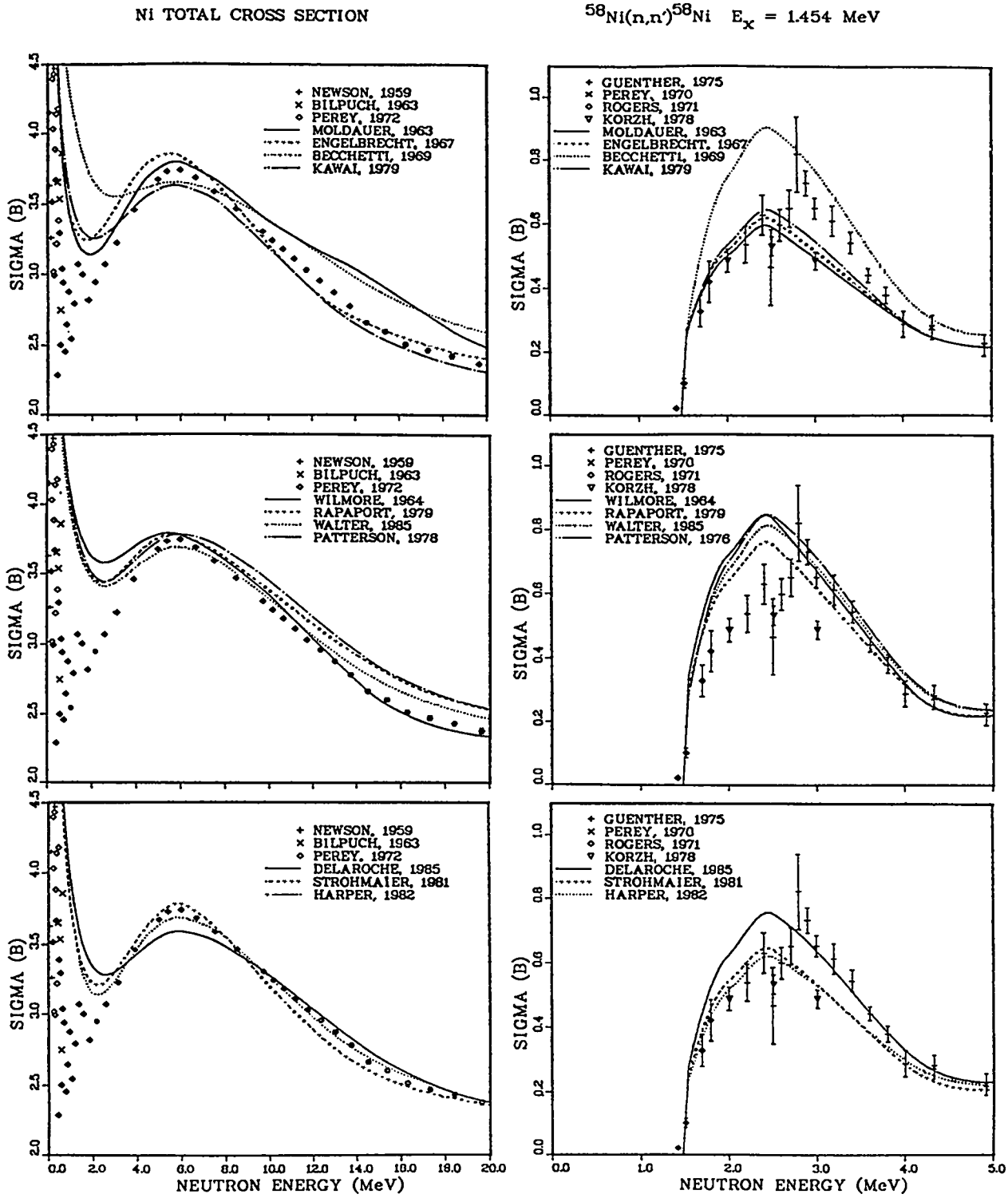

Fig. 38. Experimental total neutron and (n,n') cross sections for Ni and ^{58}Ni compared with calculations for 11 SOM potentials. See text for details of the Hauser-Feshbach statistical theory calculations.

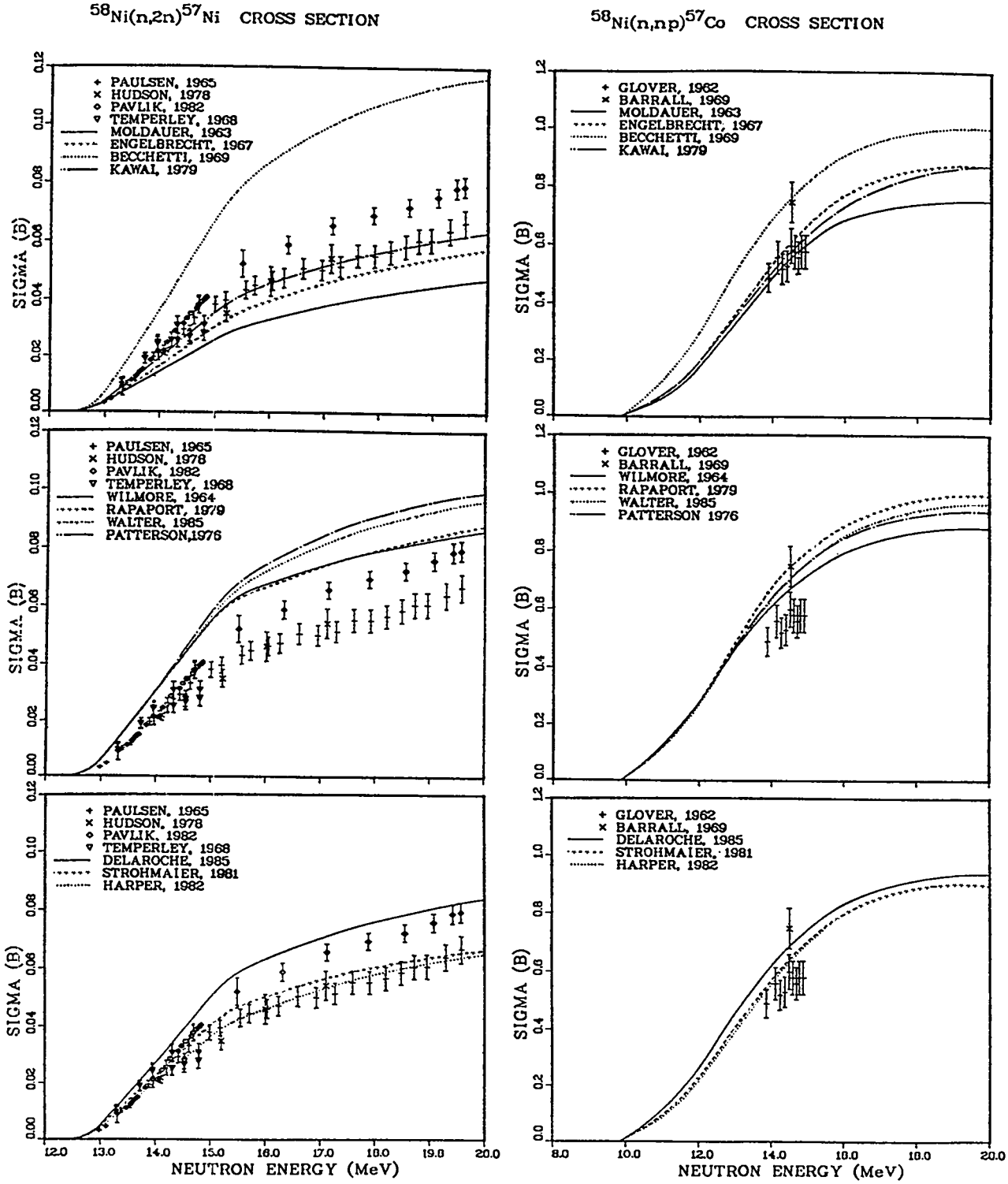

Fig. 39. Experimental (n,2n) and (n,np) cross sections for ^{58}Ni compared with Hauser-Feshbach statistical theory calculations for 11 SOM potentials.

P. Rare Earth-Actinide Potentials: ^{165}Ho, ^{238}U, ^{242}Pu (P. G. Young)

Over the past several years, a number of studies have been made of statically deformed nuclei in the rare earth and actinide regions leading to rather simple deformed optical model (DOM) parameterizations that reproduce a significant body of experimental data. Examples of some of these analyses are the Nd-Sm isotope studies by Shamu et al.[69], the W-isotope studies by Arthur[70] and Delaroche,[71] the Ho-Tm analyses by Young et al.[72], and the actinide calculations by Haouat et al.[73] and Lagrange.[74] The various potentials have many similarities, and, in some cases, the differences even in details are small. The possibility of a regional potential describing both rare earth and actinide rotational nuclei, at least at some reduced level of accuracy, is explored here, together with the suitability of global parameterizations in this region.

To investigate a regional potential, the Haouat-Lagrange actinide potential,[73,74] which describes neutron scattering results up to E_n = 5 MeV for several Th, U, and Pu isotopes, was adapted for use with ^{165}Ho. This case was chosen because a DOM parameterization already exists for ^{165}Ho[73] that is similar to ones for W isotopes[70] and ^{169}Tm,[72] as well as to the actinide potential.

The large ground state spin of ^{165}Ho ($7/2^-$) precludes the possibility of extensive standard coupled-channel calculations, and certainly any automated fitting of such calculations. To carry out the analysis, the method of deriving a DOM potential from an SOM analysis, demonstrated by Madland and Young[62] for actinides, was employed. In this instance, an abbreviated procedure was followed, because the exercise was largely exploratory and the goal was to develop a ^{165}Ho potential that was as similar as possible to the actinide potential. In particular, the following simple transformation was assumed here (using primes to denote SOM):

$$\frac{W_D a_D}{W'_D a'_D} = \frac{W_D}{W'_D} = 0.7 \quad , \tag{1}$$

and the same values of diffuseness and real well depth were used in both the SOM and DOM calculations.

Starting with an average representation of the Haouat-Lagrange potential[73,74] written in the Lane form[37] and including a small volume term, an SOM fit[58] was made to ^{165}Ho total cross-section measurements between 7 and 30 MeV and to the measured angular distribution at 11 MeV.[59] The only parameter permitted to vary in the search was W_D, assuming a linear dependence with neutron

energy. The higher energy expression that resulted for W_D was matched at 6 MeV to a lower energy segment having the same energy dependence as the actinide potential, after the appropriate scaling according to Eq. (1). The resulting parameterization is given in Table VII as "Set A."

Coupled-channel calculations were performed using the ECIS78 code[38]. Below 4 MeV, the first three members of the ground-state rotational band ($7/2^-$, $9/2^-$, $11/2^-$) were coupled in the calculations, using deformations of $\beta_2 = 0.3$ and $\beta_4 = -0.02$.[73] At higher energies, these levels were replaced by fictitious 0^+, 2^+, 4^+ levels according to the model of Lagrange et al.[75] It was determined empirically that this approximation leads to errors less than 0.8% in the total cross section for $E_n \geq 4$ MeV.

TABLE VII

NEUTRON DOM PARAMETERS FOR ^{165}Ho

			r_0 (fm)	a (fm)
Haouat et al., 1982[a73] and Lagrange, 1982[74]	$V_R = 49.8-16\eta-0.3E$		1.26	0.63
	$W_D = 5.3-8\eta+0.4E$	E≦10 MeV	1.26	0.52
	$W_D = 9.3-8\eta$	E>10 MeV		
	$V_{SO} = 6.2$		1.12	0.47
Set A	Same as Haouat except:			
	$W_D = 4.7-8\eta+0.4E$	E≦6 MeV	1.26	0.52
	$W_D = 7.1-8\eta-0.046(E-6)$	E>6 MeV		
	$W_V = -1.8+0.2E$		1.26	0.63
Set B	Same as Haouat except:			
	$W_D = 5.0-8\eta+0.4E$	E≦8 MeV	1.26	0.52
	$W_D = 8.2-8\eta-0.046(E-8)$	E>8 MeV		
	$W_V = -1.8+0.2E$		1.26	0.63

[a]Averaged over several actinides.

Calculations of the ^{165}Ho total cross section and elastic angular distribution at 11 MeV with the DOM version of Set A are compared with measurements and with calculations using the Young et al.[72] DOM parameterization in Figs. 40 and 41, respectively. (The SOM calculations of both the total cross section and elastic angular distributions show the characteristic overprediction of maxima and underprediction of minima.) The results from the Set A DOM agree with the measurements about as well as the Young results, except for a 2-3% overprediction of the total cross section near 14 MeV. The agreement with the elastic angular distribution at 14 MeV is improved over that of Young et al.

The final iteration in this simple procedure was to roughly average the W_D parameterization for ^{165}Ho with that from the actinide potential; the result is the average potential Set B in Table VII. Calculations with the Set B parameterization, also included in Figs. 40 and 41, generally improved agreement with the total cross-section data, but slightly worsened agreement with the 11-MeV angular distribution measurement.

Calculations of ^{238}U and ^{242}Pu neutron total cross sections with the Set B DOM parameterization are compared in Figs. 42 and 43 with measurements[59] of neutron total cross sections and with the regional DOM parameterizations of Haouat-Lagrange[73,74] and Madland.[62] Values of β_2 and β_4 from the Haouat-Lagrange analysis were used in the calculations with Set B. Agreement with the data is slightly poorer at low energies with Set B as compared with the Haouat-Lagrange actinide potential. At energies above 2 MeV, however, Set B reproduces the σ_T data as well as or better than the Haouat-Lagrange potential. The Madland DOM potential appears to best reproduce the total cross-section data for both ^{238}U and ^{242}Pu up to 10 MeV, which is the limit of its range of validity.

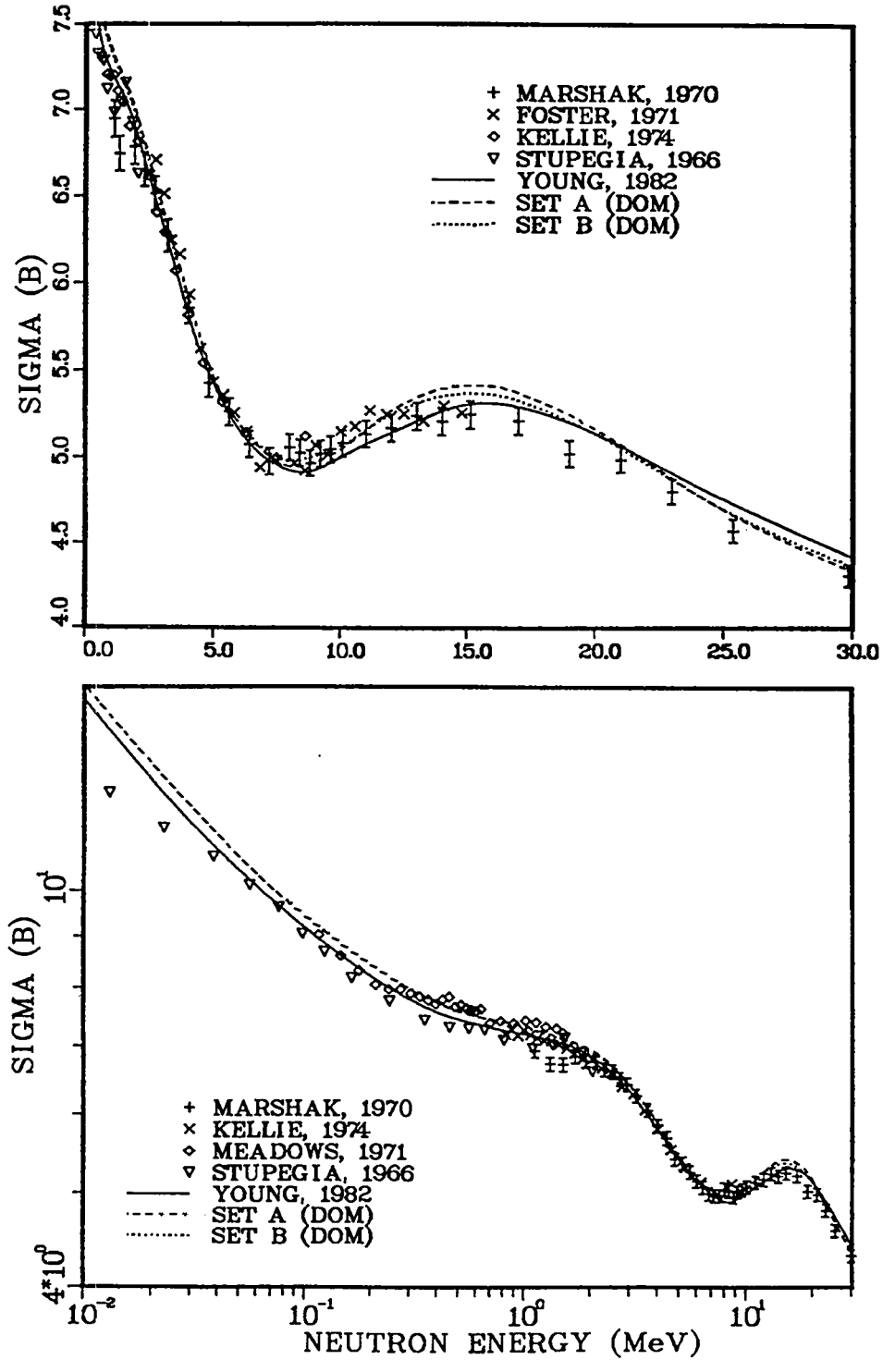

Fig. 40. Comparison of calculations with several deformed optical potentials for measurements of σ_T vs E_n for ^{165}Ho. The Set A and Set B potentials are described in the text and in Table VII.

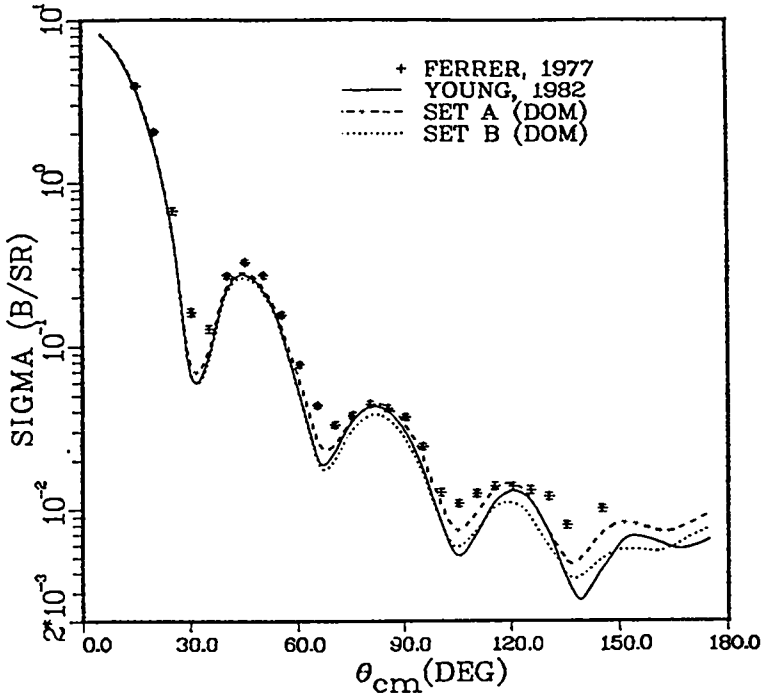

Fig. 41. Comparison of calculations with several deformed optical potentials for measurements of $\sigma_{Elastic}(\theta)$ vs θ for 11 MeV neutrons for ^{165}Ho. The Set A and Set B potentials are described in the text and in Table VII.

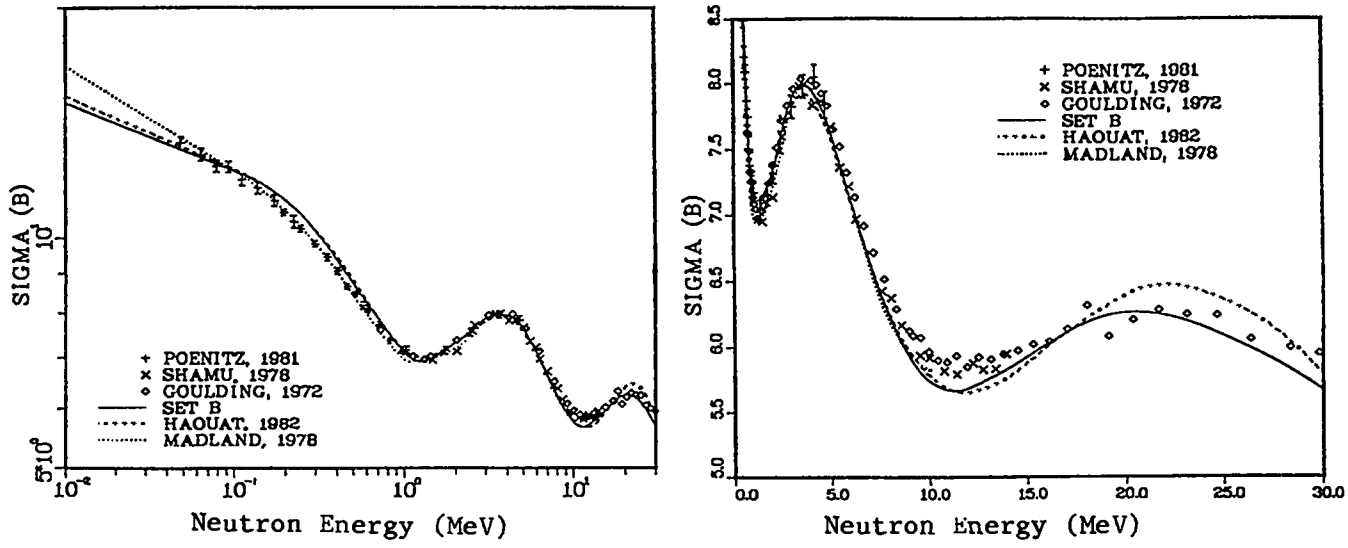

Fig. 42. Comparison of experimental neutron total cross sections for ^{238}U with calculated values from 3 deformed optical potentials. The Set B parameterization is described in the text and in Table VII.

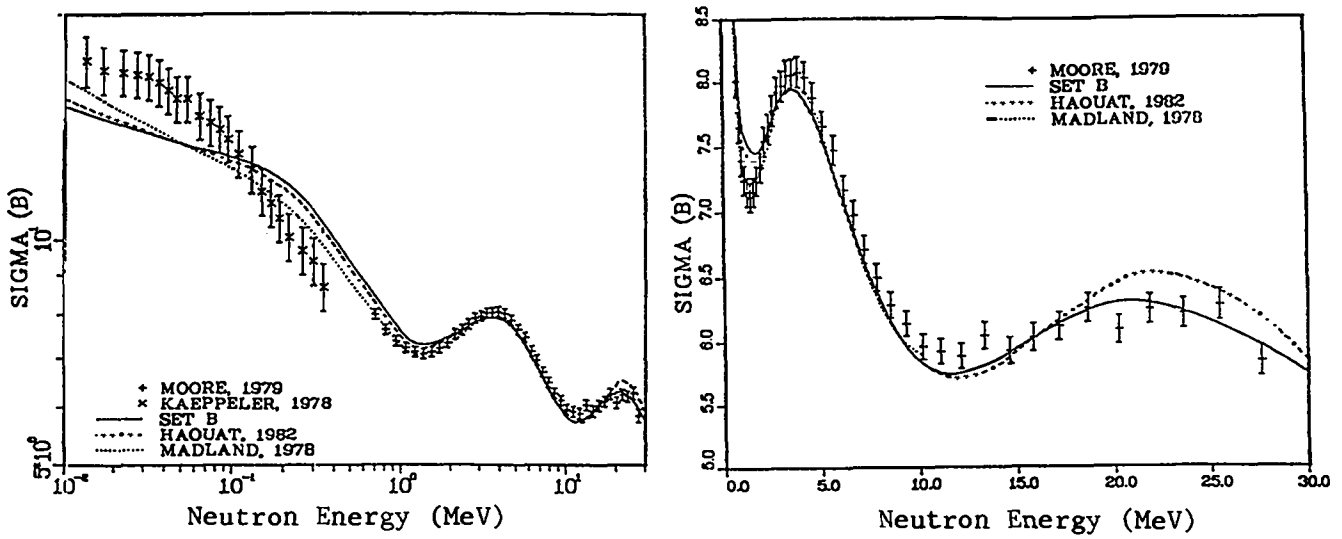

Fig. 43. Comparison of experimental neutron total cross sections for ^{242}Pu with calculated values from 3 deformed optical potentials. The Set B parameterization is described in the text and in Table VII.

Q. Reaction Theory Calculations of n + ^{165}Ho Reactions (P. G. Young)

Preliminary calculations have been performed of neutron-induced reactions on ^{165}Ho using the COMNUC[63] and GNASH[8] code systems. The following assumptions were made for the calculations:

1. Neutron transmission coefficients from deformed optical model calculations are used.

2. Experimental energy levels, spins and parities up to 482 keV in ^{166}Ho (22 levels) and 590 keV in ^{165}Ho (14 levels) are included.

3. A Gilbert-Cameron[64] level-density formulation, which reproduces observed level spacings at the neutron binding energy, is matched (number and energy derivative) to the experimental levels in (2) above.

4. Width-fluctuation corrections are included in the cross section calculations below 0.5 MeV but are negligible at higher energies.

5. Gamma-ray transmission coefficients are inferred from a Tm measurement. In particular, the shape of a γ-ray strength function was determined from a measurement[76] on ^{169}Tm and the normalization was accomplished from measurements of $\langle\Gamma_{\gamma 0}\rangle$ and $\langle D_0\rangle$ for ^{165}Ho, as compiled by Mughabghab,[57] in the following manner:

   a. A giant-dipole-resonance shape and normalization was taken for $f_{M1}(E_\gamma)$ from the systematics of Lone.[77]

b. The assumed $f_{M1}(E_\gamma)$ was subtracted from the measured[78] total $f(E_\gamma)$ for Tm, resulting in a tabulation for the dominant $f_{E1}(E_\gamma)$ strength function.

c. Weisskopf single-particle estimates were used to obtain E2, M2, E3, M3, E4, and M4 strength functions.

d. The normalization of the resulting total gamma-ray strength function was determined from $\langle\Gamma_{\gamma 0}\rangle$ and $\langle D_0\rangle$ measurements on ^{166}Ho from the expression

$$\left.\frac{\langle\Gamma_\gamma\rangle}{\langle D\rangle}\right|_{\ell=0} = \int_0^{B_n} \left(\sum_{x\ell} f_{x\ell}(E_\gamma) E_\ell^{2\ell+1}\right) \rho(B_n - E_\gamma) dE_\gamma \quad ,$$

where B_n is the neutron binding energy of ^{166}Ho.

The neutron total cross sections that result from the deformed optical model analyses of Young et al.[72] are compared with the "Set A" analysis and experimental data in Sec. P. The agreement with experiment is better than ± 5% for both potentials from 10 keV to 30 MeV, and somewhat closer at most energies.

The ^{165}Ho(n,γ) radiative capture cross section calculated with Young et al. potential[72] is compared with experimental data[59] for neutron energies between 1 keV and 4 MeV in Fig. 44. Here the agreement is generally within ± 20%, depending upon the particular measurements in the comparison.

Calculations of the ^{165}Ho(n,2n) cross section to the 6^- isomeric state of ^{164}Ho at E_x = 140 keV with the Young et al. potential and both the Set A and Set B potentials of Sec. P are compared with experimental data in Fig. 45. The difference in the calculations for the three potentials is less than 10% at all energies.

To test the theoretical gamma-ray emission spectra from the models, the shape of a spectrum for thermal incident neutrons calculated with the Young et al. potential is compared with the measurement of Orphan et al.[78] in Fig. 46. The experimental spectrum, given by the dashed histogram was obtained by unfolding spectral data from a Ge(Li) detector. The unfolding uncertainties and sharp decrease in efficiency of the pair spectrometer that was used precluded determination of the unresolved spectrum below 1.5 MeV (although lines were measured down to E_γ = 220 keV). The agreement between the calculated and measured spectrum above E_γ = 1.5 MeV is not too unreasonable, but some significant differences do appear.

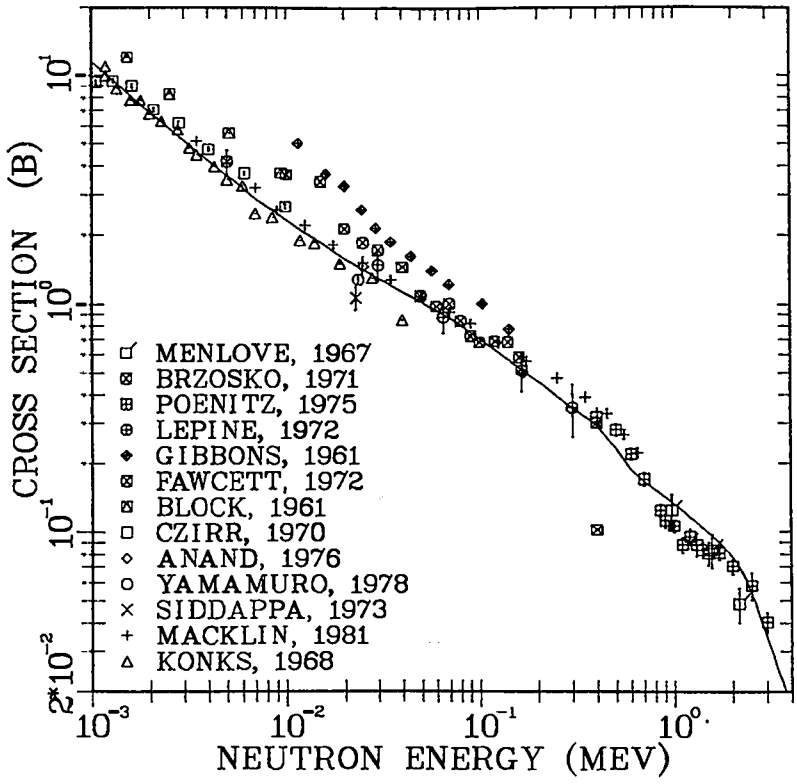

Fig. 44. Comparison of the calculated ^{163}Ho(n,γ) cross section (Young et al.[72] potential) with experimental data between 1 keV and 4 MeV.

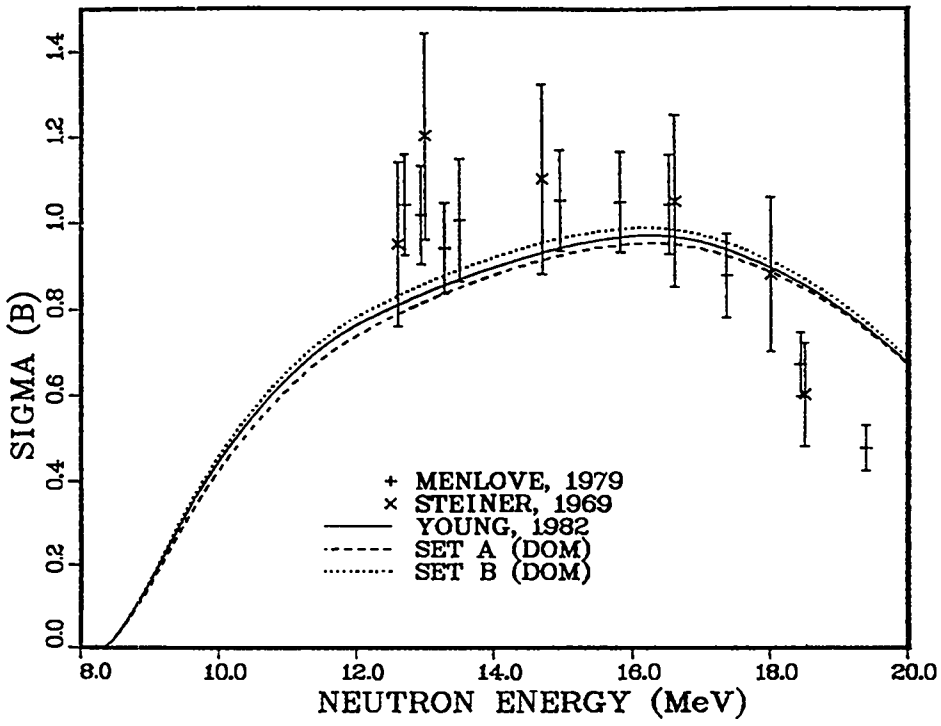

Fig. 45. Comparison of calculations with several deformed optical potentials for measurements of $\sigma_{n,2n}$ (metastable) vs E_n for ^{165}Ho. The Set A and Set B potentials are described in the text and in Table VII.

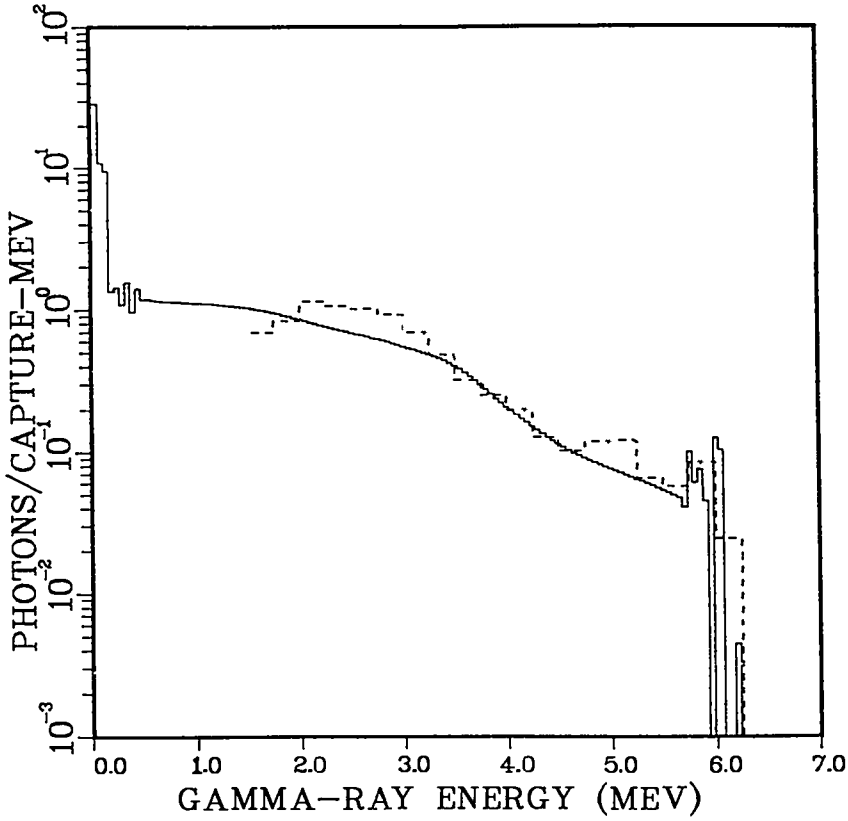

Fig. 46. Photon-emission spectra from ^{165}Ho(n,γ) reactions with thermal neutrons. The solid curve was calculated using the Young et al.[72] potential; the dashed histogram represents the measurement of Orphan et al.[78]

Finally, Fig. 47 gives the γ-ray spectrum calculated at E_n = 50 keV, now represented in absolute units of b/MeV. The shape is very similar to the one calculated at thermal except some of the weaker lines are starting to become more significant.

The comparisons presented above indicate that these preliminary calculations agree quite reasonably with the available experimental data. Further optimization of the gamma-ray strength functions might be attempted after new gamma-ray measurements are completed* at Los Alamos.

*Information available from S. Wender (P-3) and G. Auchampaugh (P-DO) of the Los Alamos National Laboratory.

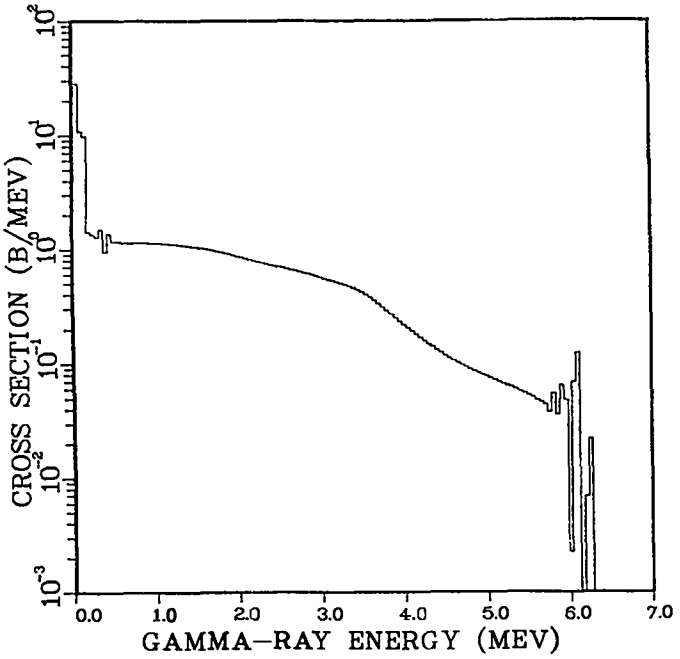

Fig. 47. Calculated gamma-ray emission spectrum for ^{165}Ho (n,xγ) reactions with 50-keV neutrons.

R. GNASH Output Conversion Code for ENDF/B File 6: GNFILE6 (P. G. Young)

A program (GNFILE6) has been developed that converts output from the GNASH[8] Hauser-Feshbach statistical theory code to an energy-angle correlated representation in ENDF/B-VI File 6 format. Because GNASH only calculates angle-independent spectra, the code utilizes the File 6 LAW=1, LANG=2 option, which specifies that Kalbach-Mann systematics[79] are used to represent the angular dependence of the energy-angle emission spectra. Accordingly, the GNFILE6 code collects the outgoing particle spectra, $d\sigma/d\varepsilon_i$, and determines preequilibrium fractions, $P(\varepsilon_i)$, for each outgoing particle (i) at each bombarding energy included in the GNASH calculations, and outputs them in the appropriate File 6 format. Also included in the output are $d\sigma/d\varepsilon$ File 6 tables for outgoing gamma rays, which are assumed to be isotropic.

The code presently handles neutrons, protons, deuterons, and alphas as incident or outgoing particles. Interpolation schemes for the emission spectra may be specified as histograms, linear $(d\sigma/d\varepsilon)$-linear (ε), or log $(d\sigma/d\varepsilon)$-linear (ε). The emission spectra are automatically thinned in outgoing energy according to an inputted criterion. Provision is made to remove a variable (inputted) number of discrete inelastic lines from the File 6 spectra in order to represent the lines more precisely in ENDF/B Files 3 and 4. In addition, the code scans the discrete gamma rays from the calculation, and automatically places all of those having cross sections greater than an inputted minimum value into the File 6 discrete-line representation.

The code has been utilized to construct ENDF/B file 6 tables from the neutron- and proton-induced GNASH calculations on ^{27}Al, described in Sec. F.

S. Modeling Levels of Odd-Mass Deformed Nuclei (D. G. Madland)

A computer code NUCLEV has been developed to complete the low-excitation rotational band structure of odd-mass deformed nuclei, given that some members of each band are experimentally determined in excitation energy, spin, and parity. Axial symmetry is assumed. Then, the relevant equation from the particle-rotor is given by

$$E(J,K) = \varepsilon_K + \frac{\hbar^2}{2I}\left[J(J+1) - K^2 + \delta_{K,\frac{1}{2}}\, a(-1)^{J+\frac{1}{2}}\left(J+\frac{1}{2}\right)\right] \qquad (2)$$

where ε_K is the single-particle (quasi-particle) energy, I is the moment of inertia, J is the total angular momentum, K its projection on the body-fixed symmetry axis, and a is the decoupling parameter. The last term in Eq. (2), in which a appears, arises from the Coriolis interactions. It has been assumed that the so-called recoil term[80] can be absorbed into the quasi-particle energy. Finally, band mixing effects have, so far, been ignored.

The solution of Eq. (2) then requires knowledge of three states to determine the three unknowns (ε_K,I,a) for $K = \frac{1}{2}$ and knowledge of two states to determine the two unknowns (ε_K,I) for $K > \frac{1}{2}$. If insufficient experimental information exists (the usual case), one can use Nilsson or Nilsson-like calculations to complete, as much as possible, the low-lying level spectrum. It is noted here that usually the first few members of a given low-lying band are the most accurately known experimentally. In such cases the best possible values are obtained for ε_K, I, and a (if $K = \frac{1}{2}$) provided, of course, that one does not then attempt to calculate band members too high in spin values where $I = I(\omega)$. Another reason to confine the calculation of the discrete level spectrum to lower excitation energies is that more complex states than those treated here arise as the excitation energy increases. For these reasons, the maximum excitation energy is confined in the present calculations to values between 1 and 2 MeV for the rare earths, actinide, and transactinide nuclei.

For a specified value of the maximum excitation energy EEMAX, the code NUCLEV calculates the remaining members of each band up to excitation EEMAX. It then produces a discrete level spectrum by ordering all levels in increasing excitation energy, computes the angular momentum distribution together with

first and second moments, the parity distribution, and the cumulative energy distribution (discrete nuclear level density). Finally, if desired, a search is performed for adjacent levels that are within some specified energy interval, to aid in searches for close-lying pairs.

As a test example, calculations have been performed for seven nuclei, with EEMAX = 1 MeV, that have been well studied experimentally. The results are summarized in the last column of Table VIII, which gives RMS deviations between calculated and measured sets of levels. In computing the RMS, none of the measured levels used to determine the parameters of Eq. (2) were included. The range of RMS deviations extends from 2.5 keV (^{239}Pu) to 19.9 keV (^{171}Yb). The RMS deviation is, of course, influenced by how well the level is measured and by how appropriate the model is. In some of the cases of Table VIII, the magnitude of the RMS deviation is dominated by contributions from one or two states. On the basis of this test example, one would conclude that RMS deviations of perhaps a few keV can be achieved.

TABLE VIII

COMPARISONS WITH EXPERIMENTAL LEVELS FOR EXCITATION ENERGIES BELOW 1 MeV

Nucleus	Number of Known Bands[a]	Number of Known Band States[a]	Number of Calculated Band States	Number of Known Band States Needed for Parameters	Number of Band States That Can Be Compared	RMS Deviation[b] (keV)
$^{167}_{68}$Er	9	41	46	20	21	10.6
$^{171}_{70}$Yb	9	35	41	19	16	19.9
$^{179}_{72}$Hf	7	25	34	15	10	6.5
$^{183}_{74}$W	7	20	31	15	5	4.8
$^{237}_{92}$U	8	28	56	17	11	8.3
$^{237}_{93}$Np	6	35	55	14	21	5.4
$^{239}_{94}$Pu	5	25	46	12	13	2.5

[a]Taken from Ref. 81.

[b]Not including the known band states used to determine the parameters for calculating the members of each band.

T. Nuclear Structure Studies for Gamma-Ray Lasers [D. G. Madland, E. D. Arthur, D. C. George, and D. Strottman (T-9)]

We summarize some initial results in our investigation of the nuclear physics issues of gamma-ray lasers. We describe here what is known thus far from existing experimental data and which theoretical models one may employ for systematic searches of candidate nuclei and for detailed calculation of candidate level properties. We have earlier reported[82] on simple nuclear physics considerations that indicate which mass regions may be most fruitful to search. A detailed summary of all of our initial results is given in Ref. 83.

Some of the proposed schemes for gamma-ray lasers require the identification of a suitable nucleus in which an isomeric state (of sufficient lifetime to allow population and preparation in a host material) lies nearby a state that decays essentially instantaneously. Because of present-day limitations on radiation sources needed to drive the interlevel transition to produce lasing, the energy spacing between the two states must be less than several hundred electron volts (eV).

As part of an effort to identify possible nuclei with certain of the above level characteristics, we completed a search of the computerized nuclear structure data library, CDRL82,[84] which is based on the 1978 Table of Isotopes[85] compilation. This library contains data (excitation energy, spin, parity) for 41000 levels although, because of the vintage of the compilation (1977), current data are often lacking.

The criterion used to perform the search was initial identification of isomeric states having lifetimes greater than or equal to a specified input value. A halflife $\geq$ 5 seconds was used for these results. After identification of such a state, the spacings of nearby levels were examined to determine which ones (if any) fell within a specified excitation energy window, ΔE. (Two ΔE values were specified: 5 keV and 1 keV.) If one or more levels were found that lay nearby to an isomeric state of sufficient lifetime, then the energy, spin, and parity information appropriate to such levels was printed. These results were examined further to eliminate levels where spin or parity information was lacking, or where an obvious level duplication had occurred.

Figure 48 illustrates regions of the periodic table where candidate nuclei having isomeric states of lifetime > 5 s along with short-lived levels occurring within a spacing of 5 keV are indicated. Also shown (approximately) by the shaded areas are regions of nuclear deformation where enhanced densities of

nuclear levels should occur. Table IX lists the nuclei identified in this search. For the next part of the search, the spacing criterion was lowered to ≦ 1 keV. Figure 49 depicts the candidate nuclei identified. Of the nuclei appearing in Fig. 49, ^{179}Hf is of particular interest because it exhibits the closest level spacing (~ 200 eV) of any nucleus identified. The transition from the short-lived nuclear state involves a 1.1 MeV gamma ray, which may be too energetic for the gamma-ray laser, but ideal for investigation of interlevel transfer processes.

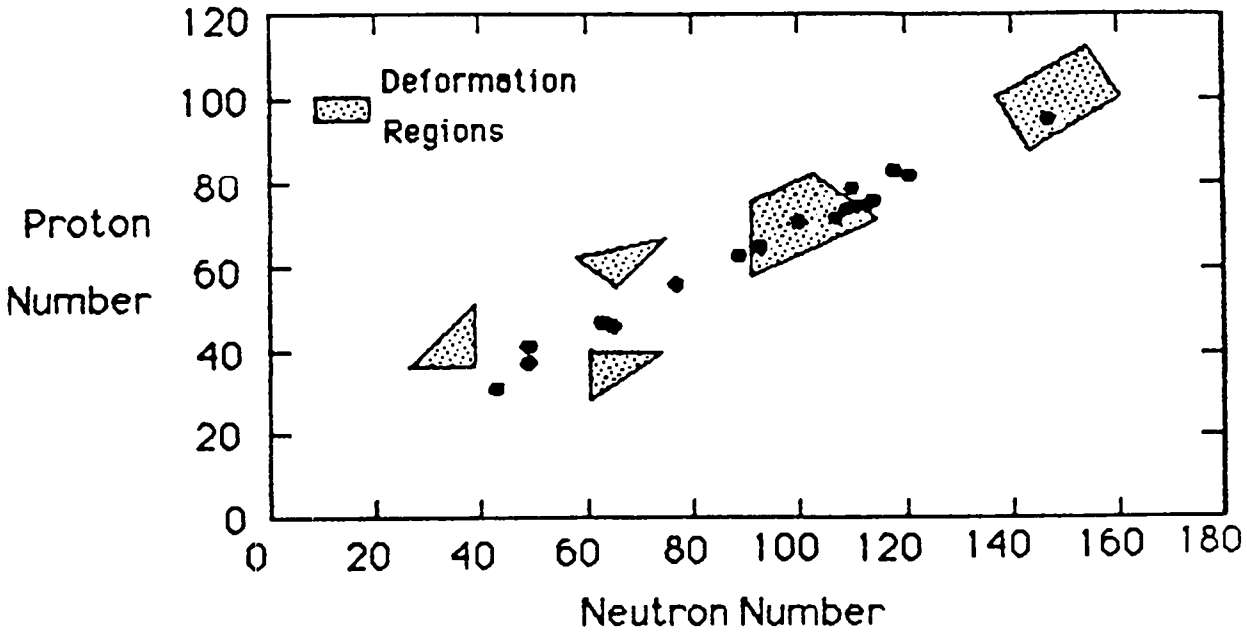

Figure 48. Candidate nuclides with 5 keV (or less) spacings.

TABLE IX

NUCLEI IDENTIFIED IN THE SEARCH WITH $\Delta E \leqq 5$ keV

$_{31}Ga^{74}$	$_{37}Rb^{80}$
$_{41}Nb^{90}$	$_{46}Pd^{111}$
$_{47}Ag^{110}$	$_{56}Ba^{133}$
$_{63}Eu^{152}$	$_{65}Tb^{158}$
$_{71}Lu^{171}$	$_{72}Hf^{179}$
$_{74}W^{183}$	$_{82}Pb^{203}$
$_{83}Bi^{201}$	$_{95}Am^{242}$

There are several difficulties associated with this search, most of which are related to the vintage (1977) of the compilation. Experimental techniques have progressed significantly over the past 8 years so that a more up-to-date compilation might offer many more nuclear candidates. Secondly, two data files, one resulting from nuclear decay data and the other from reaction data, were merged to produce CDRL82. In the process, levels appearing in these separate files having spacings ≦ 1 keV were considered to be the same. While this presumption is prudent for most nuclear levels, there is a significant chance that level information applicable to the gamma-ray laser could be lost. In order to circumvent certain of these problems (especially those related to use of antiquated data), a second search has begun using nuclear structure data from the more recent (circa 1982 for some nuclei) ENSDF[85] evaluated nuclear structure file.

As a second step in the effort to determine which mass regions may be most fruitful to search theoretically, and to check our earlier conclusions[83] based upon simple theoretical arguments, we have scanned both the CDRL and ENSDF

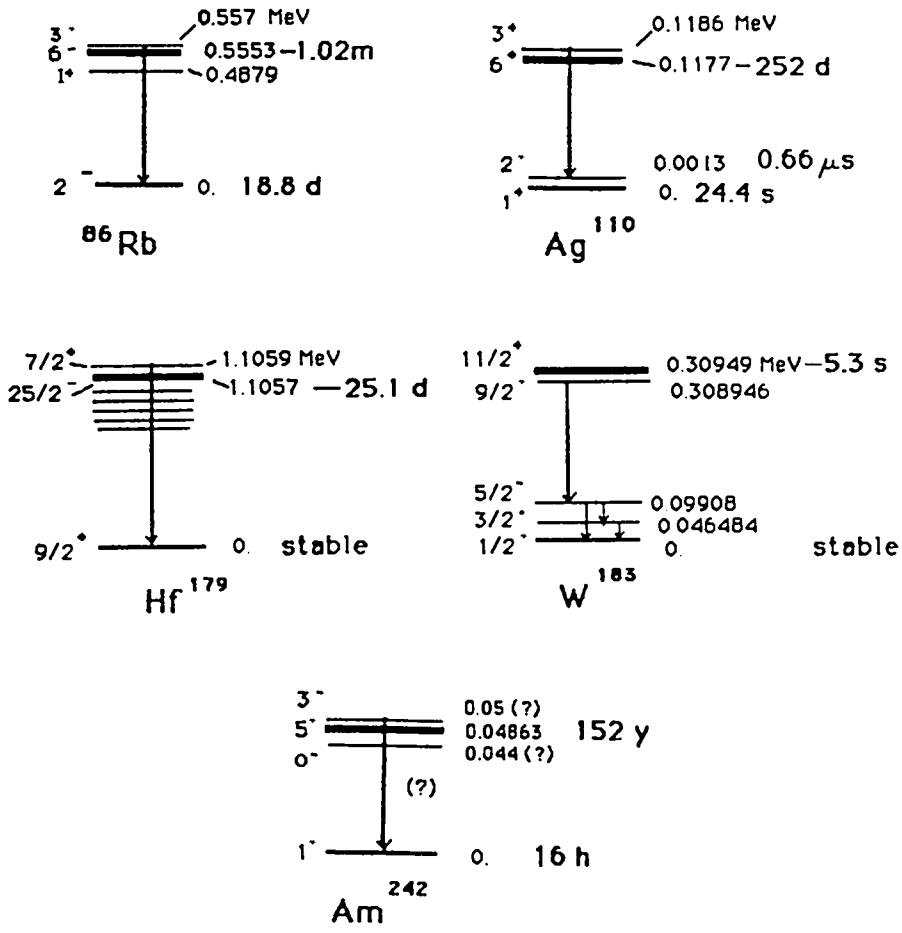

Fig. 49. Candidates having spacings ≦ 1 keV.

nuclear structure files for experimentally known isomeric states. We have performed four scans, on each file, for isomeric state halflives, $T_{\frac{1}{2}}$, that are greater than 1 s, 1 min, 10 min, and 1 h. For each of these ranges we have calculated the average number of isomeric states as a function of the nuclear mass number A. Figures 50 and 51 illustrate the results for the range $T_{\frac{1}{2}} > 10$ min for the CDRL and ENSDF files, respectively. These clearly show strong dependencies of the average number of isomeric states on mass number. As we expected,[82,83] regions of shell closure in neutron number N and proton number Z, as well as deformed rare earth and actinide nuclei, contain the largest numbers of isomeric states. In particular, the regions N = (28,50,82), Z = (28,50), the rare earths ($150 \leq A \leq 190$), and the actinides and transactinides (A > 220), exhibit well-defined peaks. However, the largest peak (for each of the four halflife ranges studied) occurs for mass numbers A = 195-197, which corresponds to stable and long-lived isotopes of $_{76}$Os, $_{77}$Ir, $_{78}$Pt, $_{79}$Au, and $_{80}$Hg. These nuclei are representative of the transition region between the heavy deformed rare earths and the spherical nuclei near doubly magic ^{208}Pb. Clearly, this region could be further investigated for possible gamma-ray laser considerations.

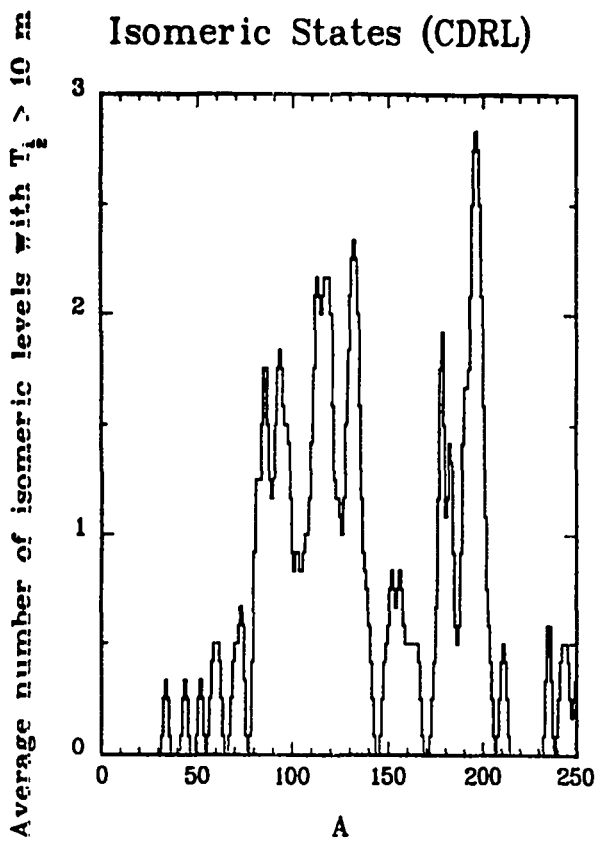

Fig. 50. Average number of isomeric levels with halflives greater than 10 min as a function of nuclear mass number. The CDRL 1982 evaluated nuclear structure file[84] was used.

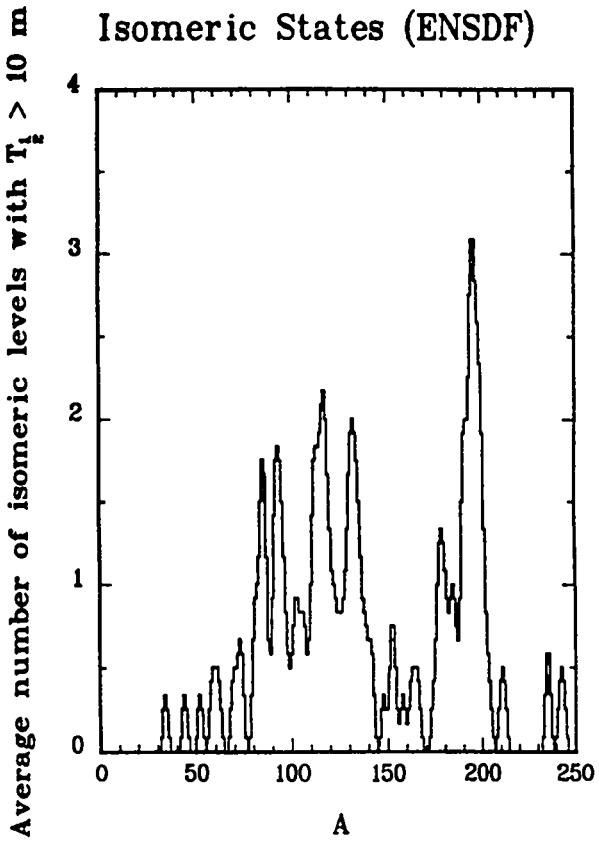

Fig. 51. Identical to Fig. 50 except that the ENSDF evaluated nuclear structure file[86] was used.

We now briefly describe the main theoretical models we envision using to systematically search for candidate nuclei and to determine candidate level properties.

Odd-A Nuclei. Most descriptions of odd-A nuclei begin with the Bohr-Mottelson ansatz for the Hamiltonian:

$$H = \sum_k \frac{\hbar^2}{2I_k} (J_k - j_k)^2 = \sum_k \frac{\hbar^2}{2I_k} R_k^2 \ , \qquad (3)$$

where the I_k are moments of inertia, and J_k, R_k, and j_k are components of the total, core, and single-particle angular momentum, respectively. In particular, referring to the 3-axis of the body-fixed systems, $J_3 = K$ and $j_3 = \Omega$, whereas, referring to the space-fixed system, $J_{3'} = M$. The corresponding wave function under the assumption of axial symmetry ($I_1 = I_2 = I$) is

$$\Phi^J_{MK} = \sqrt{\frac{2J+1}{16\pi^2}} \left[D^J_{MK} \chi_K + (-1)^{J-K} D^J_{M-K} \chi_{-K} \right] \ , \qquad (4)$$

$$\text{with} \quad \chi_K = \sum_j a_{jK} \phi_{jK} \ , \qquad \text{where} \qquad (5)$$

ϕ_{jK} are the single-particle wave functions and the a_{jK} are given by the Nilsson model or similar calculation. For an axially-asymmetric system, the wave function (4) must be summed over K.

With axial symmetry, the matrix element of H can be readily calculated using Eq. (4):

$$\langle JK|H|JK\rangle = \frac{\hbar^2}{2I}\left[J(J+I) - K^2 + \langle JK|\vec{j}^{\,2} - K^2|JK\rangle - \delta_{K,\frac{1}{2}}(-1)^{J+\frac{1}{2}}(J+\frac{1}{2})a\right] . \quad (6)$$

The third term is referred to as the recoil term, while the last term arises from the Coriolis interactions, connecting K and -K in a cross matrix element, and is therefore nonzero only if $K = \frac{1}{2}$. The quantity a, the decoupling parameter, is given by

$$a = \sum_j (-1)^{j-\frac{1}{2}}(j+\frac{1}{2})(a_{j\frac{1}{2}})^2 \quad , \quad (7)$$

where the $a_{j\frac{1}{2}}$ are expansion coefficients of a Nilsson wave function.

In practice the recoil term is usually ignored by assuming that its effects can be lumped into the single particle energy. However, in our application where the accurate determination of the candidate level energy is crucial, this term cannot be ignored. It is especially important if several valence nucleons exist, because the recoil term then contains one-body and two-body operators and cannot be absorbed into the single-particle potential. Moreover, when pairing is taken into account, even if there is only a single valence nucleon, the recoil term becomes effectively a many-body operator.

A second refinement leading to more accurate prediction of candidate level energy is the inclusion of band mixing effects due to off-diagonal matrix elements arising from the Coriolis interactions, $\langle JK'|H|JK\rangle$. These matrix elements exist when K′ and K differ by 1 and they may alter the energy dependence from that of Eq. (4). It is stressed here that the magnitude of such off-diagonal matrix elements is not yet completely understood. More theoretical work is therefore required in this area.

Odd-Odd Nuclei. In the simplest generalization of Eq. (3), to include two extra nucleons, one has

$$H = \sum_k \frac{\hbar^2}{2I_k}(J_k - j_k^n - j_k^p)^2 + V_{np} \quad , \quad (8)$$

where V_{np} is the residual neutron-proton interaction. Only the axially-symmetric case has been worked out in detail, due to uncertainties in V_{np} and odd-odd experimental level schemes. In this case, $K = \Omega_n + \Omega_p$ and the only term that is new is V_{np}. The matrix element for V_{np} is then given by

$$\langle JK|V_{np}|JK'\rangle = \langle\Omega_p\Omega_n|V_{np}|\Omega'_p\Omega'_n\rangle + (-1)^{K+J}\delta_{K-K'}\ \langle\Omega_p\Omega_n|V_{np}|-\Omega'_p - \Omega'_n\rangle \quad . \qquad (9)$$

The first term is called the Gallagher-Moszkowski[87] matrix element and the second the Newby[87] matrix element. The Newby matrix element contributes only to $K = 0$ bands owing to the rotational invariance of V_{np}. The magnitudes of these matrix elements are, typically, 100 keV and 50 keV, respectively. Clearly, an accurate calculation of the energy of a candidate level in an odd-odd nucleus requires a very good representation of V_{np}. In addition, odd-odd axially-asymmetric nuclei of interest, perhaps near $A \sim 180$, no longer have $K = \Omega$. This means that the entire formalism summarized above must be repeated to obtain the analogous, although more complex, expressions for the level energies of such nuclei. We note here that the largest peaks of Figs. 50 and 51, those corresponding to $A \sim 194$-198, may include such nuclei. Given this possibility, the axial-asymmetric model may be very important in the search for candidate levels for the gamma-ray laser.

U. Comparisons of Four Representations of the Prompt Neutron Spectrum for the Spontaneous Fission of ^{252}Cf [D. G. Madland, R. J. LaBauve, and J. R. Nix (T-9)]

Because of its importance as a neutron standard, we present comparisons of measurements and calculations of the prompt fission neutron spectrum N(E) for the spontaneous fission of ^{252}Cf. In particular, we test four representations of N(E) against recent experimental measurements of the differential spectrum and threshold integral cross sections. These representations are the Maxwellian spectrum, two versions of the Watt spectrum, the NBS spectrum,[88] and the Los Alamos spectrum of Madland and Nix.[89] For the Maxwellian spectrum, we obtain the value of the Maxwellian temperature T_M by least-squares adjustments to the experimental differential spectrum of Poenitz and Tamura[90] and also that of Boldeman et al.[91] Similarly, for the Watt spectrum we perform least-squares adjustments to obtain the Watt temperature T_W with the other parameter of the Watt spectrum, the average kinetic energy per nucleon E_f, determined from experiment. For the Los Alamos spectrum, least-squares adjustments determine the nuclear level-density parameter a, which is the single unknown parameter that

appears. The NBS spectrum has been previously constructed by adjustments to eight earlier differential spectrum measurements. With these representations of the spectrum so determined, we calculate 15 threshold integral cross sections for each representation, using ENDF/B-V cross sections generally, and compare the calculated values with the measured values of Grundl et al.[92] and Kobayshi et al.[93]

We consider first the differential spectrum of Poenitz and Tamura. Our least-squares adjustments with respect to this experiment give the following adjusted parameter values and minimum values of χ^2 per degree of freedom: Maxwellian (T_M = 1.429 MeV, χ^2 = 1.20), Watt (T_W = 0.897 MeV, χ^2 = 2.33), modified Watt (T_W = 0.897 MeV, χ^2 = 1.57), and Los Alamos (a = A/9.15 MeV^{-1}, χ^2 = 0.55). Here the modified Watt spectrum is the average of two Watt spectra representing separately neutron emission from equi-temperature fragments of the light and heavy fragment mass peaks. The values of E_f^L and E_f^H are again determined from experiment. The NBS spectrum yields a value of χ^2 = 1.92. The ratios of these spectra and the experimental spectrum to the Maxwellian spectrum are shown in Fig. 52. Clearly, the Los Alamos spectrum agrees best with the experiment, both in overall shape agreement and by factors exceeding two in χ^2.

Secondly, we consider the differential spectrum of Boldeman et al. Our least-squares adjustments with respect to this experiment give the following corresponding values: Maxwellian (T_M = 1.420 MeV, χ^2 = 8.24), Watt (T_W = 0.926 MeV, χ^2 = 31.70), modified Watt (T_W = 0.922 MeV, χ^2 = 23.42), and Los Alamos (a = A/9.50 MeV^{-1}, χ^2 = 11.59). The NBS spectrum yields a value of χ^2 = 6.09. The ratios of these spectra and the experimental spectrum to the Maxwellian spectrum are shown in Fig. 53. Here the NBS spectrum agrees best with the experiment in terms of χ^2. However, the Maxwellian and Los Alamos spectra yield χ^2 values that are within a factor of two of the minimum value.

Figure 54 shows 15 ratios of calculated to experimental integral cross sections, as a function of the effective threshold energy of the reaction, for each of the spectra that have been adjusted with respect to the Poenitz and Tamura measurement, plus the NBS spectrum. We infer that the Maxwellian spectrum is too hard in the tail region and that the two Watt spectra are too soft. The NBS spectrum is slightly hard and the Los Alamos spectrum is slightly soft. The corresponding ratios for spectra adjusted with respect to the Boldeman et al. experiment, plus the NBS spectrum, are shown in Fig. 55. Similar inferences are made here except that the Los Alamos spectrum is just slightly hard and it gives the best overall agreement with experiment.

This work has been presented[94] at the International Conference on Nuclear Data for Basic and Applied Science, May 13-17, 1985, Santa Fe, New Mexico.

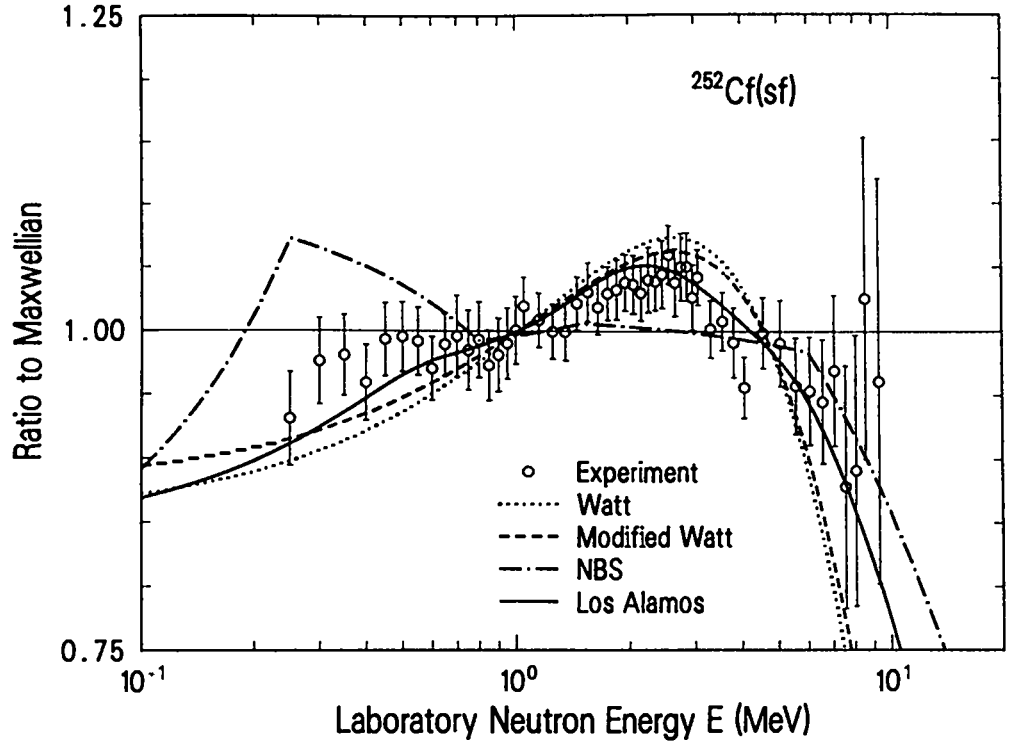

Fig. 52. Differential spectrum comparisons for adjustments to the Poenitz and Tamura experiment (Ref. 89).

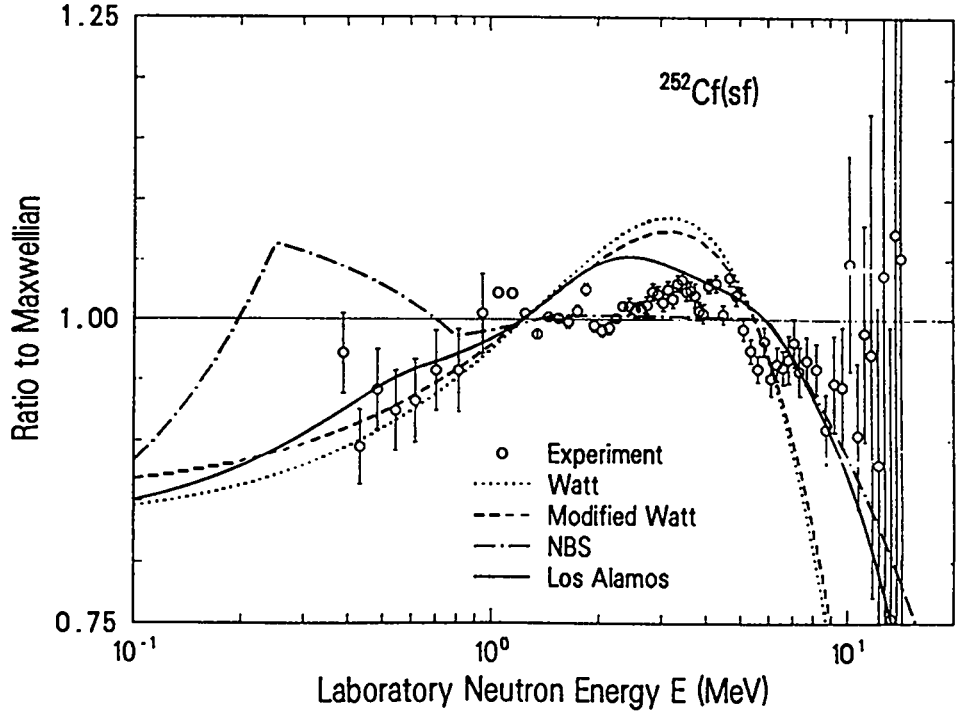

Fig. 53. Differential spectrum comparisons for adjustments to the Boldeman et al. experiment (Ref. 91).

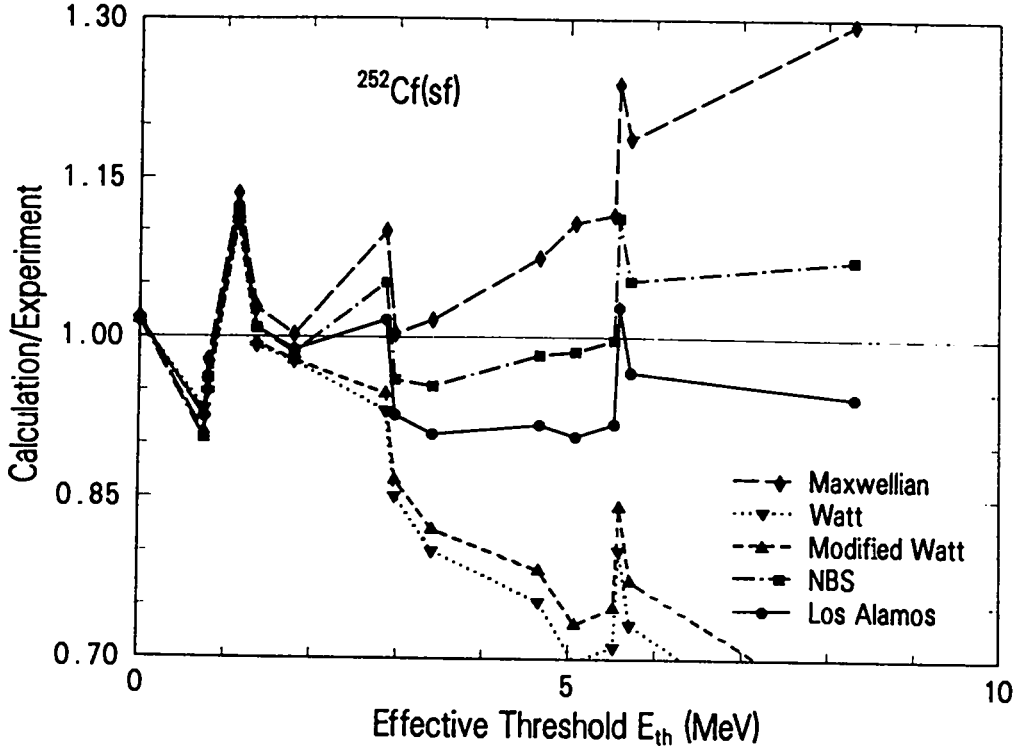

Fig. 54. Integral cross-section comparisons for spectra adjusted to the Poenitz and Tamura experiment (Ref. 90).

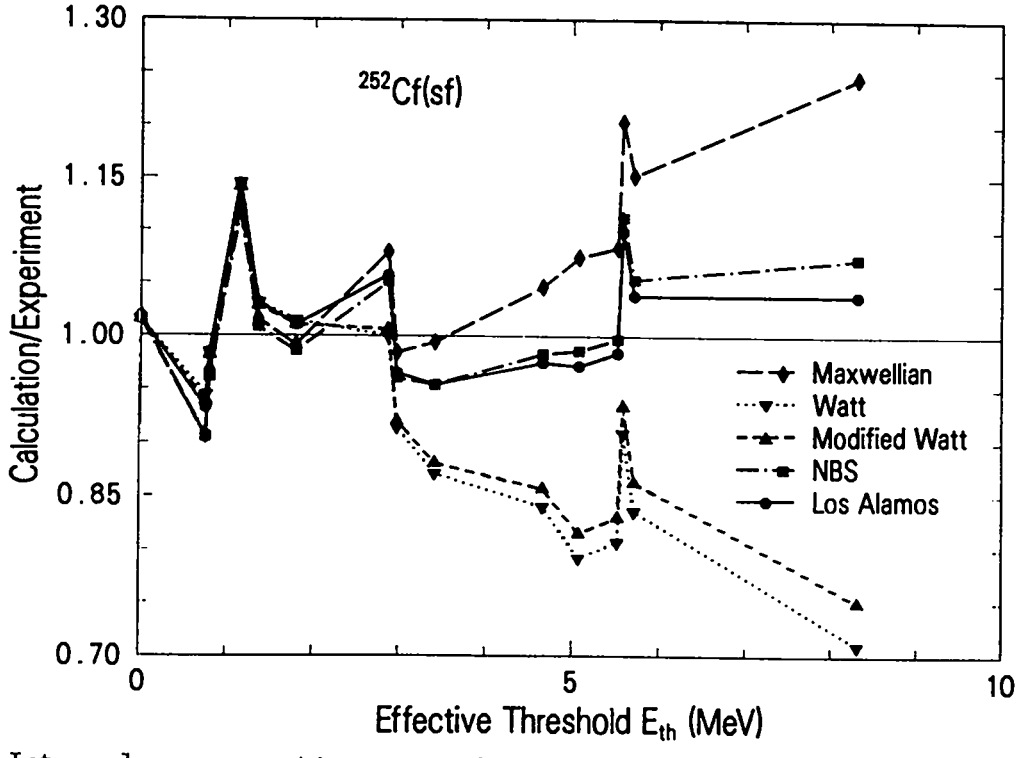

Fig. 55. Integral cross-section comparisons for spectra adjusted to the Boldeman et al. experiment (Ref. 91).

V. Coupled Energy-Angle Distributions of Recoiling Nuclei (D. G. Foster, Jr. and R. E. MacFarlane)

In previous reports[95,96] we have described a new code system for calculating the coupled energy-angle distributions of particles and recoil nuclei. This system takes advantage of recently increased flexibility in File 6 of the ENDF/B system. Briefly, whenever we calculate a series of nuclear reactions with the GNASH code,[8] we store all of the individual increments of cross sections for subsequent reanalysis. A new code named RECOIL reads these increments and uses a modification of the Kalbach-Mann formalism[79] to calculate the resulting angular distributions of the particles emitted during the subsequent decays. By summing the resulting recoils over the successive particle emissions and averaging over angles, RECOIL constructs a Legendre expansion of the angular distribution, as a function of secondary energy, for each recoil species.

In making these calculations, we have modified the Kalbach-Mann formalism in two respects. The first is to force all of the Legendre coefficients to go quadratically to zero at zero secondary energy, while still joining the original curves reasonably smoothly. The second is to adopt curves for the first two Legendre coefficients for neutrons that are different from the curves for charged particles. The curves for neutrons were derived by fitting measured angular distributions for inelastic neutron scattering from iron; these exhibit substantially more forward peaking below 20 MeV than do charged-particle measurements.

The output from RECOIL consists of fragments of the desired ENDF records. These are retrieved from intermediate storage in the correct order by a second new code named MAKE6, which writes the results directly in the required formats for Files 3, 6, 12, and 15.

We have used RECOIL and MAKE6 to generate the coupled energy-angle distributions for ^{56}Fe from 5.25 to 36 MeV, using the GNASH calculations from the 1980 evaluation by Arthur and Young.[23] Unfortunately, RECOIL is so expensive to run that we could not afford to use a fine enough mesh in averaging over angular distributions, so the resulting recoil angular distributions for minor recoil species are useless. Accordingly, we modified MAKE6 to reject angular distributions that are clearly faulty. We also added an input parameter to suppress recoil angular distributions in which neither of the first two Legendre coefficients exceeds a specified threshold (typically 0.1). Even with these omissions, the resulting additions to the ENDF file total more than 7000 lines.

Taking advantage of the flexibility permitted by the rules for File 6, we treated only the (n,n'), (n,p), and (n,α) reactions explicitly over the entire range of primary energies. We treated the (n,2n) reaction explicitly from threshold to 20 MeV, then buried it in MT = 99 above 20 MeV, along with all the other minor reactions. The resulting cross section file for MT = 99 above 20 MeV therefore begins with a subsection for each of the three light particles (neutron, proton, alpha particle), followed by eight subsections for the minor heavy recoils. Figure 56 displays the resulting cross sections, as recorded in File 3. The "total" cross section shown is incomplete, because the shape-elastic cross section has been omitted.

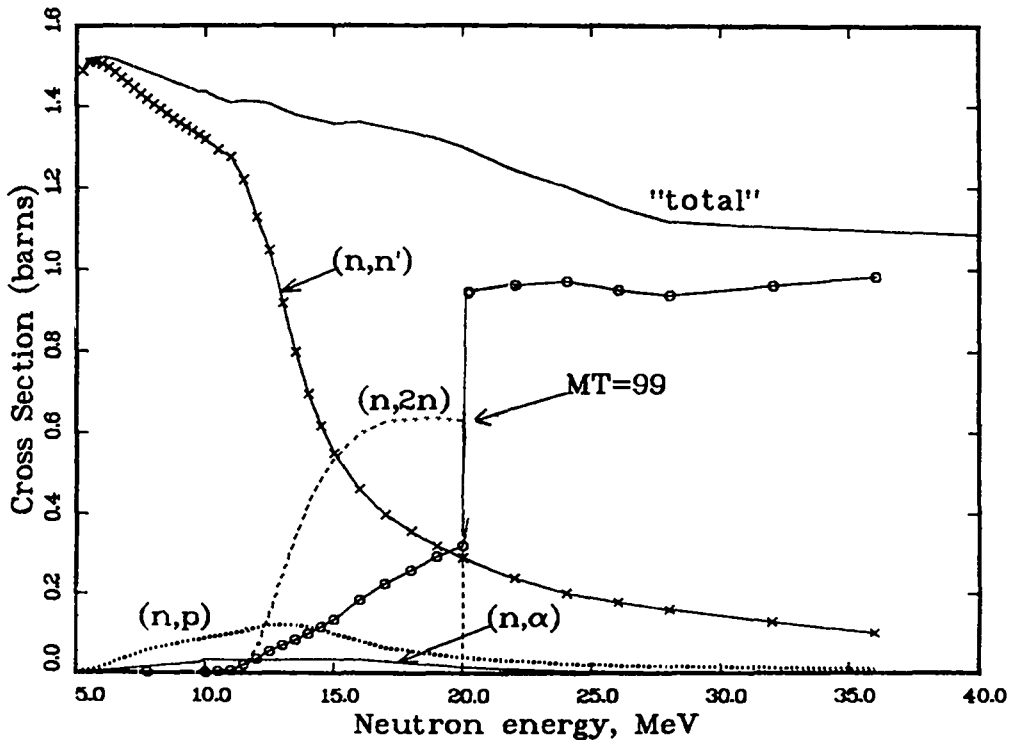

Fig. 56. Reaction cross sections included in this work. The "total" cross section does not include the shape-elastic contribution.

Figure 57 illustrates a typical particle spectrum at the highest energy in our calculations. The spectrum is normalized to have an integral of unity, as required for ENDF/B. The apparently empty portion at lower energies has been drained of most of its cross section by transitions that left enough energy for another emission, in this case to the (n,2n) or higher-order reactions. Typically, the preequilibrium fraction saturates at 1.0 for these very energetic emissions. The sharp bend in the preequilibrium-fraction curve is the result of a rather crude treatment in GNASH.

Figure 58 shows the spectrum of ^{56}Fe recoils that corresponds to Fig. 57. Because the recoil bin-width in RECOIL is self-scaling, the apparent width of the discrete structure is distorted by differences in relative bin width. The dashed and dotted lines exhibit the energy dependence of the first two Legendre coefficients. The negative values for $\ell = 1$ reflect the fact that the average direction is backwards in the center-of-mass frame. At much lower energies, the $\ell = 2$ coefficient frequently is larger than that for $\ell = 1$.

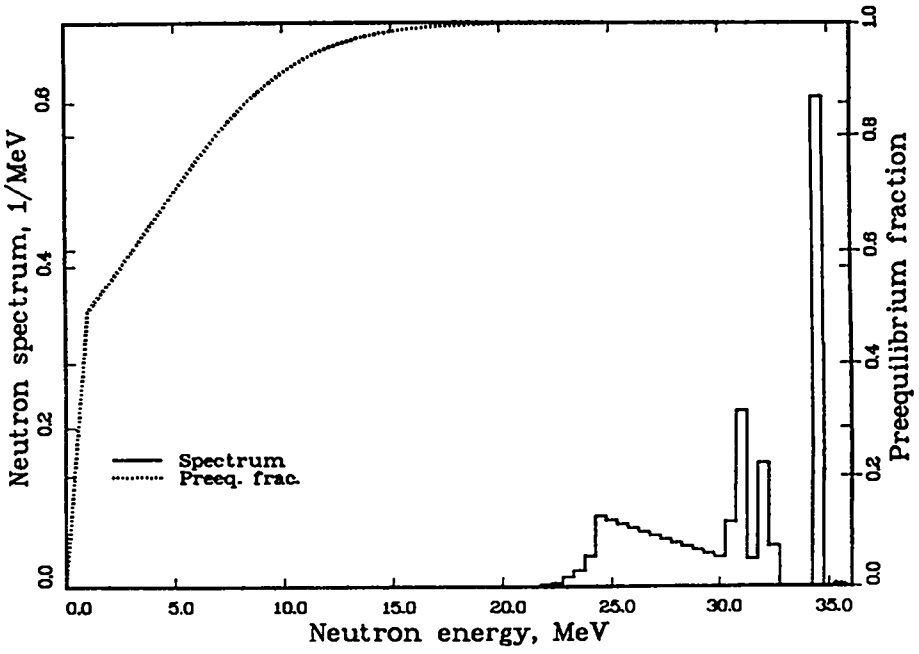

Figure 57. Normalized neutron spectrum and its associated preequilibrium fraction for the (n,n') reaction at 36 MeV.

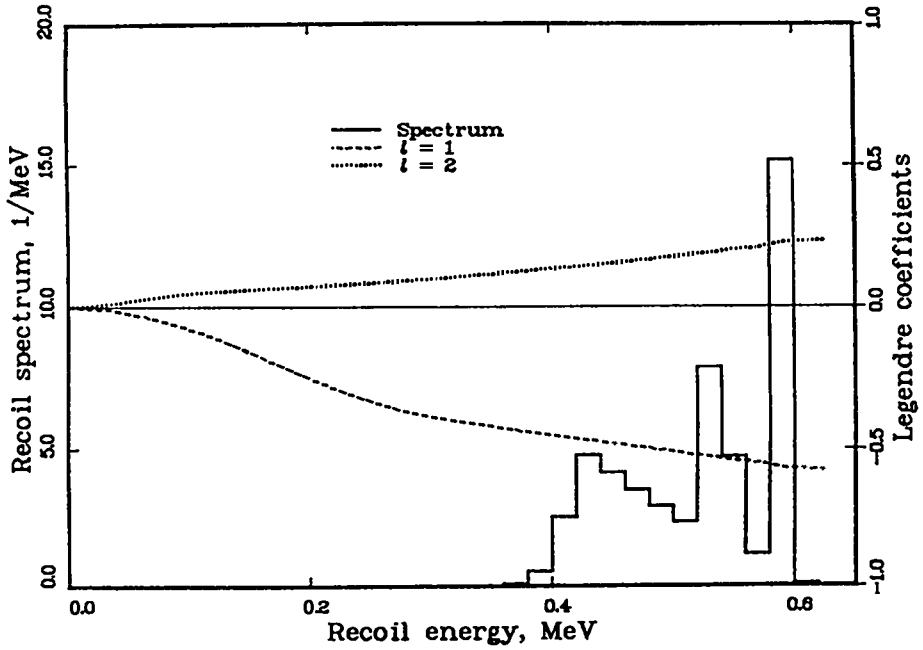

Fig. 58. ^{56}Fe recoil spectrum and angular distribution corresponding to Fig. 57.

W. Tests of the GNASH Preequilibrium Model at Low Energies (D. W. Muir)

In the course of a series of calculations[97] of neutron reactions on ^{59}Co, using a version of GNASH now operational on the CRAY-1 at Harwell,[98] it was observed that the preequilibrium calculation did not converge properly at an incident neutron energy of 8 MeV, while it did converge at nearby energies, both above and below this energy. In order to further examine this discontinuous behavior, an identical code version was implemented on the Los Alamos CRAY machines. Identical behavior was then seen in Los Alamos repetitions of the Harwell runs. Numerical experimentation and analysis of the code has revealed that the observed behavior is a natural consequence of the algorithm used in subroutine RESOL to detect the onset of equilibrium in the solution of the "master equations."[99] While the problem can be avoided with existing GNASH versions by simply turning off the preequilibrium treatment at low energies (where the preequilibrium effect is small anyway), we have implemented an improved convergence test in RESOL that effectively avoids the problem.

II. NUCLEAR CROSS-SECTION PROCESSING AND TESTING

A. NJOY Development (R. E. MacFarlane)

The NJOY nuclear data processing system[100] is now in use all over the world, and with the increasing international standardization on ENDF-type formats, NJOY use should expand even further. The development of NJOY has proceeded through a series of dated "versions" [e.g., NJOY(6/83)] and numbered "revisions" [e.g., (6/83-2)]. We are now in the process of releasing NJOY (6/83-3). The major changes made since revision 2 are described below.

Many changes were made to handle the new ENDF/B-VI formats; RECONR, BROADR, UNRESR, THERMR, MODER, and GAMINR are all essentially Version-VI compatible in NJOY(6/83-3). See the discussions of thermal changes, the Reich-Moore option, and photon-interaction processing in Sec. B, Chapter II of this report.

The efforts to improve the transportability of NJOY have continued, and the use of FORTRAN-77 has increased (see OPENZ and PACK especially). The "overlay" type structure has been changed to a "segment" structure that seems to be consistent with more systems. The use of local plotting routines in DTFR has been reduced, and a FORTRAN-77 version of the "Draw Large Characters" routine has been written. Only low-level routines, such as "draw a vector" and "advance page" are needed to convert the DTFR plotting logic to a new system.

In response to the most common criticism of GROUPR, a more automated way to request the processing of a series of reactions has been added. The single input card "3/" will now cause the processing of all the reactions on the PENDF tape (except thermal). Similarly, "6/" will request all neutron transfer matrices (except thermal), and "16/" will generate all photon production matrices. Optional quantities such as thermal data, average inverse velocity, or delayed-neutron data must still be requested explictly.

A new interactive method for choosing the energy grid for Doppler-broadened cross sections was installed in BROADR. This method corrects some small inaccuracies noticed by S. Ganesan (Reactor Research Centre, Kalpakkam, India), and it actually improves the speed of BROADR for heavy isotopes. In addition, the input instructions for BROADR were modified slightly to provide the same control over reconstruction and thinning used by RECONR. Test calculations have shown that the older method was perfectly adequate for producing multigroup data at the 1/8 to 1/4 lethargy level if reasonably tight tolerances were used (1% or better). However, the newer method gives improved point-cross-section results, and some small changes may be seen if very fine group structures (for example, 640 groups) are used.

Several ENDF/B-V elemental evaluations have energy regions where resolved- and unresolved-resonance representations overlap. These evaluations are not processed correctly by NJOY (6/83-2). We have modified RECONR, BROADR, UNRESR, and GROUPR to detect such overlaps. In BROADR, the smooth unresolved part is removed from the reaction cross section in the overlap range, the remainder is broadened, and the smooth part is added back onto the result. In GROUPR, the resolved part of the cross section in the overlap range is separated from the unresolved part and used as part of the σ_0 background cross section when computing the effective self-shielded value of the unresolved part of the cross section.

In addition to the ENDF/B-VI upgrades in THERMR described elsewhere, several improvements were made to the calculational methods for thermal data. A number of these problems were reported by M. Mattes (University of Stuttgart) and some were found by looking at detailed plots of thermal data using an upgraded plotting code. THERMR now does a better job with both incident and secondary energy grids. Figure 59 shows examples for two interesting moderators. People interested in using NJOY for thermal neutron cross sections should upgrade to version 6/83-3 as soon as possible.

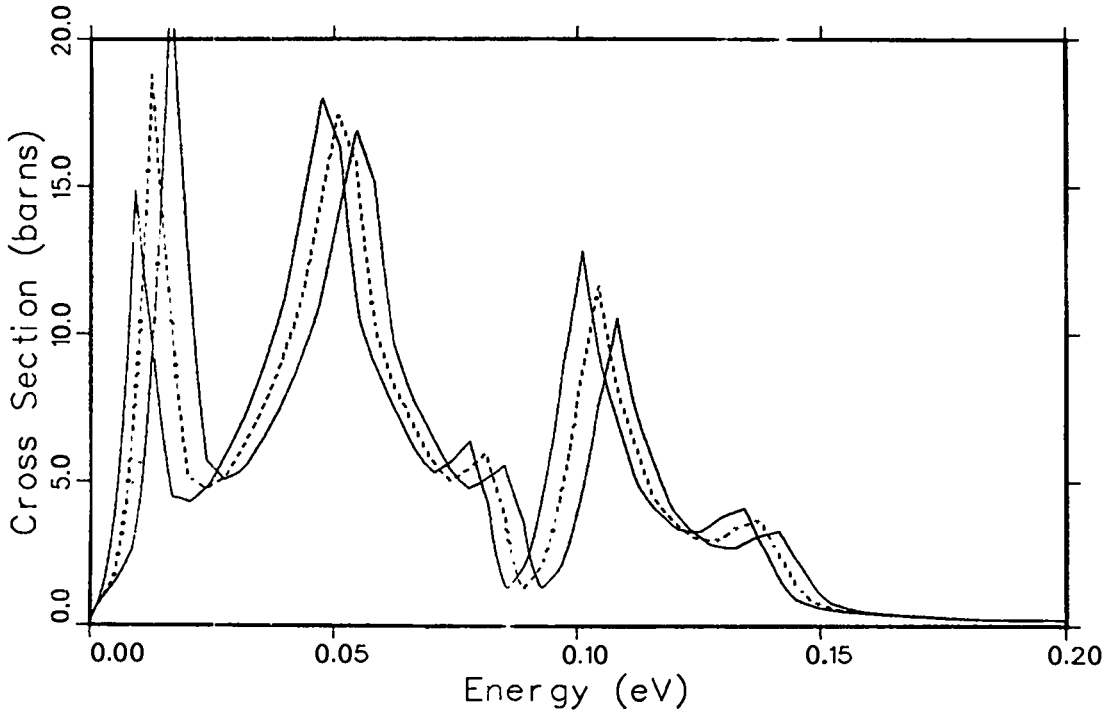

Fig. 59 (a)

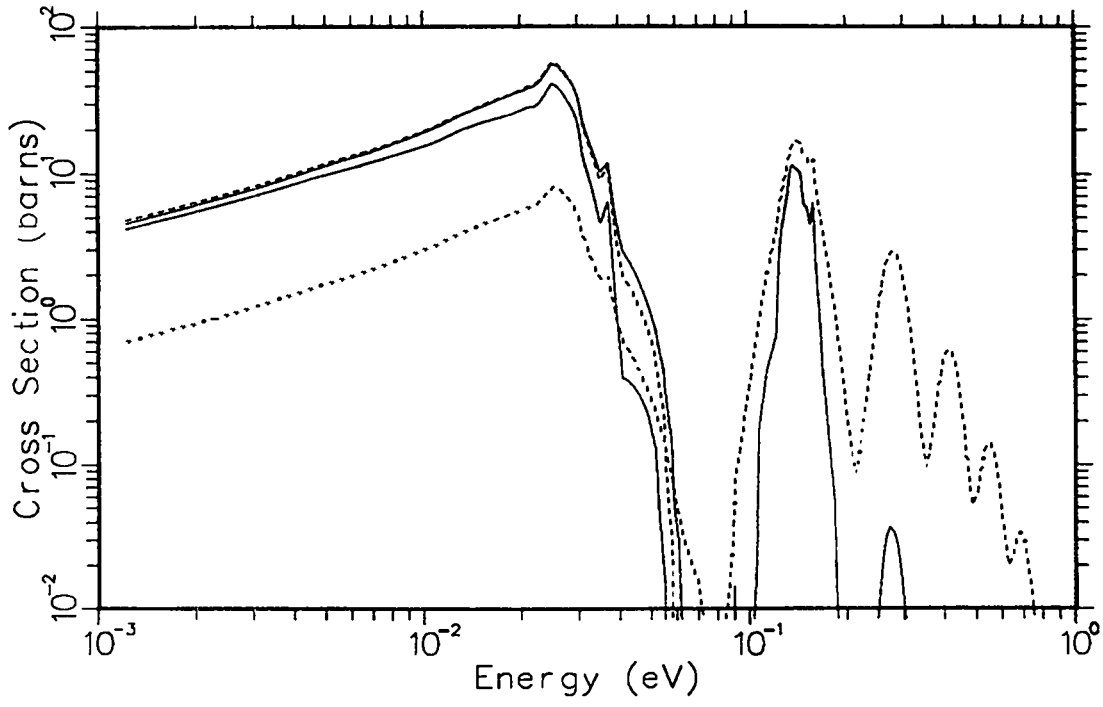

Fig. 59(b)

Fig. 59. Examples of THERMR calculations: (a) BeO at 600 K for three incident energies near 0.01 eV, (b) H in ZrH for an incident energy of 0.01 eV at temperatures of 300, 600, 800 and 1200 K.

Two new volumes of the NJOY report, namely LA-9303-M, Volumes III and IV, are now complete.[101,102] Volume III describes the GROUPR and GAMINR modules, which prepare multigroup cross sections for neutron and photon transport and responses, and the MODER module, which performs mode conversion and certain other operations on ENDF/B and NJOY output files. Volume IV describes the ERRORR and COVR modules, which are concerned with the covariances of multigroup cross sections and fission $\bar{\nu}$ values. The new volumes provide detailed descriptions of the theory and methods used in these five modules and they provide more complete (and more up-to-date) descriptions of the user input than that given in the general NJOY user's manual.[100]

B. Reich-Moore Resonance Format (R. E. MacFarlane)

The use of the Reich-Moore resonance format has been approved for nonfissionable isotopes for ENDF/B-VI. We have borrowed some coding from the National Nuclear Data Center (Brookhaven) ENDF-VI checking code PSYCHE and modified it for RECONR, the resonance reconstruction module of NJOY. Provision was also made to include fission channels for testing or for use in other evaluation communities. The new option has been testing using a sample problem provided by D. Larson of Oak Ridge National Laboratory. Results also have been sent to D. E. Cullen at the International Atomic Energy Agency (IAEA) for comparison with other Reich-Moore results.

C. Photon Interaction Cross Sections (R. E. MacFarlane)

The existing photon interaction cross-section libraries available at Los Alamos are based on the DLC-7E library* in ENDF/B-IV format, as processed by NJOY. Recently, there have been three developments that make it desirable to upgrade our processed data libraries. First, a new version of the evaluated data library has been released in ENDF/B-V format. This one is called DLC-99/HUGO,* and its contents are described in Ref. 103. Second, a new format for photon interaction data has been adopted for ENDF/B-VI. Third, we have always felt that the GAMINR module was too slow.

Based on these developments, we decided to update the GAMINR module of NJOY to handle the ENDF-6 format and to be more efficient. The efficiency gain was obtained by taking advantage of the fact that incoherent photon scattering is

* The DLC-7E and DLC-99 libraries are available from the Radiation Shielding Information Center at the Oak Ridge National Laboratory.

proportional to the charge number Z at high energies. The energy above which proportionality holds increases with Z, and in a series of calculations for gradually increasing Z, the new code simply rescales some of the results from the previous step to get the high-energy groups for the current element.

We also converted the DLC-99/HUGO library to ENDF-VI format and supplied the result to the National Nuclear Data Center at the Brookhaven National Laboratory.

The new version of GAMINR was tested on all three libraries, and the modifications are now available in NJOY (6/83-3). Multigroup libraries for the DLC-99 evaluations will be generated in 12 and 24 groups in the near future.

D. ENDF/B-VI Thermal Data (R. E. MacFarlane)

As a part of the development work for the ENDF-6 format, we examined the representations used for thermal neutron scattering data in the previous versions of ENDF/B. The following problems and shortcomings were noticed.

1. It is often necessary to compute incoherent inelastic scattering for energy or momentum transfers outside the range of the tabulated $S(\alpha,\beta)$. This kind of extension is normally done using the "short-collision-time" approximation, which requires a table of effective temperature versus moderator temperature. These effective temperatures have been computed from the same frequency distribution models used to generate $S(\alpha,\beta)$, and the temperatures are given in ENDF-269.[104] They currently must be transferred to the input of the processing codes by hand. It would be better to add a supplementary table to the format for MF=7, MT=4.

2. Incoherent elastic scattering (polyethylene, ZrH_x) is currently represented as a temperature-dependent tabulated cross section in File 3 (MT=2) and an angular distribution in File 4. A more accurate angular distribution (especially for Monte-Carlo) can be obtained if one knows the effective bound cross section and the Debye-Waller integral. Once again, these data are given in ENDF-269 and must be transferred to the processing code by hand.

3. Coherent elastic scattering (Be, BeO, graphite, UC, UO_2) is represented in the same way. It is currently possible to reconstruct the exact angular

distribution from File 3 by locating Bragg edges and subtracting cross sections to get structure factors (this method was developed for NJOY). When this is done, the existing File 4 is no longer required. It turns out that an even more compact representation using File 7, MT2 instead of File 3, MT2, is desirable.

4. Temperature dependent cross sections are given using a rarely used format. The values in the file may not be consistent with those computed from the standard File 2 + File 3 data for the evaluation. Cross-section tabulations should be removed from the thermal files.

5. Some compound evaluations (BeO, Benzine) give the molecular $S(\alpha,\beta)$ in File 7 rather than the $S(\alpha,\beta)$ for one atom in the compound (H in H_2O). Such evaluations require cross-section and effective temperature data for the secondary atom.

Repairs for these problems were incorporated into a format proposal for File 7 in ENDF-6. This proposal has been accepted.

In order to transfer data from the old format to the new, a simple translation code has been written. It takes as much information as possible from the old ENDF/B-III thermal evaluations (tapes 320, 321, ...), and requests user input for the balance of the information; that is, new MAT numbers, new comment cards, bound atom cross section and Debye-Waller integral for incoherent elastic scattering, parameters for SCT approximation in mixed moderations (BeO), and tables of effective temperatures for the SCT approximation.

This conversion process has been carried out for several existing evaluations. The work will be completed in the near future, and the results will be made available to the Cross-Section Evaluation Working Group (CSEWG) through NNDC.

Conversion does not remove shortcomings in the original data. Some of the outstanding problems include the following.

1. Upper energies for the thermal treatments are generally too low.

2. Some of the free atom cross sections in File 7 do not agree with the cross section values in the latest evaluations for the materials.

3. Grids for α and β are sometimes too coarse.

4. Some $S(\alpha,\beta)$ values are set to zero in the files when they get "small." Unfortunately, the definition of "small" is too large, and these zeros lead to problems in computed cross sections when attempts are made to extend the calculations to higher energy transfers.

Some of these problems should probably be worked on before the ENDF/B-VI files are released.

E. Cross-Section Production (D. C. George, R. E. MacFarlane)

In order to support various Q-Division programs, neutron cross sections in 69- and 80-group MATXS library formats were prepared for the following materials:

Material	Temperature	σ_o
Re-185	1200, 2100, 3100	10^{10}
Re-187	1200, 2100, 3100	10^{1}-10^{10}
Nb-93	2100, 3100	10^{1}-10^{10}
Ta-181	2100, 3100	10^{1}-10^{10}
W-182,183,184,186	1200, 2100, 3100	10^{1}-10^{10}
U-235	3100	10^{1}-10^{10}
U-238	3100	10^{1}-10^{10}

In addition, temperature-dependent cross sections for the MCNP Monte-Carlo codes were prepared for the following materials:

Material	Temperature	Scattering Laws
H-1	300, 400, 500, 600, 800	H_2O, Benz
H-1	300	Poly
H-1	300, 400, 500, 600, 800, 1200	ZrH
Li-6	300, 1200	
Li-7	300, 1200	
Be-9	300, 600, 800, 1200	Metal, BeO
C	300, 600, 800, 1200, 1600, 2000	Graphite
Na-23	300, 1200	
K	300, 1200	
Cr	300, 1200	
Fe	300, 1200	
Ni	300, 1200	
Sm-149	300, 1200	
Xe-135	300, 1200	
Mn-55	300, 1200	
Zr	300, 4000, 600, 800, 1200	ZrH

(continued)

Material	Temperature	Scattering Laws
Nb	300, 1200	
Mo	300, 1200	
Eu-151	300, 900	
Eu-153	300, 900	
Ta-181	300, 1200	
W_{nat}	300, 1200, 1800	
Re-185	300, 1200	
Re-187	300, 1200	
U-235	300, 1200, 1800	
U-238	300, 1200, 1800	
Pu-239	300, 1200, 1800	

A special cross-section library was prepared for ESS-Division to be used to compute neutron scattering in the soil of Mars and to describe the transport of the scattered neutrons through the Martian atmosphere to an orbiting neutron detector. This system shows promise of being able to map the occurrence of water on Mars. A future library will include the low temperature (200 K) scattering cross sections for water needed for more realistic calculations.

Because of the various improvements to NJOY described elsewhere in this report, we have begun a program to recompute cross sections that may be particularly affected. We are also trying to complete the processing of all the evaluations prepared for ENDF/B-V revision 2. Some recent jobs under this program follow.

Material	Format
H-1	PENDF, 69x24 GENDF
H-2	PENDF, 69x24 GENDF
H-3	PENDF
He-3, He-4	PENDF
Be-9	PENDF, 69x24 GENDF
C	PENDF, 69x24 GENDF
Cl	69x24 GENDF
Mg	69x24 GENDF
Ar	PENDF
Zr	PENDF, 69x24 GENDF
Pu-239	PENDF, 69x24 GENDF, 80x24 GENDF
Pu-240	PENDF, 69x24 GENDF, 80x24 GENDF, ACER

III. NEUTRON ACTIVATION, FISSION PRODUCTS, AND ACTINIDES

A. Delayed Neutron Spectra from Fission Pulses [T. R. England, M. B. Butler, E. D. Arthur, A. Sierk (T-9), C. W. Maynard (Univ. of Wisconsin), and F. M. Mann (Hanford Engineering Development Laboratory)]

Current work is directed toward an improvement in precursor data suitable for aggregate, time-dependent calculations in summation codes. This includes direct fission yield distributions, delayed neutron emission probabilities (Pn) and precursor spectra. Calculations require similar information for the precursor parents.

Most recent efforts have been on a reevaluation of Pn values and on expansion of the individual precursor spectra. The fission yields in use are described in Ref. 105, with the exception of ^{238}U fast fission, in which the proton pairing parameter has been reduced by approximately a factor of two.

1. Pn Values.

The current evaluation includes data through mid-1985. The evaluated measured data (82 nuclides) are also used to derive fitting parameters for the Hermann-Kratz equation[106] and the results used to estimate unmeasured Pn values for 28 nuclides. The evaluation process is described in Ref. 107. Table X lists the currently evaluated and estimated Pn's; the estimated values can be identified by the lack of an uncertainty. The actual uncertainty is probably a factor of two or more, but the 28 precursors having estimates account for only a few per cent of the total calculated delayed neutron rate (<10% at equilibrium). In addition, Table X lists the sources of spectra and the time-group assignment in the conventional six groups. The basis of the group assignment is discussed in Ref. 108; however, group assignments are not used in the current calculations. Instead, we use the precursors and their parents in explicit summation calculations. The additional data needed for such calculations are based on ENDF/B-V and listed in Ref. 109, with the exception of more recent Pn, yield and delayed spectra data.

2. Number of Precursors.

Currently we are using 110 precursors and their parents--about 228 nuclides. Based on energetics derived from mass tables, there should be > 270 precursors.[108] These additional precursors are generally very short-lived and have small yields. We have examined the effect of these probable precursors only

on the total delayed neutron rate at equilibrium and find that they would increase the calculated rate by only 1-2%. We will examine these for fission pulses, and particularly for their contribution to high-energy delayed neutrons during the next T-2 Progress Report coverage.

TABLE X

Pn VALUES AND SOURCE OF DATA[a]

Cs	ZZAAAS	HL(s)	Pn	Uncert.	Gp.	Source Pn	Source Spec.
Zn	300790	0.313	0.3521		5	Theory	Theory
Ga	310790	3.00	0.2280	+/- 0.2670	4	Meas.	Meas.1
Ga	310800	1.66	0.2290	+/- 0.3800	4	Meas.	Meas.1 +aug.
Ga	310810	1.23	11.0000	+/- 0.8300	4	Meas.	Meas.1 +aug.
Ga	310820	0.60	20.4000	+/- 1.6900	5	Meas.	Theory
Ga	310830	0.31	50.0000	+/- 6.8500	5	Meas.	Theory
Ge	320830	1.9	0.0040*		4	Theory	Theory
Ge	320840	1.2	2.7752		4	Theory	Theory
Ge	320850	0.250	9.3856	+/- 8.0000	6	Meas.	Theory
Ge	320860	0.247	10.1508		6	Theory	Theory
As	330840	5.3	0.0870	+/- 0.0440	3	Meas.	Theory
As	330850	2.03	62.0320	+/- 7.9284	4	Meas.	Meas.1 +aug.
As	330860	0.9	8.6692	+/- 1.9957	4	Meas.	Theory
As	330870	0.30	43.8296	+/-19.9397	6	Meas.	Theory
Se	340870	5.60	0.1690	+/- 0.0220	3	Meas.	Theory
Se	340880	1.50	0.8530	+/- 0.0120	4	Meas.	Theory
Se	340890	0.427	10.5219	+/- 3.2998	5	Meas.	Theory
Se	340900	0.555	5.4752		5	Theory	Theory
Se	340910	0.27	15.5068		6	Theory	Theory
Br	350870	55.7	2.5600	+/- 0.2000	1	Meas.	Meas.2
Br	350880	16.0	6.3400	+/- 0.5000	2	Meas.	Meas.1
Br	350890	4.38	14.1000	+/- 1.0900	3	Meas.	Meas.2 +aug.
Br	350900	1.80	24.9000	+/- 2.3600	4	Meas.	Meas.2 +aug.
Br	350910	0.600	18.3000	+/- 1.8700	5	Meas.	Meas.2 +aug.
Br	350920	0.360	43.7318	+/-12.3346	5	Meas.	Meas.2 +aug.
Br	350930	0.176	24.0476		6	Theory	Theory
Kr	360920	0.360	0.0327	+/- 0.0038	5	Meas.	Theory
Kr	360930	1.29	1.9900	+/- 0.1900	4	Meas.	Theory
Kr	360940	0.210	6.3300	+/- 2.4900	6	Meas.	Theory
Kr	360950	0.780	6.4000	+/- 3.7000	5	Meas.	Theory
Rb	370920	4.53	0.0101	+/- 0.0007	3	Meas.	Meas.2
Rb	370930	5.86	1.3700	+/- 0.0900	3	Meas.	Meas.1 +aug.
Rb	370940	2.76	10.2000	+/- 0.6700	4	Meas.	Meas.2 +aug.
Rb	370950	0.380	8.7900	+/- 0.5600	5	Meas.	Meas.1 +aug.
Rb	370960	0.204	14.2000	+/- 0.9400	6	Meas.	Meas.2 +aug.
Rb	370970	0.170	27.1000	+/- 1.9600	6	Meas.	Meas.2 +aug.
Rb	370980	0.110	13.5000	+/- 1.0300	6	Meas.	Meas.2 +aug.
Rb	370990	0.145	16.0000	+/- 2.2000	6	Meas.	Theory
Sr	380970	0.40	0.0055	+/- 0.0026	5	Meas.	Theory
Sr	380980	0.65	0.3030	+/- 0.0540	5	Meas.	Theory
Sr	380990	0.6	0.4770	+/- 0.1480	5	Meas.	Theory
Sr	381000	0.618	0.7380	+/- 0.0490	5	Meas.	Theory

TABLE X (Cont.)[a]

Cs	ZZAAAS	HL(s)	Pn	Uncert.	Gp.	Source Pn	Source Spec.
Y	390971	1.11	0.1110 +/-	0.0370	4	Meas.	Theory
Y	390970	3.7	0.0560 +/-	0.0053	3	Meas.	Theory
Y	390981	0.65	3.4800 +/-	0.9800	5	Meas.	Theory
Y	390980	2.0	0.2420 +/-	0.0190	4	Meas.	Theory
Y	390990	1.4	1.0400 +/-	0.1870	4	Meas.	Theory
Y	391000	0.800	0.8190 +/-	0.0590	5	Meas.	Theory
Zr	401040	2.573	0.0481		4	Theory	Theory
Zr	401050	0.493	0.3571 +/-	0.7700	5	Meas.	Theory
Nb	411030	1.500	0.0021*		4	Theory	Theory
Nb	411040	4.80	0.0078*		3	Theory	Theory
Nb	411050	2.800	0.9962*		4	Theory	Theory
Nb	411060	1.000	0.1633		4	Theory	Theory
Mo	421090	1.409	0.0292		4	Theory	Theory
Mo	421100	2.772	0.5545		4	Theory	Theory
Tc	431090	1.40	0.0199*		4	Theory	Theory
Tc	431100	0.83	0.0972		4	Theory	Theory
Ag	471210	0.8	0.0770 +/-	0.0050	5	Meas.	Theory
Ag	471220	1.5	0.1880 +/-	0.0120	4	Meas.	Theory
Ag	471230	0.39	0.5560 +/-	0.0350	5	Meas.	Theory
Cd	481280	1.053	0.0295		4	Theory	Theory
In	491271	1.300	0.7000 +/-	0.0800	4	IN127	IN127
In	491270	3.76	0.5820 +/-	0.0500	3	Meas.	Theory
In	491280	0.84	0.0600 +/-	0.0090	4	Meas.	Theory
In	491291	2.5	2.2500 +/-	1.4300	4	Meas.	IN129
In	491290	0.99	2.9400 +/-	0.4500	4	Meas.	Meas.1
In	491301	0.111	1.5600 +/-	0.1240	6	Meas.	IN130
In	491300	0.58	0.9450 +/-	0.2850	5	Meas.	Meas.1
In	491311	0.111	1.7600 +/-	0.2500	6	Meas.	IN131
In	491310	0.28	1.6000 +/-	0.3320	6	Meas.	Theory
In	491320	0.12	6.5200 +/-	0.6850	6	Meas.	Theory
Sn	501330	1.47	0.0722*		4	Theory	Theory
Sn	501340	1.04	18.9000 +/-	14.4000	4	Meas.	Meas.1 +aug.
Sn	501350	0.418	5.2786		5	Theory	Theory
Sb	511340	10.200	0.1160 +/-	0.0120	2	Meas.	Theory
Sb	511350	1.82	17.8900 +/-	1.5400	4	Meas.	Meas.1 +aug.
Sb	511360	0.82	29.8225 +/-	3.9095	4	Meas.	Theory
Sb	511370	0.478	20.479		5	Theory	Theory
Te	521360	19.0	1.1700 +/-	0.5400	2	Meas.	Meas.1
Te	521370	3.5	2.7800 +/-	0.6600	3	Meas.	Theory
Te	521380	1.6	7.0000 +/-	2.3500	4	Meas.	Theory
Te	521390	0.580	4.4045		5	Theory	Theory
I	531370	24.5	7.0500 +/-	0.5400	2	Meas.	Meas.1
I	531380	6.50	5.4300 +/-	0.5400	3	Meas.	Meas.1
I	531390	2.38	9.9400 +/-	0.8000	4	Meas.	Meas.1 +aug.
Sr	381000	0.618	0.7380 +/-	0.0490	5	Meas.	Theory
I	531400	0.860	9.3500 +/-	0.9900	4	Meas.	Meas.1 +aug.
I	531410	0.46	21.5000 +/-	3.9000	5	Meas.	Meas.1 +aug.

TABLE X (Cont.)[a]

Cs	ZZAAAS	HL(s)	Pn	Uncert.	Gp.	Source Pn	Source Spec.
I	531420	0.200	5.5341		6	Theory	Theory
I	531430	0.401	52.3523		5	Theory	Theory
Xe	541410	1.72	0.0324	+/- 0.0067	4	Meas.	Theory
Xe	541420	1.22	0.3970	+/- 0.0460	4	Meas.	Theory
Xe	541430	0.96	1.3883		4	Theory	Theory
Xe	541440	1.10	2.3953		4	Theory	Theory
Xe	541450	0.9	3.2318		4	Theory	Theory
Cs	551410	24.9	0.0375	+/- 0.0390	2	Meas.	Theory
Cs	551420	1.69	0.0960	+/- 0.0074	4	Meas.	Meas.1
Cs	551430	1.78	1.6300	+/- 0.1100	4	Meas.	Meas.1 +aug.
Cs	551440	1.001	3.1800	+/- 0.2200	4	Meas.	Meas.1 +aug.
Cs	551450	0.59	13.8500	+/- 0.9200	5	Meas.	Theory
Cs	551460	0.340	13.5000	+/- 1.1800	5	Meas.	Theory
Cs	551470	0.546	34.9000	+/-11.5000	5	Meas.	Theory
Ba	561470	1.755	0.0190	+/- 0.0017	4	Meas.	Theory
Ba	561480	3.325	0.0120	+/- 0.0180	3	Meas.	Theory
Ba	561490	0.695	0.4350	+/- 0.1230	5	Meas.	Theory
Ba	561500	0.962	6.8025		4	Theory	Theory
La	571470	5.00	0.0470	+/- 0.0290	3	Meas.	Theory
La	571480	1.3	0.1110	+/- 0.0081	4	Meas.	Theory
La	571490	2.408	0.1008*		4	Theory	Theory

[a]Pn and its uncertainties are listed in per cent. Under Pn Source, the notation of measurement refers to an evaluation of measurements, and theory refers to use of the Herrmann-Kratz equation using fitted parameters based on the measured Pn's. Under Spectra Source, Meas. 1 refers to normalized spectra received from G. Rudstam, and Meas. 2 refers to normalized spectra received from K. Kratz. In either case, +aug. refers to an augmentation of these spectra using the nuclear model code BETA, as discussed in the text. Theory also uses the BETA code for theoretical spectra. The asterisk (*) following the Pn value identifies those theoretical values using Wapstra 1983 mass values. All other nuclides use Wapstra 1981 or Möller-Nix masses.

3. Precursor Spectra.

Presently we have normalized measured spectra for 30 nuclides and we expect to add an additional 4 or more. These 30 account for 80 to 90% of the total delayed neutron emission at equilibrium and after a few seconds decay following a fission pulse, depending on the fissioning nuclide.

Current calculations use measured spectra supplied by G. Rudstam*[110] or K. -L. Kratz,*[111] modified as noted below, and theoretical calculations using the BETA code[112] for unmeasured spectra.

*The actual data files were supplied by G. Rudstam, Swedish Research Councils Laboratory, Studsvik, Sweden, in 1981 and by K. -L. Kratz, Johannes-Gutenberg University, Mainz, Germany, in 1983.

There are a number of problems with spectra. Measured spectra generally do not include the complete energy range. Thus, the ^{3}He spectrometers are generally deficient at energies below ~ 70 keV, and hydrogen recoil spectrometers cover only ~ 1 MeV. Because of the low count rate at high energies, the measured spectra with either spectrometer generally cut off at 3 MeV or less. The measurer reports results normalized over the measured energy range, not absolute values. This presents a difficulty when the spectra from different experiments stressing different energy ranges are to be combined, or when theory is used to extend the spectra. We have generally assumed that the ^{3}He spectrometer results are the most accurate over an energy range that can differ for each emitter. Other results are first normalized to the ^{3}He data using ratios of integrals over a small, common energy range and then added to the ^{3}He data to extend its range. The resulting combined spectra are then renormalized over the total energy range. This procedure is necessarily subjective and requires a detailed examination and individual decision for each emitter.

Before any spectra were combined or extended by theory, we compared the ^{3}He data of Rudstam and Kratz. Figures 60 and 61 are typical of the approximately ten precursors common to each measurer. They are sufficiently similar so that there is little reason to choose one over the other, and uncertainties are sufficiently large that we see no reason to combine these sources into a composite spectrum. The choice made is identified in Table X.

We then examined the range of measured energies using different mass tables and any available level densities, spins, and parities of the precursor's daughter and granddaughter nuclide in the BETA code.[112] This portion of the study was focused at an augmentation of the high-energy spectra, if necessary, of the measured data. Figures 62-65 are typical of the range of comparisons of the theoretical and measured spectra using the mass tables (Q_β and S_n, the neutron separation energy) that best agree with the measured spectra. The BETA code cannot provide the fine energy structure; it generally appears to underpredict the low energy and overpredict the high-energy delayed neutrons. Partially this is a result of the normalization over a larger energy range. However, it could also be that the beta-strength function and level density need improvement. In any case, we are using the BETA code results only for unmeasured spectra and to add a high-energy tail to some of the measured spectra. The tail is first reduced to an approximate value near the end of each measurement. To date it has been reduced essentially to the last measured value, but, in the future, it will

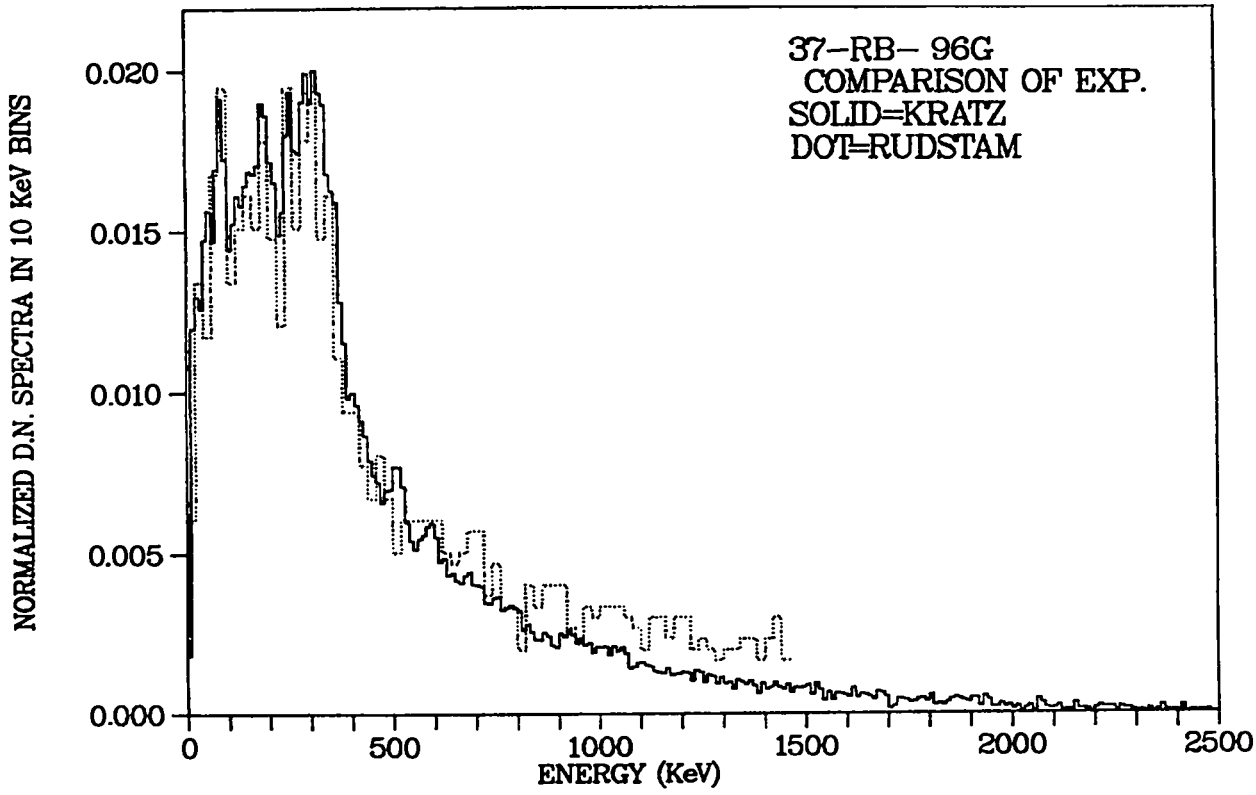

Fig. 60. Normalized delayed neutron spectra for nuclide ^{96g}Rb.

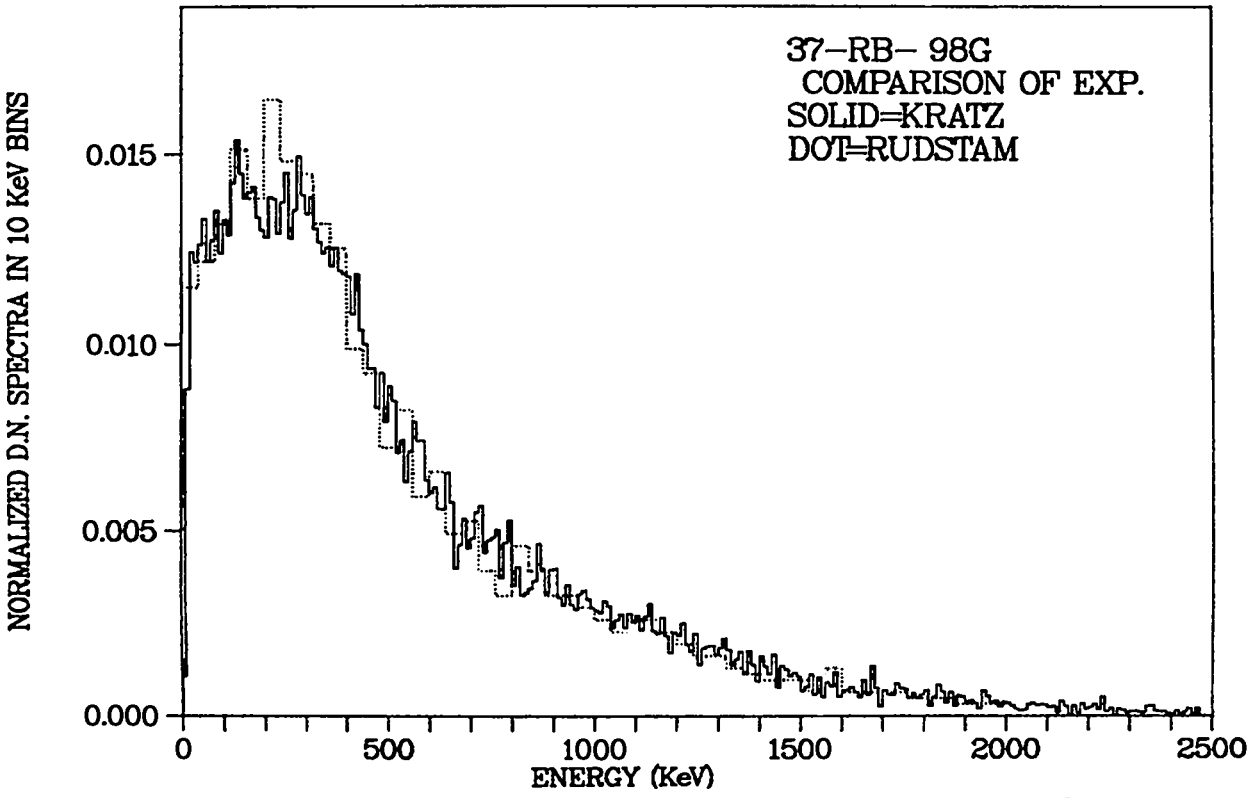

Fig. 61. Normalized delayed neutron spectra for nuclide ^{98g}Rb.

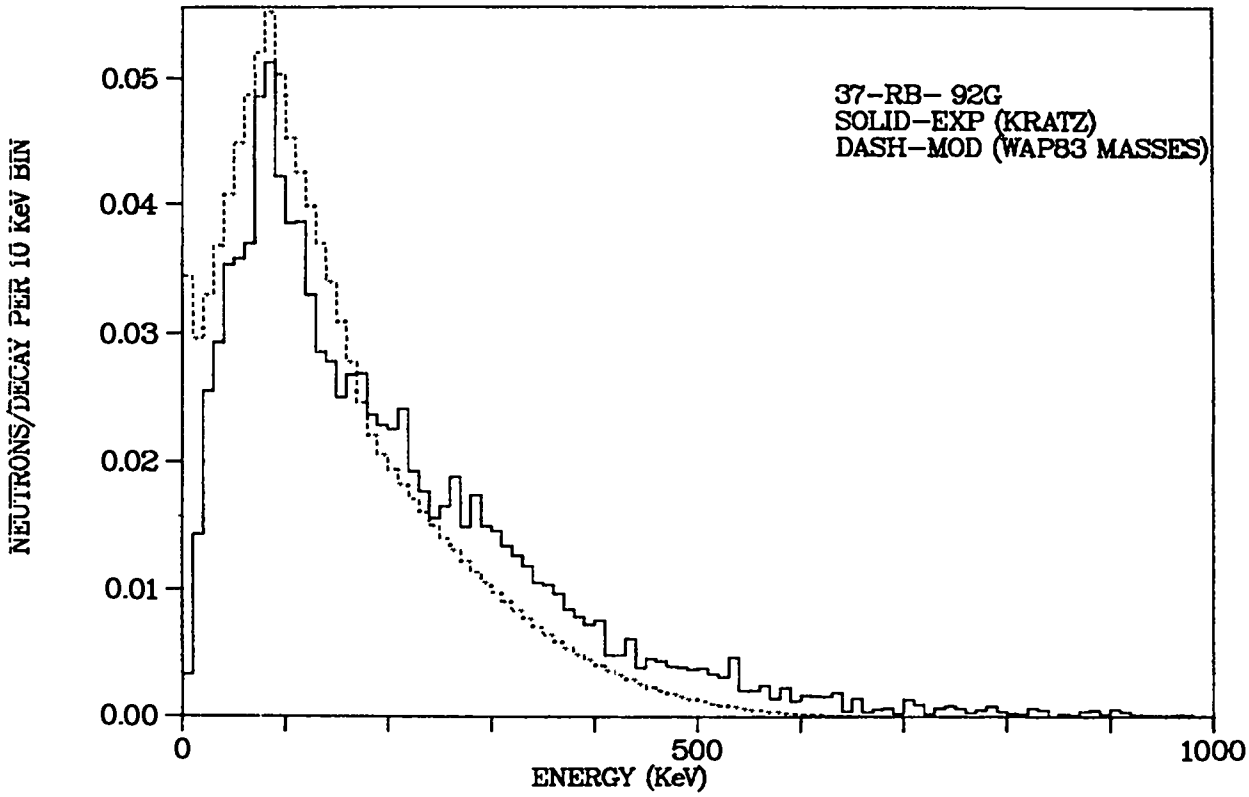

Fig. 62. Normalized delayed neutron spectra for nuclide ^{92g}Rb.

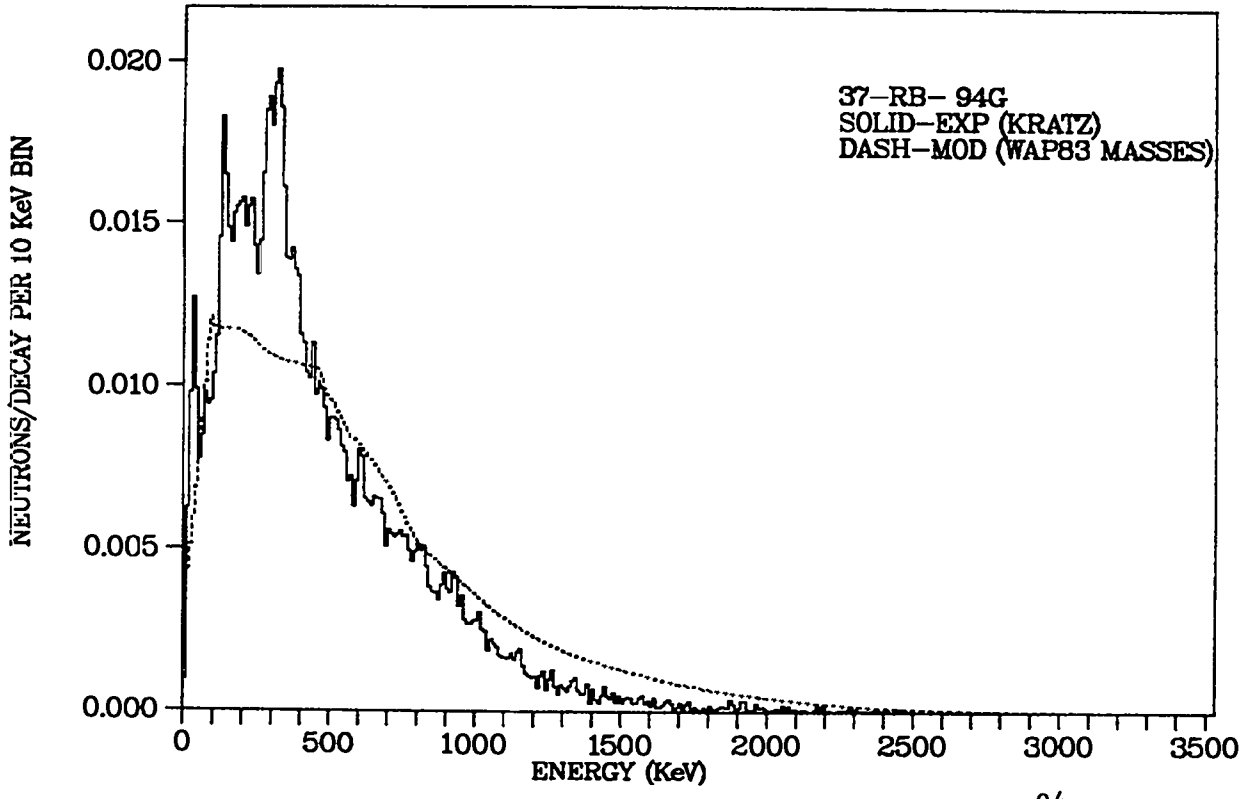

Fig. 63. Normalized delayed neutron spectra for nuclide ^{94g}Rb.

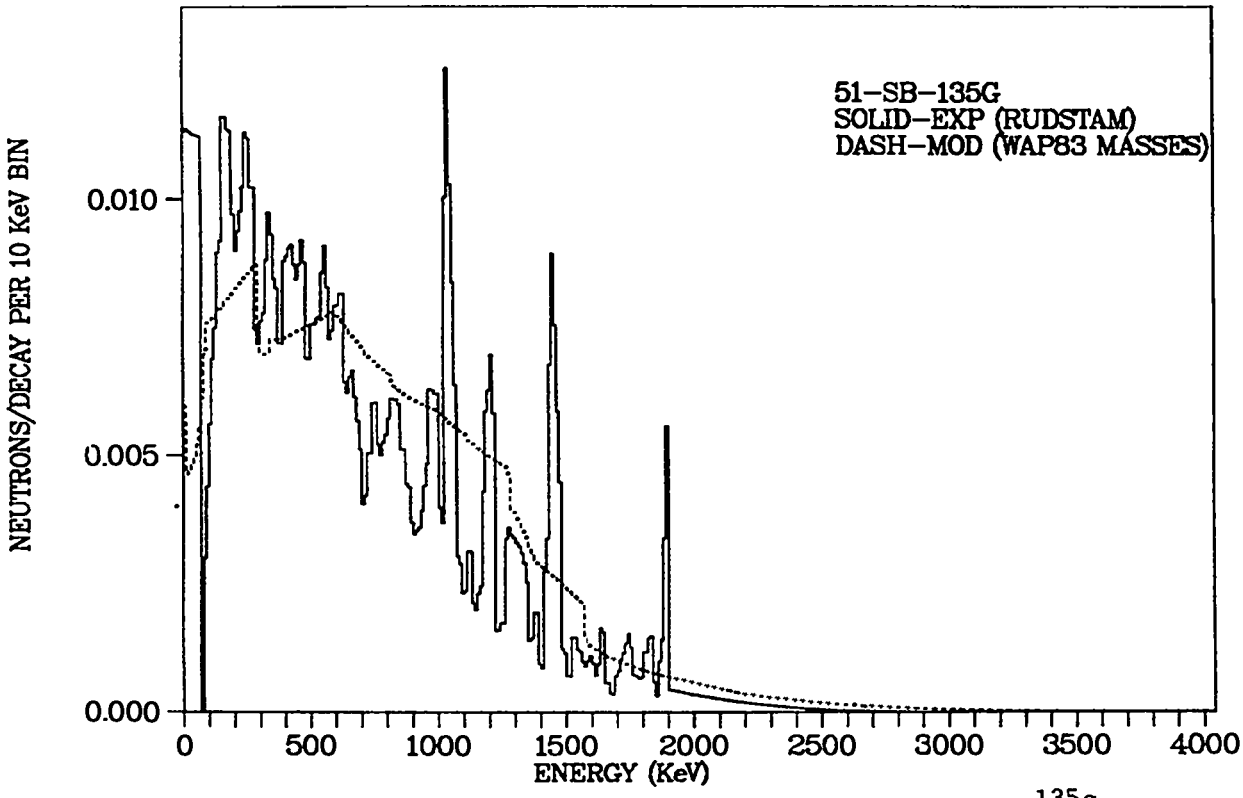

Fig. 64. Normalized delayed neutron spectra for nuclide ^{135g}Sb.

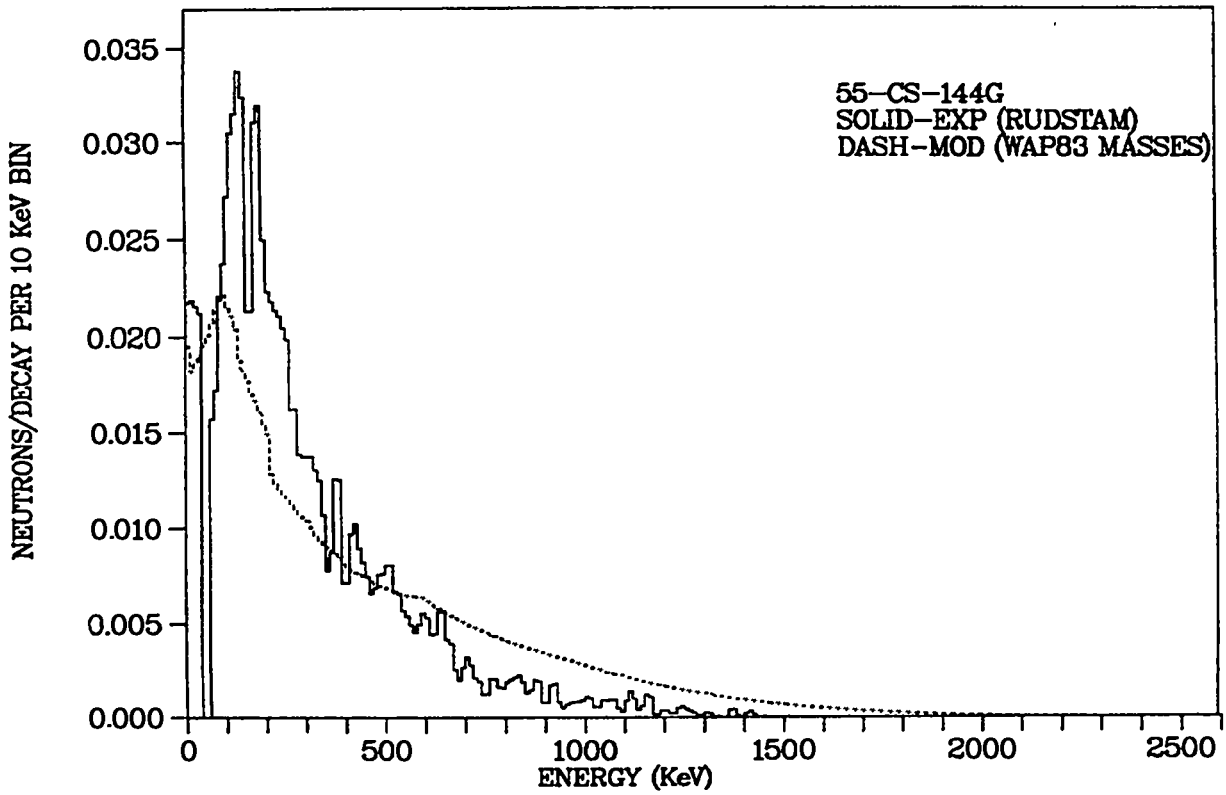

Fig. 65. Normalized delayed neutron spectra for nuclide ^{144g}Cs.

be based on a small range near the end of the measurements. The point of addition is subjective, based on uncertainties and plots of the measurement. Twenty of the thirty measured spectra were extended; the point of addition and the fractional reduction are listed in Table XI.

TABLE XI

MEASURED PRECURSORS HAVING EXTENDED SPECTRA

Nuclide	Joined KeV	Frac.	Nuclide	Joined KeV	Frac.
31Ga 80G	1060	0.6427	31Ga 81G	1690	0.7759
33As 85G	2520	0.4662	35Br 89G	2290	0.5339
35Br 90G	2830	0.5423	35Br 91G	2940	0.3022
35Br 92G	3000	0.8393	37Rb 93G	1230	0.2514
37Rb 94G	2460	0.9625	37Rb 95G	1210	0.1412
37Rb 96G	2220	0.1060	37Rb 97G	2110	0.0342
37Rb 98G	2470	0.0965	50Sn134G	1620	0.5222
51Sb135G	1910	0.6393	53I 139G	1610	0.3473
53I 140G	1760	0.2566	53I 141G	1680	0.4255
55Cs143G	1260	0.3210	55Cs144G	1430	0.1771

Because of the recent interest in higher energies, it has been necessary to recalculate the spectra for 70 unmeasured nuclides. Our previous results, noted in Ref. 108, extended only to 5 MeV or less. Based on comparisons such as those in Figs. 62-65, we have used Q_β and S_n values derived from Wapstra mass tables,*[113] where available, and from Möller-Nix otherwise.[114]

Presently, we are adding low energy spectra, having been measured recently with a hydrogen recoil spectrometer[115] and other data measured by Reeder[116] and Kratz.[117] In addition, we anticipate reevaluating the Pn values and incorporating some recent measurements by Reeder.[118]

4. Summation Calculations.

Before any of the improvements in fission product yields, Pn and spectra data were made, it was shown in Ref. 108 that summation code calculations could greatly extend the low- and high-energy range of aggregate, evaluated spectra, and they could increase the number of fissionable nuclides having evaluated spectra. The earlier work was based on interest in improvements in equilibrium spectra. Time-dependent, aggregate spectra following a fission pulse are even more difficult to measure and require even more accurate precursor data, especially fission yields, for use in summation codes.

*Wapstra 81 refers to a preliminary 1981 set of masses distributed for comment but not published.

We have used a modified version of the CINDER-10 code[119] for computing aggregate pulse spectra. Prior to the extensions of spectra noted above, a typical pulse result is shown in Fig. 66. For high-energy neutrons, a better representation is given in Fig. 67, where the fraction of neutrons above the abscissa energy is plotted. The rapid drop between 2-3 MeV results from the lack of any precursor spectra above 3 MeV. This, in fact, was the motivation for the extensions. Figure 68 compares the new results at 20 seconds after a pulse with the old. Here 20 measured spectra were extended, but no other changes were made.

The values labelled time 0 on Figs. 66-68 should actually apply at $\sim 10^{-4}$ s. There could be neutrons emitted from the highly excited fission fragments during the first few microseconds following fission.

Similar results have been computed for other fuels.

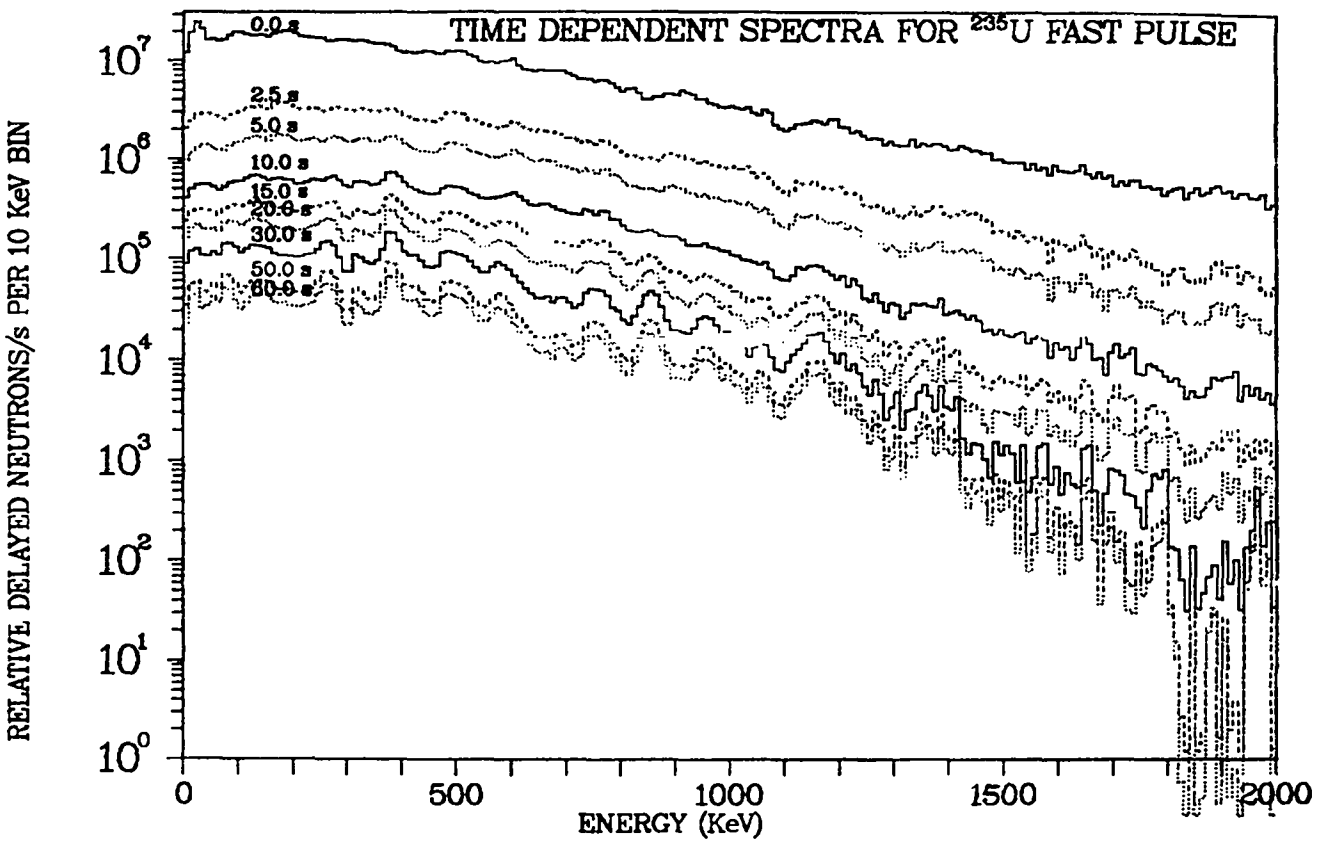

Fig. 66. ^{235}U delayed neutron spectra (1.3E + 16 fission pulse).

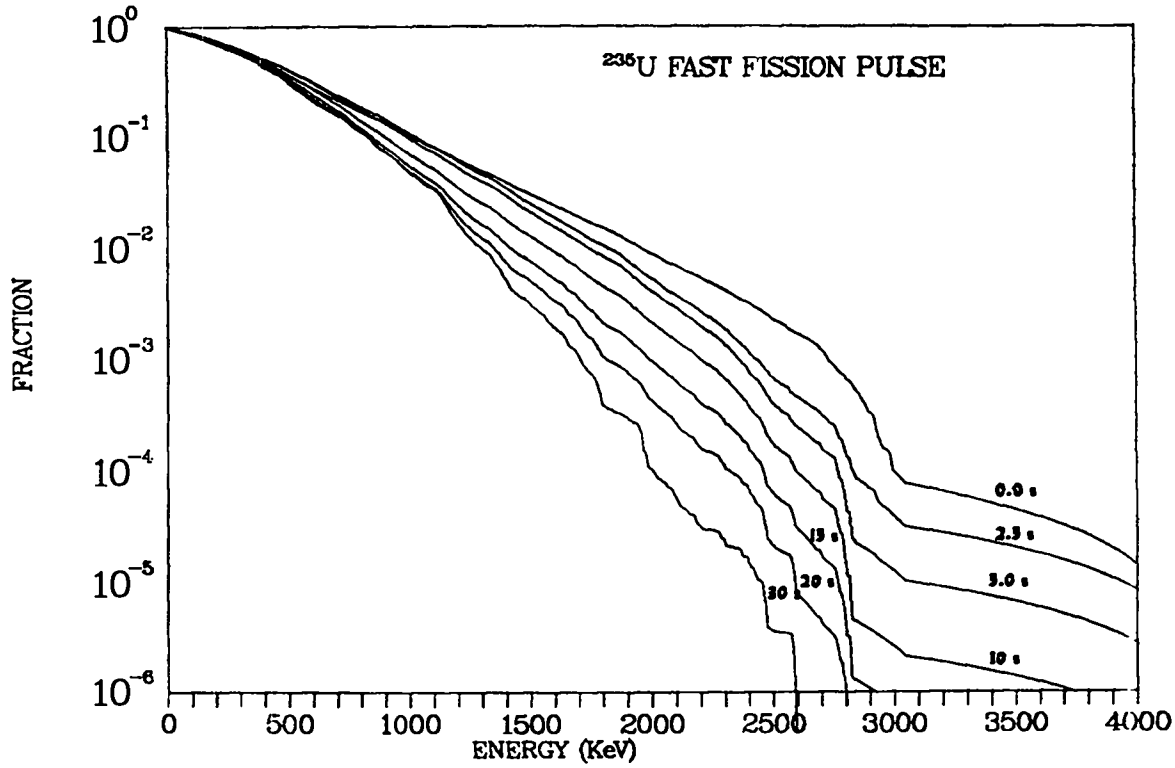

Fig. 67. Fraction of total delayed neutrons above abscissa energy (based on pulse spectra).

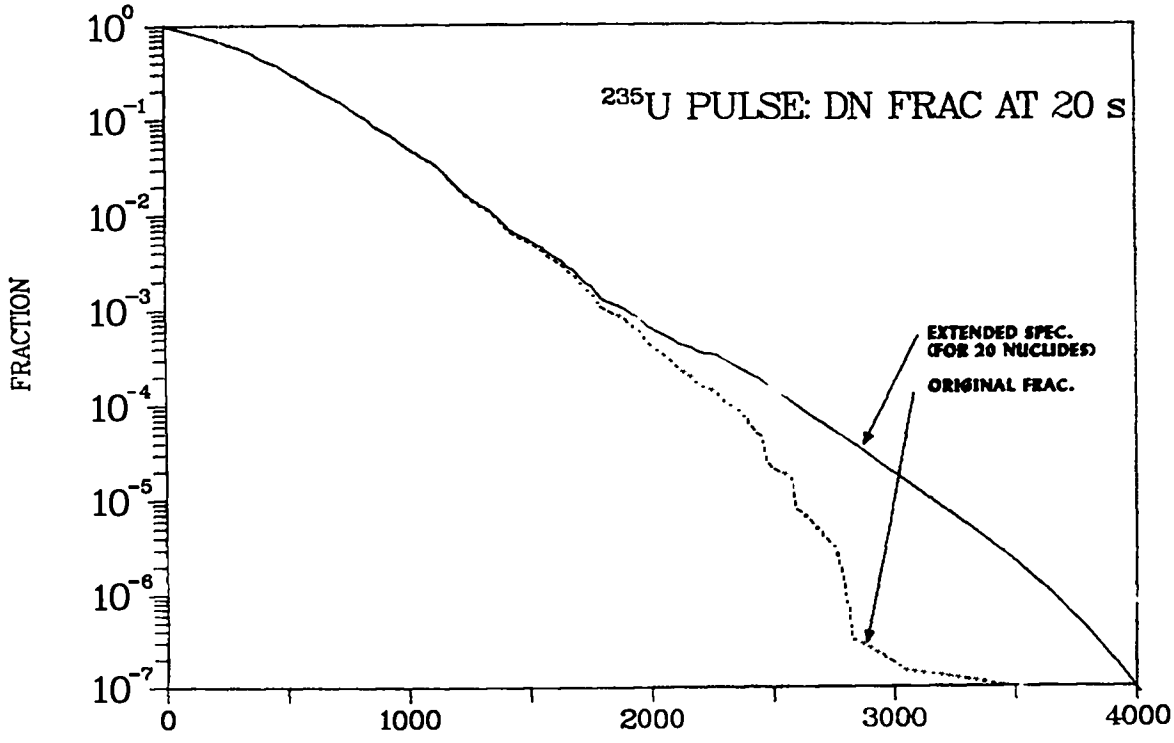

Fig. 68. ^{235}U fraction of total delayed neutrons above abscissa energy.

5. Confirmation of Spectra

The high-energy augmentation of 20 measured spectra is very evident in Fig. 68, but it has very little effect on the measured portion of the spectra. For some applications, the energies above ~ 2 MeV are important and we need an independent confirmation of at least the order of magnitude of these results, short of an aggregate experiment.

A. Sierk[120] used a completely statistical and evaporation model to get approximate spectra. Mass chain yields and their distribution vs Z were assumed to be described by a Gaussian. The ft value was fit to an approximation for halflives (separately for odd-odd and odd-even nuclei). The rate of beta decay to excited states was approximated and the emission spectrum was assumed to be a simple evaporation model. In actual calculations, true halflives were applied where they were known, and the same sources of mass values employed in the BETA code were used.

Considering the number of approximations, it was not clear that this study could confirm the more detailed summation calculations, seen in Fig. 68; however, as demonstrated in Fig. 69, the results compare very well, differing by only a factor of three in the integral value at 5 s, the only time compared. This is within the estimated factor of five uncertainty in the statistical calculation.

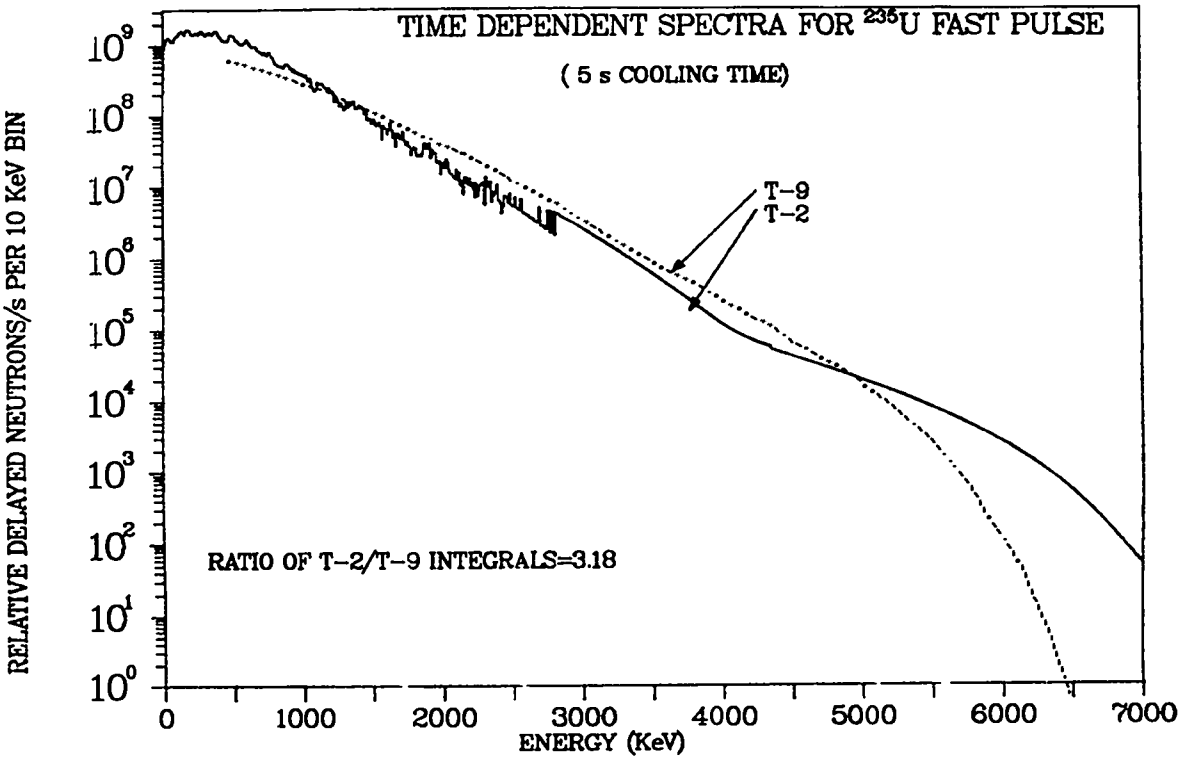

Fig. 69. ^{235}U delayed neutron spectra.

B. ENDF/B-VI Yields (M. B. C. Butler and T. R. England)

In a preliminary ENDF-VI evaluation,[105] ENDF-VM fission product yields were modified by extending the yields along mass chains. For the 50 yield sets currently in ENDF-VM, the pairing model[121] was used to extend yields on the neutron rich side of the mass chains 66-172. The influence of pairing on the distribution of the yields was also taken into account by the use of both neutron and proton pairing factors in the yield extension. This process resulted in increasing the number of yields per set from an average of ~ 1100 to an average of ~ 1200. The new yield sets were tested by executing the OKLA code, which employs various conservation principles in the integral testing of yield data. In terms of satisfying these basic conservation laws, the 50 extended yield sets appear satisfactory.

With the exception of modifying the pairing used for ^{238}U fast fission, this effort was primarily directed toward getting a complete set of yields in an ENDF/B format.

C. Beta and Gamma Fission-Product Decay Energy Comparisons with Recent Japanese Measurements (Pulse) [T. R. England, R. J. LaBauve, W. B. Wilson, and M. Akiyama (University of Tokyo)]

For ^{238}U and ^{232}Th fast fission, we have made several comparisons with the recent Japanese measurements. Figures 70-73 illustrate these comparisons.

When the Japanese Nuclear Data Committee (JNDC) 1.5 nuclide decay energies replace those in ENDF/B-V, the agreement is remarkably improved over use of only ENDF/B files. Also, the Japanese calculations using only their file (which uses ENDF/B-V yields) are nearly identical to those using ENDF/B-V + JNDC nuclide energies.

Similarly, we have seen a good degree of improvement when comparing ENDF/B-V + JNDC energies with US measurements following ^{235}U and ^{239}Pu thermal fission.

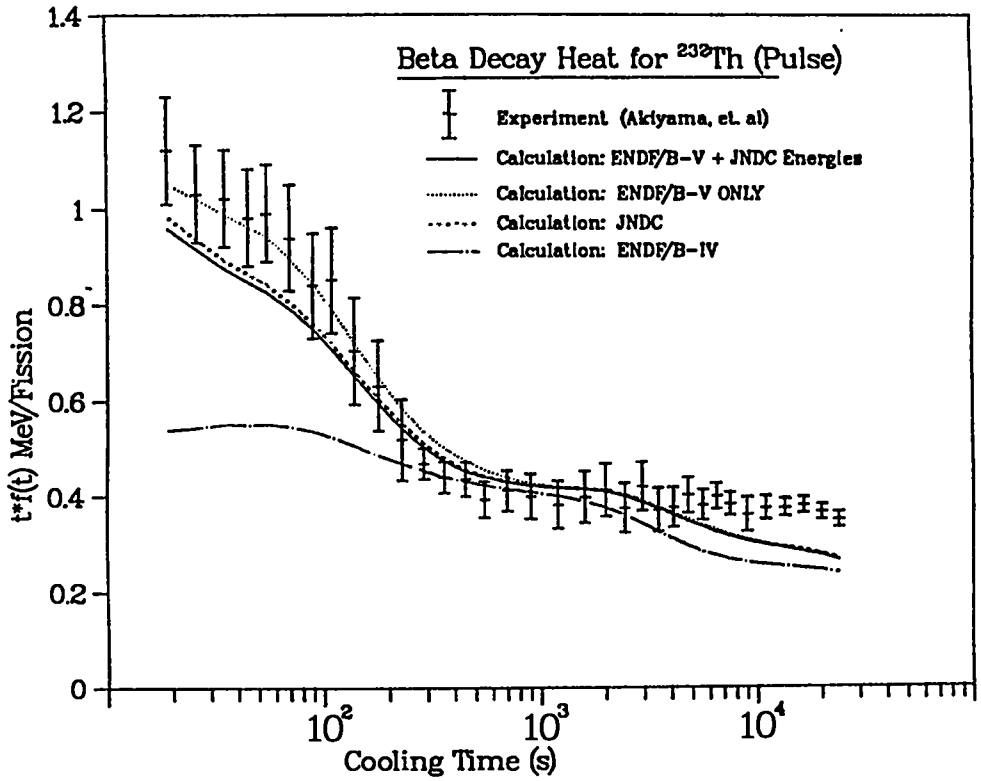

Fig. 70. Comparison of Japanese β-decay heat for ^{232}Th (pulse) with calculations.

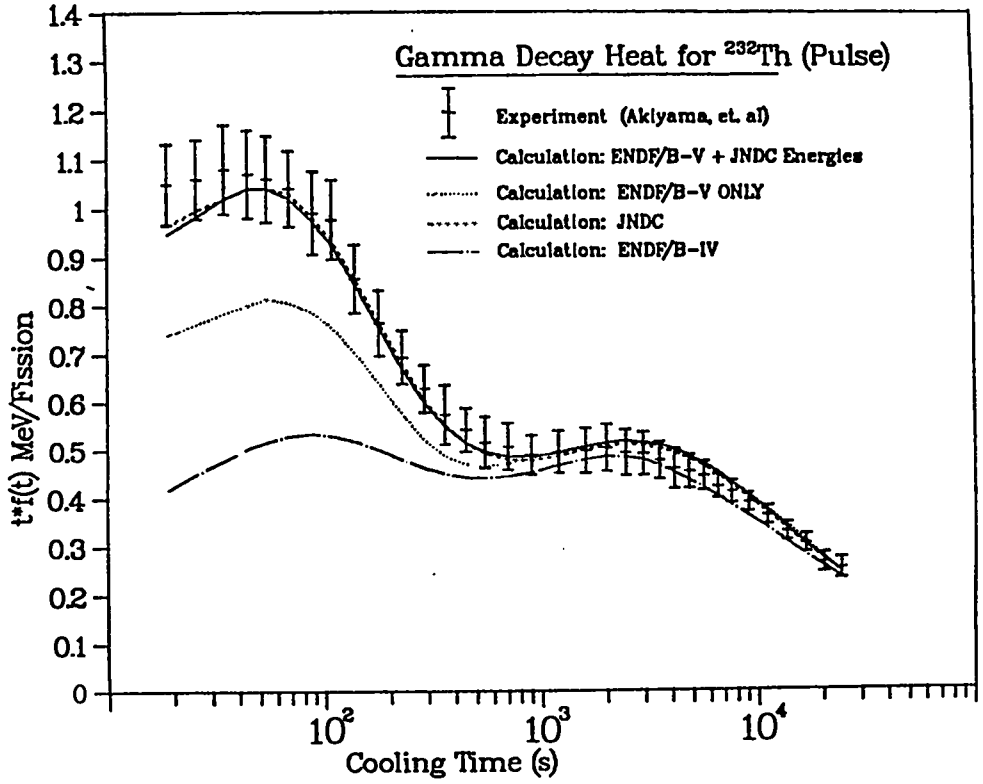

Fig. 71. Comparison of Japanese γ-decay heat for ^{232}Th (pulse) with calculations.

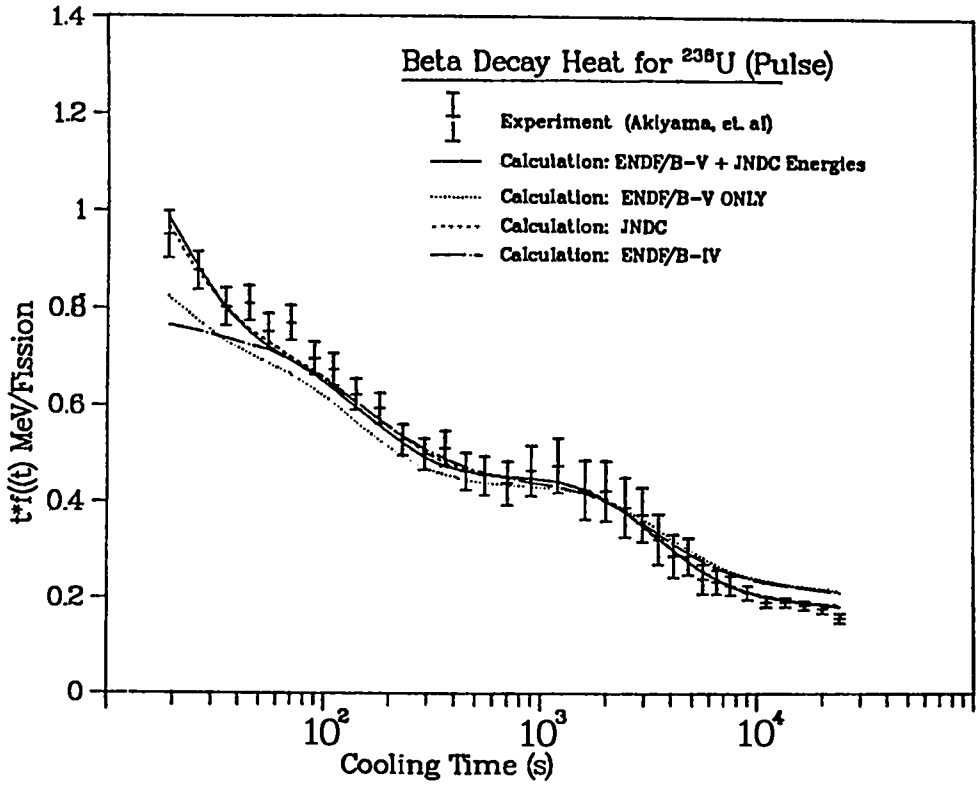

Fig. 72. Comparison of Japanese β-decay heat for ^{238}U (pulse) with calculations.

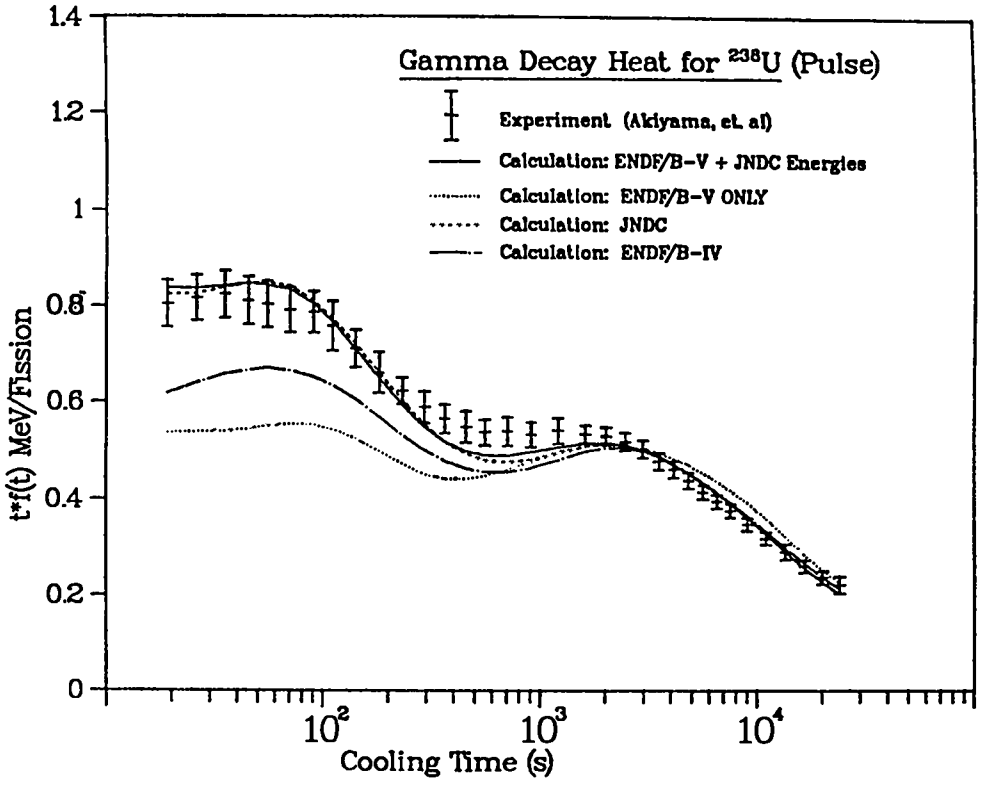

Fig. 73. Comparison of Japanese γ-decay heat for ^{238}U (pulse) with calculations.

D. Evaluation of $^{10,11}B(\alpha,n)$ Cross Sections [W. B. Wilson and R. T. Perry (Texas A&M University)]

The (α,n) cross section, measured by Walker[122] for ^{nat}B below 5 MeV, has been used in SOURCES[123] code calculations of thick target $B(\alpha,n)$ yields,[124] producing values about 40% higher than yields measured for 3.5-5.5 MeV α's on boron.[125,126,127] Calculations of (α,n) neutron spectra for commercial high-level waste problems[128] with B require individual ^{10}B and ^{11}B cross sections extending above 6 MeV, as well as product level branching fractions. The available $^{10,11,nat}B(\alpha,n)$ cross-section data have been accumulated as follows:

(a) the $^{nat}B(\alpha,n)$ data of Walker;[122]

(b) cross sections and product nuclide level branching fractions calculated with the GNASH code;[8]

(c) the $^{11}B(\alpha,n_0)$ cross sections calculated from the $^{14}N(n,\alpha_0)$ reciprocal reaction cross section of ENDF/B-V[85] from the evaluation by Young and Foster;[129]

(d) the $^{10,11}B(\alpha,n)$ cross sections stripped from the thick target yield data of Bair and del Campo[125] using the α stopping cross-section functions of Ziegler.[130]

Cross sections obtained from these sources, as shown in Fig. 74, appear to be divided into a group of higher-magnitude data containing (a), (b), and (c) above, and the lower-magnitude stripped cross sections of (d).

The following observations may be made on these data:

(a) Yields calculated with the Walker data are higher than measured yields.

(b) The GNASH calculations should be expected to produce relatively accurate partial cross-section ratios $\sigma(\alpha,n_\ell)/\sigma(\alpha,n)$ (i.e., product level ℓ branchings) but less accurate cross-section magnitudes when used to describe light nuclei.

(c) The $^{14}N(n,\alpha_0)$ cross section used in the reciprocal reaction calculation is an evaluation of widely varying data and closely follows the highest values.[129]

(d) Yields calculated with the cross sections stripped from the $^{10,11}B$ (α,n) yields of Bair and del Campo agree well with all measured $^{10,11,nat}B(\alpha,n)$ yields, as shown in Table XII.

The cross-section data stripped from the Bair and del Campo yields have been included in the SOURCES data library, as have level branching fractions calculated from partial cross sections produced in the GNASH calculations.

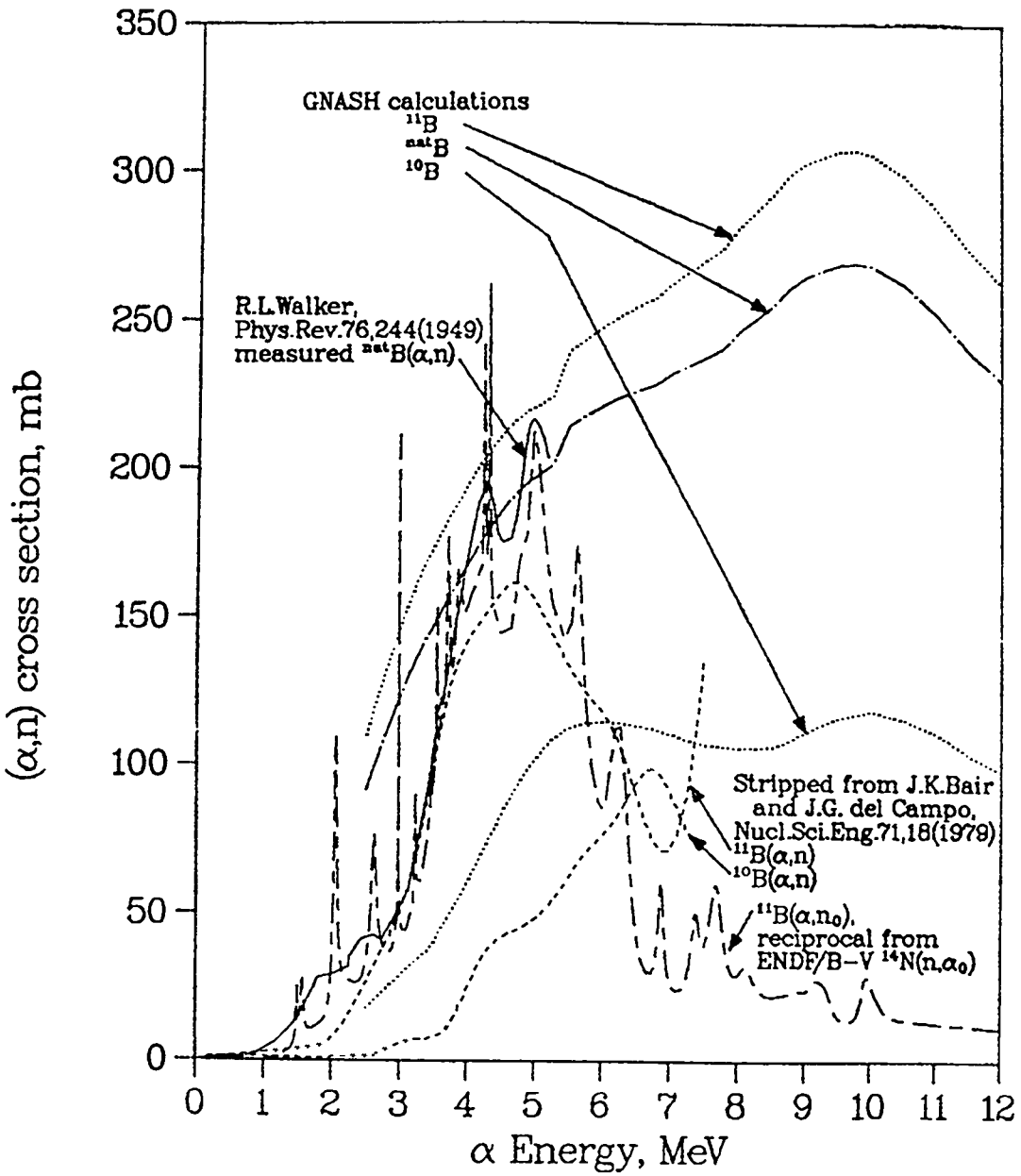

Fig. 74. Boron (α,n) cross-section data.

TABLE XII

COMPARISON OF MEASURED (α,n) THICK TARGET YIELDS AND VALUES CALCULATED WITH CROSS SECTIONS STRIPPED FROM YIELDS MEASURED BY BAIR AND DEL CAMPO[a]

	(alpha,n) thick target yields, n/ 1.e+6 alphas								
	boron-10			boron-11			natural boron		
E, MeV	Meas	Calc	%diff	Meas	Calc	%diff	Meas	Calc	%diff
3.5	0.331	0.361	+ 9.1	3.803	3.456	- 9.1	3.150	2.840	- 9.8
4.0	0.758	0.786	+ 3.7	7.618	7.254	- 4.8	6.238	5.967	- 4.3
4.5	1.924	1.948	+ 1.2	12.64	12.26	- 3.0	10.63	10.21	- 4.0
5.0	3.552	3.574	+ 0.6	18.43	18.04	- 2.1	15.64	15.16	- 3.1
5.3		4.762			21.47		[b]19.6	18.15	- 7.4
							[c]21.0	18.15	-13.6
5.5	5.674	5.696	+ 0.4	24.05	23.66	- 1.6	20.59	20.09	- 2.4
6.0	8.578	8.604	+ 0.3	29.24	28.86	- 1.3	25.35	24.83	- 2.1
6.5	12.29	12.32	+ 0.2	33.92	33.55	- 1.1	29.85	29.32	- 1.8
7.0	16.78	16.82	+ 0.2	37.52	37.16	- 1.0	33.62	33.11	- 1.5

[a]All measured yields are from J. K. Bair and J. G. del Campo,[125] unless otherwise noted.
[b]See G. V. Gorshkov, V. A. Zyabkin, and O. S. Tsvetkov, Ref. 126.
[c]See J. H. Roberts, Ref. 127.

IV. APPLICATIONS

A. Initial Loading Calculations for the RI SAFR Design [(R. J. LaBauve, D. C. George, and E. Specht (Rockwell International)]

As part of the US Department of Energy's directive that the national laboratories provide assistance to private companies in their fast reactor research, development, and design, Los Alamos National Laboratory has cooperated with Rockwell International (RI) by performing a series of calculations for the initial loading of the RI design for SAFR,[131] a heterogeneous fast breeder reactor. This report gives results of calculations completed in FY1985 and indicates additional work needed to assure a safe start-up of the reactor.

The basic one-sixth core, hexagonal-Z model used in our calculations was taken from data sent to us by Argonne National Laboratory (ANL) for the oxide version of SAFR; ANL is assisting RI in the SAFR core design. Due to the fact that this model is set up for depletion calculations, it contains more detail than we feel was needed for our initial start-up calculations. Consequently, we simplified this Hex-Z model for our application. Our R-Z model was derived from our Hex-Z model by keeping volumes (actually, areas) equal in going from hexagonal to annular regions. The R-Z model is shown in Fig. 75, and the Z-plane at

mid-core (Z = 132.1 cm) of the Hex-Z model is shown in Fig. 76. These models were used in the preliminary calculations described below.

The nuclear cross-section data we used were derived from ENDF/B-V[132] data processed by NJOY[100] into the 80-group MATXS6[133] fine-group library. The TRANSX[133] code was used to produce the 12-group library in the ISOTXS[134] format required by DIF3D,[135] the code used for two-dimensional R-Z and three-dimensional Hex-Z calculations. Initially, TRANSX was run to generate 80-group cross sections for each of nine different compositions used in the models. Table XIII gives the correspondence between TRANSX regions and the zones shown in the figure for the R-Z model. A DIF3D 80-group run was made using the R-Z model to generate 80-group fluxes for subsequent use in a second TRANSX calculation to collapse to 12-groups. The 80- and 12-group energy structures are given in Table XIV. The last TRANSX step produced 12-group homogenized cross sections for the nine compositions and also microscopic cross sections for what are referred to as "IB," "OC," and "RR" materials, using Zone 1 (IB01) and Zone 3 (OC01 and OC02) fluxes to collapse the cross sections for the "IB" and "OC" materials, respectively; Zone 9 (RR01) fluxes were used for all "RR" materials except ^{10}B, ^{11}B, and C for which Zone 8 (CRI1 and CRI2) fluxes were used.

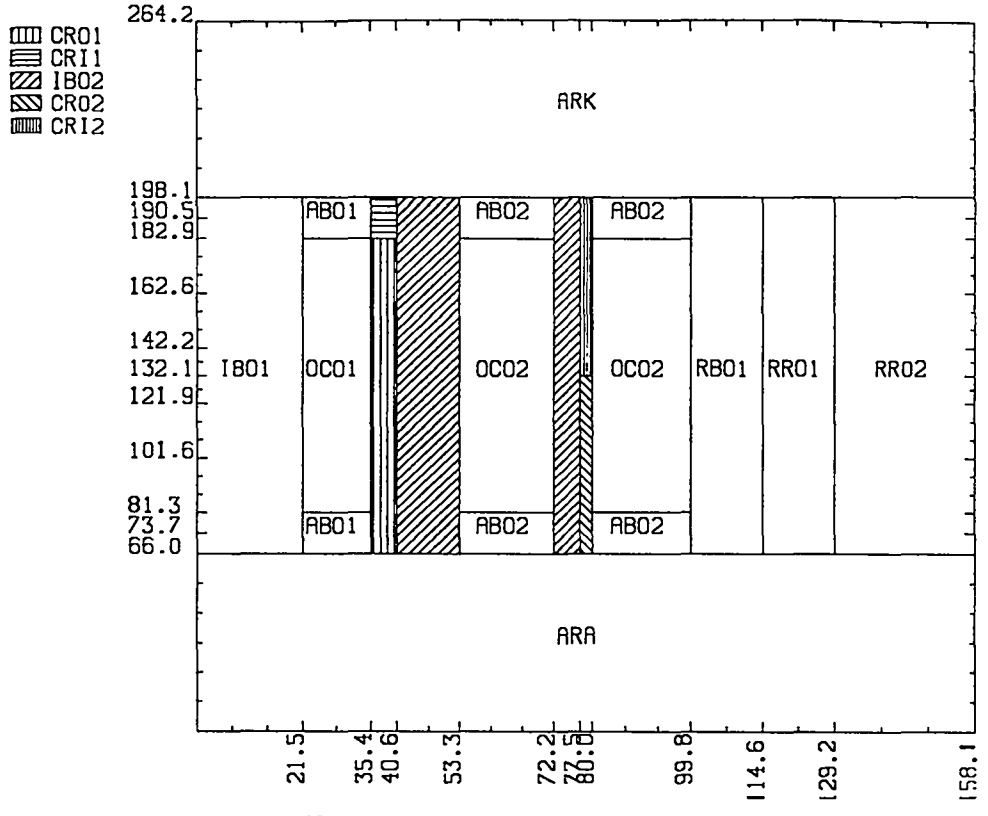

Fig. 75. R-Z model of SAFR.

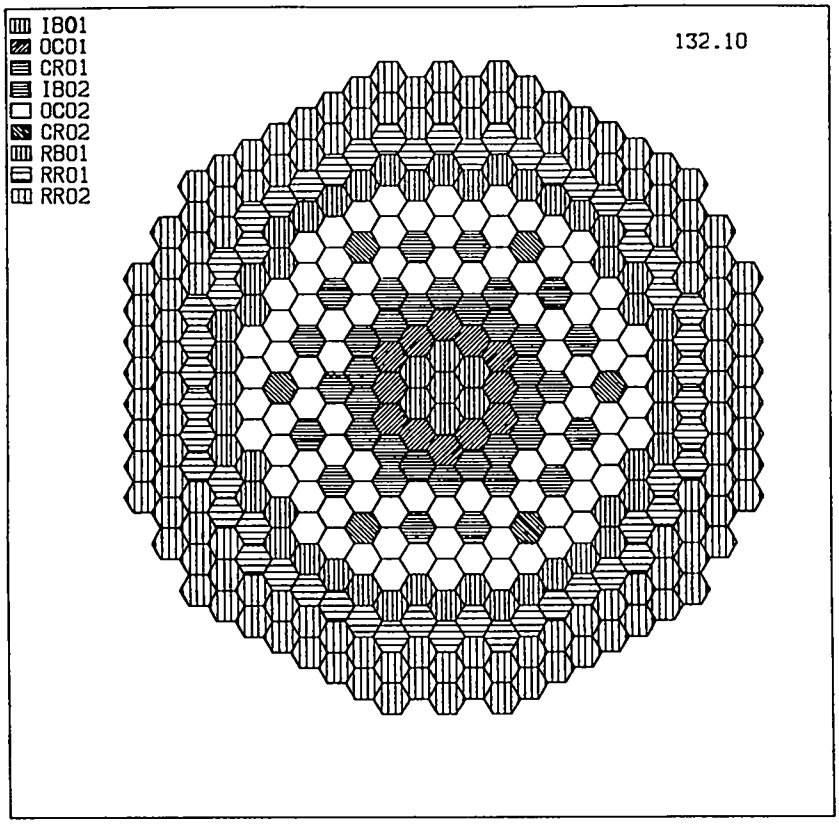

Fig. 76. Hexagonal plane at 132.1 m--mid core.

TABLE XIII

REGION CORRESPONDENCE FOR CROSS-SECTION COLLAPSE

DIF3D Region Designation	TRANSX Region Designation	R-Z Zone No.	Hex-Z Zone No.
ARA-Lower Axial Reflector	ARSC	9	6
ARK-Upper Axial Reflector	ARSC	9	6
IB01-Inner Blanket #1	IBSC	1	1
IB02-Inner Blanket #2	IBSC	1	2
OC01-Outer Core #1	OCSC	3	3
OC02-Outer Core #2	OCSC	3	3
CR01-Control Rods #1 (out)	CROSC	3	7
CR02-Control Rods #2 (out)	CROSC	3	7
CRI1-Control Rods #1 (in)	CRISC	8	8
CRI2-Control Rods #2 (in)	CRISC	8	8
AB01-Axial Blanket #1	ABSC	1	4
AB02-Axial Blanket #2	ABSC	1	4
RB01-Radial Blanket #1	RBSC	1	5
RR01-Radial Reflector #1	RR1SC	9	9
RR02-Radial Reflector #2	RR2SC	9	10

TABLE XIV

BOUNDARIES FOR 80-GROUP STRUCTURE

Group	Energy(eV)	Group	Energy(eV)
01	$2.0000X10^{7}$[a]	41	$1.5034X10^{4}$[a]
02	$1.6905X10^{7}$	42	$1.3268X10^{4}$
03	$1.4918X10^{7}$	43	$1.1709X10^{4}$
04	$1.3499X10^{7}$	44	$1.0333X10^{4}$
05	$1.1912X10^{7}$	45	$9.1188X10^{3}$
06	$1.0000X10^{7}$	46	$8.0473X10^{3}$
07	$7.7880X10^{6}$	47	$7.1017X10^{3}$
08	$6.0653X10^{6}$	48	$6.2673X10^{3}$
09	$4.7237X10^{6}$	49	$5.5308X10^{3}$[a]
10	$3.6788X10^{6}$[a]	50	$4.8810X10^{3}$
11	$2.8650X10^{6}$	51	$4.3074X10^{3}$
12	$2.2313X10^{6}$	52	$3.8013X10^{3}$
13	$1.7377X10^{6}$	53	$3.3546X10^{3}$
14	$1.3534X10^{6}$[a]	54	$2.9604X10^{3}$
15	$1.1943X10^{6}$	55	$2.6126X10^{3}$
16	$1.0540X10^{6}$	56	$2.3056X10^{3}$
17	$9.3014X10^{5}$	57	$2.0347X10^{3}$[a]
18	$8.2085X10^{5}$	58	$1.7956X10^{3}$
19	$7.2440X10^{5}$	59	$1.5846X10^{3}$
20	$6.3928X10^{5}$	60	$1.3984X10^{3}$
21	$5.6416X10^{5}$	61	$1.2341X10^{3}$
22	$4.9787X10^{5}$[a]	62	$1.0891X10^{3}$
23	$4.3937X10^{5}$	63	$9.6112X10^{2}$
24	$3.8774X10^{5}$	64	$7.4852X10^{2}$[a]
25	$3.0197X10^{5}$[a]	65	$5.8295X10^{2}$
26	$2.3518X10^{5}$	66	$4.5400X10^{2}$
27	$1.8316X10^{5}$	67	$3.5358X10^{2}$
28	$1.4264X10^{5}$	68	$2.7536X10^{2}$[a]
29	$1.1109X10^{5}$[a]	69	$1.6702X10^{2}$
30	$8.6517X10^{4}$	70	$1.0130X10^{2}$
31	$6.7379X10^{4}$	71	$6.1442X10^{1}$
32	$5.2475X10^{4}$	72	$3.7267X10^{1}$
33	$4.0868X10^{4}$[a]	73	$2.2603X10^{1}$
34	$3.1828X10^{4}$	74	$1.3710X10^{1}$
35	$2.8088X10^{4}$	75	8.3153
36	$2.6058X10^{4}$	76	5.0435
37	$2.4788X10^{4}$	77	3.0590
38	$2.1875X10^{4}$	78	1.1254
39	$1.9305X10^{4}$	79	$4.1399X10^{-1}$
40	$1.7036X10^{4}$	80	$1.5230X10^{-1}$
	Emin $1.3888X10^{-4}$[a]		

[a]12-group boundaries.

A series of preliminary DIF3D problems was run to study effects of changes in mesh size, cross-section group structure, and geometry, and also to determine control rod worth. Results are summarized in Table XV. Note from the table that for 80-group, R-Z geometry, going from a 14-cm core mesh spacing to a 5-cm spacing resulted in only a 4-milli-k change, so we compromised at a 7-cm mesh for the base 80-group, R-Z problem from which we derived the fluxes input to TRANSX. Also, surprisingly, only a 2-milli-k difference is observed between R-Z and Hex-Z geometry; whereas a 2-milli-k difference is also observed between the 12- and 80-group R-Z problems. The latter is probably due to the fact that we collapsed using fluxes from only one blanket and one core region (the inner

ones), as indicated in Table XIV. Finally, note the negligible difference in going to more planes for the Hex-Z problems. We did, however, use the 22-plane model for the loading sequences described below.

TABLE XV

RESULTS OF PRELIMINARY DIF3D PROBLEMS

Geometry	No. of Groups	CR-2 Position	K_{eff}	Run Time	Remark
R-Z	80	out	1.0279	60. s	"14-cm" mesh
R-Z	80	out	1.0241	120. s	"5-cm" mesh
R-Z	80	mid-way	0.9833	85. s	"7-cm" mesh, base problem
R-Z	12	mid-way	0.9850	10. s	Isotopic Xsec used
Hex-Z	12	mid-way	0.9873	54. s	12 Z-planes
Hex-Z	12	out	1.0179	54. s	12 Z-planes
Hex-Z	12	mid-way	0.9871	110. s	22 Z-planes

Alterations were made in the model to simulate several initial loading configurations and also to include detector locations. Low-level flux detectors were assumed to be located in Ring 12 and a detector and/or source was assumed to be located at the center (Ring 1). The reactor was assumed to be initially loaded symmetrically from center out, and the assemblies in the rings not yet loaded were assumed to consist of 95% Na and 5% HT9.

The altered R-Z and Hex-Z models are shown in Figs. 77 and 78, respectively. Note that the sizes of the source and detector regions are exaggerated to show up the figures. The compositions of regions RB01, RR01, and RR02, shown in Fig. 78, were changed to 95% Na and 5% HT9 in the DIF3D problems. In Fig. 78, for the hexagonal plane at mid-core (Z = 132.1 cm), Rings 1-6 are shown to be loaded normally, but Rings 7 and 8 are shown to be loaded with RB01, 5% HT9, and 95% Na in this case.

Results of this series of DIF3D calculations are shown in Table XVI. The response of the detectors was simulated by calculating $^{10}B(n,\alpha)$ and $^{235}U(n,f)$ reaction rates. The reaction rates are in units of reactions/sec-nucleus for an assumed power of 15 watts. Note that the reaction rates at the LLFDs are down by a factor of 10^3 from the central value, but would be down by a factor of 10^5 if the radial blanket and radial reflectors were in place during loading. Also given in Table XVI are values of k_{eff} for the various loading configurations and "multiplication" values based on a relative k_{eff} obtained for the fully loaded reactor with CR-1 withdrawn and CR-2 positioned at mid-core (see Table XV).

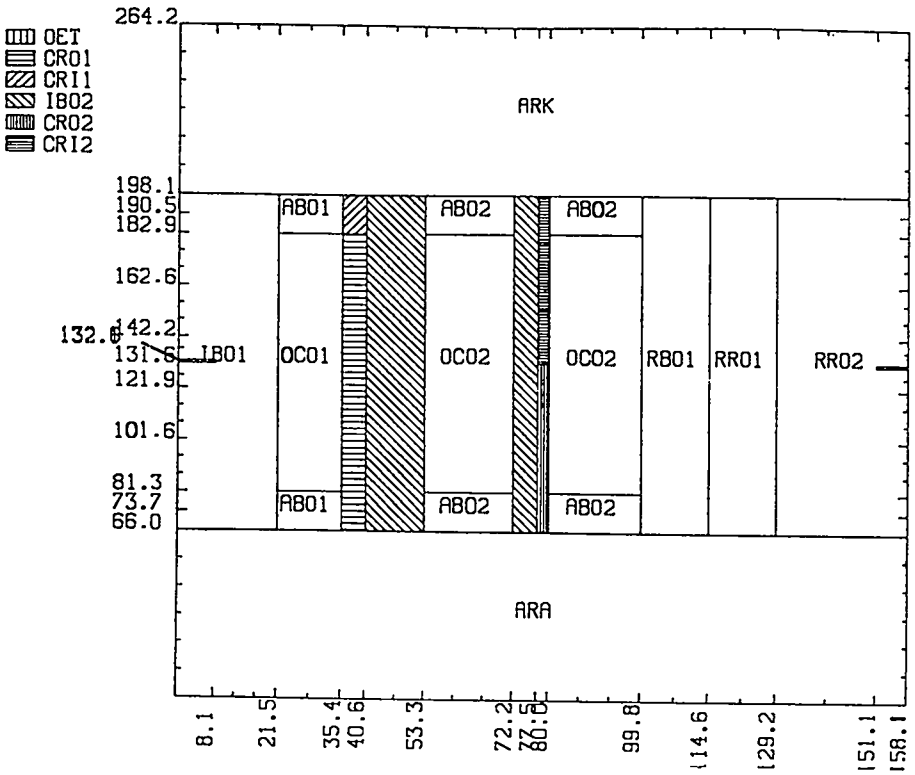

Fig. 77. SAFR R-Z model for loading sequence.

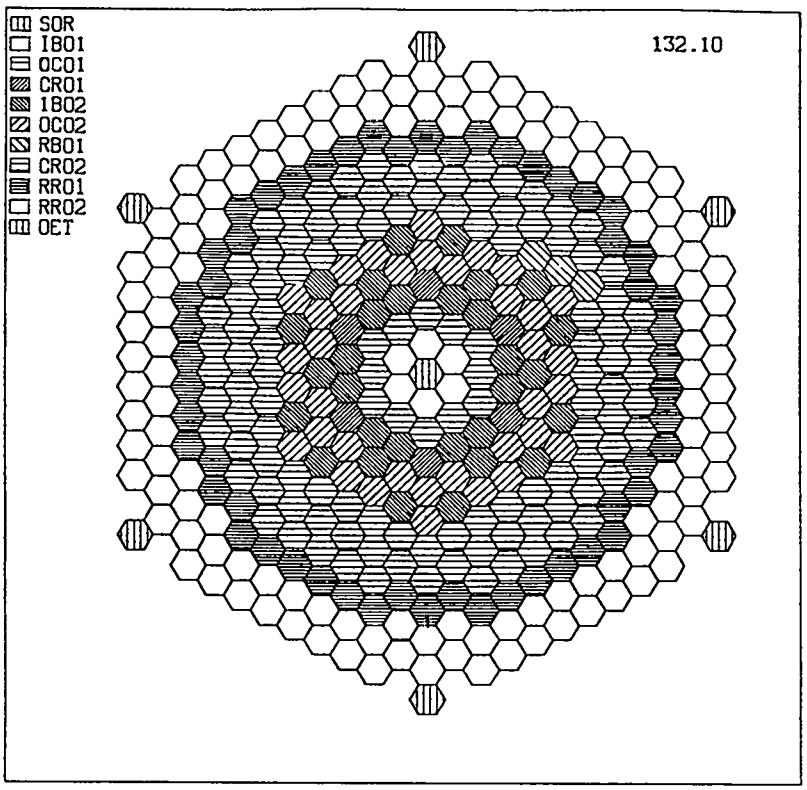

Fig. 78. Mid-core plane (Z = 132.10 cm) of Hex-Z model with Rings 1-6 loaded normally and 95% Na, 5% HT9 in other rings.

Although the calculations described in this report will be very useful in planning SAFR initial start-up, they are incomplete and need to be extended. Note in Table XVI the rather large changes in k_{eff} from problem to problem caused by loading entire rings and/or fully withdrawing/inserting the control assembly blanks. Full core problems need to be run to observe the changes caused by incremental positioning of the control rods and by adding one or two fuel assemblies at a time as criticality is approached. Also, because eigenvalue calculations for k_{eff} less than about 0.8 are not very useful, the problems shown in the table begin with normal loading up through Ring 5. Calculations for loadings up to this point should also be done, but these must be performed with a source located near the center.

TABLE XVI

RESULTS OF FIVE LOADING CONFIGURATIONS

Reactor Config.	Position of CR-1	CR-2	K_{eff}	Detector Reaction Rates $^{10}B(n,\alpha)$	$^{235}U(n,f)$	Reaction Rate Ratios $^{10}B(n,\alpha)$	$^{235}U(n,f)$	"M"
1	out	out	.7894	$2.9X10^{-18}$	$1.4X10^{-18}$	$5.9X10^{-4}$	$4.8X10^{-4}$	4
2	out	out	.8645	$2.4X10^{-18}$	$1.2X10^{-18}$	$8.1X10^{-4}$	$6.7X10^{-4}$	7
2	in	out	.7547	$2.6X10^{-18}$	$1.3X10^{-18}$	$7.7X10^{-4}$	$6.4X10^{-4}$	3
3	in	in	.8144	$1.8X10^{-18}$	$9.0X10^{-19}$	$1.0X10^{-3}$	$9.1X10^{-4}$	5
3	out	out	.9415	$1.7X10^{-18}$	$8.7X10^{-19}$	$1.0X10^{-3}$	$9.1X10^{-4}$	21
4	in	out	.9337	$1.7X10^{-18}$	$8.6X10^{-19}$	$2.3X10^{-3}$	$2.1X10^{-3}$	17
4	out	out	.9957	-	-	-	-	-
4	in	in	.8670	$1.6X10^{-18}$	$8.4X10^{-19}$	$1.6X10^{-3}$	$1.4X10^{-3}$	7
5	in	in	.8941	$1.1X10^{-20}$	$6.1X10^{-21}$	$1.3X10^{-5}$	$1.3X10^{-5}$	10
4(R-Z)	in	in	.8692					

Reactor configuration descriptions:

1 Hex rings 1,2,3,4,5 loaded normally. In rings 6,7,8 fuel/axial blanket assemblies replaced with dummy assemblies with 5% HT9 and 95% Na. Radial blanket and radial reflectors were also replaced by 5% HT9 and 95% Na. IB's in ring 6.

2 Same as in 1, but fuel/axial blanket assemblies loaded in ring 6.

3 Same as in 1, but fuel/axial blanket assemblies loaded in rings 6 and 7.

4 Same as in 1, but fuel/axial blanket assemblies loaded in rings 6, 7, and 8.

5 Full core with radial blanket and reflectors 1 and 2 in place.

"M" = "multiplication" = $(K_{eff})/(K_{ref} - K_{eff})$, where K_{ref} = .9871 for reactor configuration #5 with CR-1 out and CR-2 midway.

Reaction rates are in reactions/sec-nucleus for a power of 15 watts.

Reaction rate ratios are value at detector/central value.

B. Calculational Support for MST-5 Isotopically Tailored Ceramics Irradiation Experiments (R. J. LaBauve)

In a cooperative project, Los Alamos National Laboratory and Oak Ridge National Laboratory are planning a series of experiments in which two isotopically tailored ceramics [Al_2O_3 and "sialon" ($Si_3Al_3O_3N_5$)] will be irradiated in the Oak Ridge High Flux Isotope Reactor (HFIR). These experiments may be considered to be a first step in a program to develop ceramics for applications in which the materials are exposed to high fluences of fusion neutrons. The purpose of the HFIR experiments is to simulate a typical fusion "first wall" spectrum, particularly to determine the gas-production/displacement-per-atom ratio in the irradiated samples. The isotopic content of the samples (e.g., concentration of ^{15}N in sialon) irradiated in HFIR will be varied to stimulate the irradiation of the ceramic in the first wall spectrum.

Our calculational support for this project consists essentially of modeling the experiments and predicting results based on calculations using the REAC code[136] and ENDF/B-V data.[132] Specifically, we calculate the isotopically tailored ceramic in the specimen in HFIR spectrum and compare results with those calculated for the non-tailored specimen in the first wall spectrum. To date we have identified several important reactions and have calculated the integral cross sections of these in the HFIR PTP (peripheral test position, near central plane) and STARFIRE first wall spectra. Results, shown in Table XVII, are further compared with earlier calculations made for the Oak Ridge Reactor (ORR). Graphical comparisons of the cross sections for three of the more important reactions with the PTP and first wall spectra are shown in Figs. 79-81.

C. T-2 Macintosh Computer Network (D. C. George)

The arrival of the Apple Laserwriter printer spurred development of the T-2 Network, linking the Apple MacIntosh computers via an Appletalk network. The Laserwriter can now be shared among all network members. The Laserwriter printer support software was installed on appropriate software including MacWrite, Microsoft Word and MacPaint. The Laserwriter's Times, Helvetica, Courier, and Symbol fonts and Paragon's Scientific and Cursive fonts were installed in the word processing applications. The generation of mathematical equations was investigated and procedures for generating very readable mathematical prose were developed.

TABLE XVII

SPECTRUM AVERAGE CROSS SECTIONS

Reaction	Threshold Energy (MeV)	ORR Spectrum Average (mb)	HFIR Spectrum Average (mb)	1st Wall Spect Ave. (mb)
$^{14}N(n,p)$	0.0	35.8	439.1	52.99
$^{14}N(n,d)$	5.72	0.367	0.824	6.56
$^{14}N(n,t)$	4.32	1.02	0.173	4.91
$^{14}N(n,\alpha)$	0.17	96.5	17.38	33.05
$^{16}O(n,\alpha)$	2.67	11.0	1.70	21.81
$^{17}O(n,\alpha)$	0.0	105.	77.27	81.14
$^{27}Al(n,p)$	2.09	4.94	0.805	13.52
$^{27}Al(n,\alpha)$	4.19	0.75	0.142	19.72
$^{Nat}Si(n,p)$	4.01	8.07	1.399	39.02
$^{Nat}Si(n,\alpha)$	2.75	3.46	0.624	27.91

Note: ORR and HFIR/STARFIRE 1st Wall differences not due to spectrum differences only. ORR calculations reported previously used ENDF/B-IV data, whereas ENDF/B-V was used in the HFIR and 1st Wall calculations.

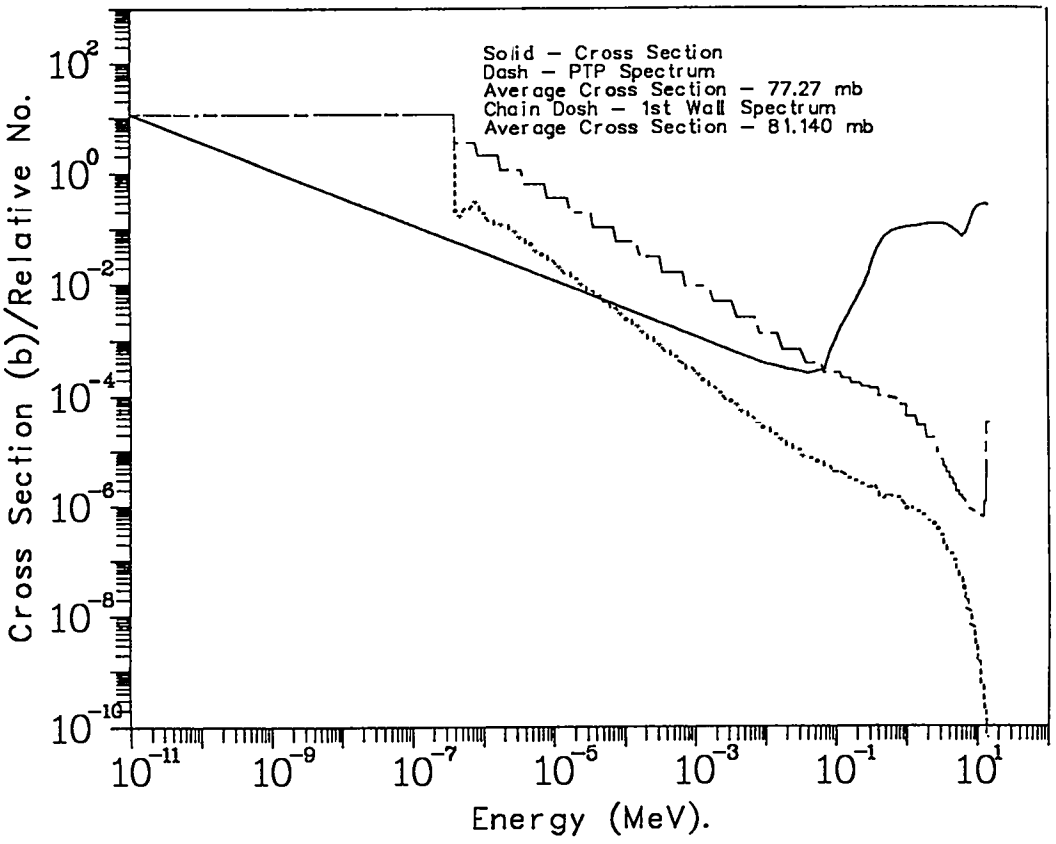

Fig. 79. Cross section for $^{170}O(n,\alpha)$ compared with the HFIR PTP and STARFIRE first wall spectra.

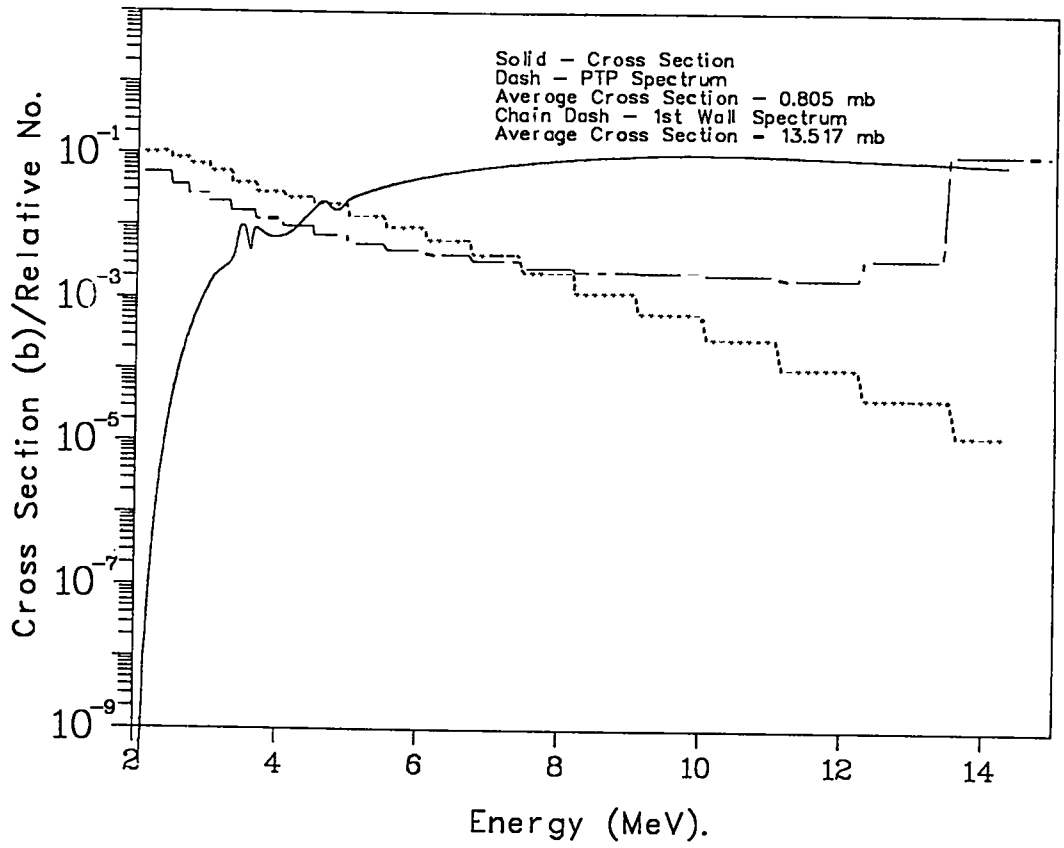

Fig. 80. Cross section for $^{27}Al(n,p)$ compared with the HFIR PTP and STARFIRE first wall spectra.

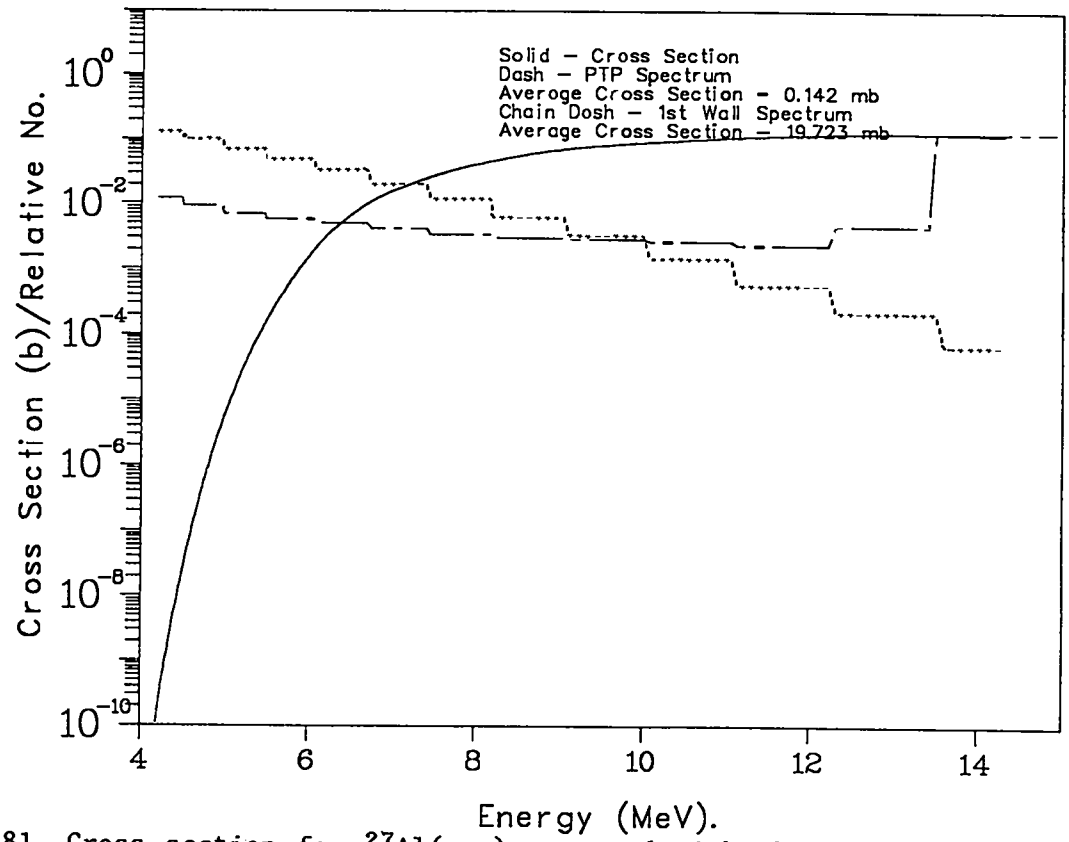

Fig. 81. Cross section for $^{27}Al(n,\alpha)$ compared with the STARFIRE first wall and HFIR PTP spectra.

REFERENCES

1. K. F. Liu, J. S. Zhang, and G. W. Shuy, "Comment on 'Fusion of Polarized Deuterons'," Phys. Rev. Lett. 55, 1649 (1985).

2. G. M. Hale and D. C. Dodder, "A=4 Level Structure from an R-Matrix Analysis of the Four-Nucleon System," B. Zeitnitz, Ed., Proc. 10th Int. Conf. Few Body Problems in Physics, Karlsruhe, West Germany, 1983 (North Holland Press, 1983), p. 207.

3. H. M. Hofmann and D. Fick, "Fusion of Polarized Deuterons," Phys. Rev. Lett. 52, 2038 (1984).

4. G. M. Hale, "Work on Polarized d+d Reactions Since the Madison Workshop," Los Alamos informal document LA-UR-2232 (1985).

5. B. P. Ad'yaseyich, V. G. Antonenko, and D. E. Fomenko, "Study of the Reactions $^{2}H(\vec{d},p)^{3}H$ and $^{2}H(\vec{d},n)^{3}He$ with a Polarized Deuteron Beam. Measurement of the Analyzing Power," Yad. Fiz. 33, 601 (1981) [Sov. J. Nucl. Phys. 33, 313 (1981)].

6. G. M. Hale, "R-Matrix Analysis of the ^{7}Li System with Peripheral Channel Overlap Exchange Effects," Proc. Int. Conf. on Nucl. Data for Basic and Applied Sci., Santa Fe, New Mexico, May 1985 (Gordon and Breach). (Proceedings to be published as well in Radiation Effects.)

7. F. M. Mann, "Transmutation of Alloys in MFE Facilities as Calculated by REAC," Hanford Engineering Development Laboratory report HEDL-TME 81-37 (1981).

8. P. G. Young and E. D. Arthur, "GNASH: A Preequilibrium-Statistical Nuclear Model Code for Calculations of Cross Sections and Emission Spectra," Los Alamos Scientific Laboratory report LA-6947 (November 1977).

9. M. Blann and J. Bisplinghoff, "Code ALICE/Livermore 1982," Lawrence Livermore National Laboratory report UCID 1914 (1982).

10. S. Pearlstein, "Neutron-Induced Reactions in Medium Mass Nuclei," Journal Nucl. Energy 27, 81 (1973).

11. J. B. Cumming, "Monitor Reactions for High Energy Proton Beams," Ann. Rev. Nucl. Sci. 13, 261 (1963).

12. R. E. MacFarlane and L. Stewart, "ENDF/B-VI Format Proposals," in Los Alamos National Laboratory report LA-10288-PR, "Applied Nuclear Science and Development Semiannual Progress Report October 1, 1983-May 31, 1984" (January 1985), p. 46.

13. E. D. Arthur, "Calculation of Neutron and Gamma-Ray Emission Spectra Produced by $p+^{27}Al$ Reactions," in Los Alamos National Laboratory report LA-10288-PR, "Applied Nuclear Science Research and Development Semiannual Progress Report October 1, 1983-May 31, 1984" (January 1985), p. 3.

14. D. Wilmore and P. E. Hodgson, "The Calculation of Neutron Cross Sections from Optical Potentials," Nucl. Phys. 55, 673 (1964).

15. W. F. McGill, R. F. Carlson, T. H. Short, J. M. Cameron, J. R. Richardson, I. Slaus, W. T. H. van Oers, J. W. Verba, D. J. Margaziotis, P. Doherty, "Measurements of the Proton Total Reaction Cross Section for Light Nuclei between 20 and 48 MeV," Phys. Rev. C 10, 2737 (1974).

16. C. M. Perey and F. G. Perey, "Deuteron Optical Model Analysis in the Range of 11 to 27 MeV," Phys. Rev. 132, 755 (1963).

17. C. M. Perey and F. G. Perey, "Compilation of Phenomenological Optical Model Parameters 1954-1975," Atomic Data and Nucl. Data Tables 17, 1 (1976).

18. G. M. Crawley and G. T. Garvey, "Inelastic Scattering in the 2s-1d Shell," Phys. Rev. 167, 1070 (1968).

19. S. M. Grimes, R. C. Haight, and J. D. Anderson, "Measurement of Sub-Coulomb Barrier Charged Particles Emitted from Aluminum and Titanium Bombarded by 15-MeV Neutrons," Nucl. Sci. Eng. 62, 187 (1977).

20. J. L. Kammerdiener, "Neutron Spectra Emitted by ^{239}Pu, ^{238}U, ^{235}U, Pb, Nb, Ni, Al, and C Irradiated by 14-MeV Neutrons," Lawrence Livermore National Laboratory report UCRL-51232 (1972).

21. G. Morgan, "Cross Sections for the Al(n,xn) and Al(n,xγ) Reactions between 1 and 20 MeV," Oak Ridge National Laboratory report TM-5241 (1976).

22. F. E. Bertrand and R. W. Peelle, "Tabulated Cross Section for Hydrogen and Helium Particles Produced by 62 and 29 MeV Protons on ^{27}Al," Oak Ridge National Laboratory report ORNL-4455 (1969).

23. E. D. Arthur and P. G. Young, "Evaluated Neutron Induced Cross Sections for ^{54,56}Fe to 40 MeV," Los Alamos Scientific Laboratory report LA-8626-MS (ENDF 304) (December 1980).

24. A. Prince, "Optical Model Calculations for the Chromium, Iron, and Nickel Isotopes in the Energy Range of 0.5 to 100 MeV," K. H. Böckhoff, Ed., Proc. Int. Conf. Nucl. Data for Sci. Technol., Antwerp, Belgium, September 6-10, 1982 (D. Reidel Publ. Co., Boston), p. 574.

25. G. S. Mani, "Spin Assignments to Excited States of ^{56}Fe Using Inelastic Proton Scattering," Nucl. Phys. A 165, 225 (1977).

26. S. M. Grimes, R. C. Haight, K. R. Alvar, H. H. Barschall, and R. R. Borchers, "Charged-Particle Emission in Reactions of 15-MeV Neutrons with Isotopes of Chromium, Iron, Nickel, and Copper," Phys. Rev. C 19, 2127 (1979).

27. F. E. Bertrand and R. W. Peelle, "Tabulated Cross Sections for Hydrogen and Helium Particles Produced by 62-MeV Protons on ^{56}Fe," Oak Ridge National Laboratory report ORNL-4456 (1969).

28. R. L. Clarke and W. G. Cross, "Elastic and Inelastic Scattering of 14.1-MeV Neutrons from Ni and Zr," Nucl. Phys. A 95, 320 (1967).

29. P. H. Stelson, R. L. Robinson, H. J. Kim, J. Rapaport, and G. R. Satchler, "Excitation of Collective States by the Inelastic Scattering of 14.1-MeV Neutrons," Nucl. Phys. 68, 97 (1965).

30. K. Dickens, "Gamma-Ray Production Due to Neutron Interactions with Nickel between 1 and 20 MeV," Oak Ridge National Laboratory ORNL-TM-4379 (1973).

31. S. Tanaka, M. Furukawa, M. Chiba, "Nuclear Reactions of Nickel with Protons up to 56 MeV," Journal Inorg. and Nucl. Chem 34, 2419 (1972).

32. Sheldon Kaufman, "Reactions of Protons with ^{58}Ni and ^{60}Ni," Phys. Rev. 117, 1532 (1960).

33. E. D. Arthur, "Calculation of Proton-Induced Reactions on Copper at E $\leq$ 50 MeV," in Los Alamos National Laboratory report LA-10513-PR, "Applied Nuclear Science Research and Development Progress Report June 1, 1984-May 31, 1985" (September 1985), p. 9.

34. J. C. Legg and J. L. Yntema, "Possible Spin Dependence in Proton Inelastic Scattering," Phys. Rev. Lett 22, 10055 (1969).

35. Y. Holler, A. Kaminsky, R. Langkan, W. Scobel, M. Trabandt, and R. Bonetti, "Precompound Emission in the Reaction ^{65}Cu(p,xn) and the Nucleon-Nucleon Scattering Mechanism," Nucl. Phys. A 442, 79 (1985).

36. E. D. Arthur and C. A. Philis, "New Calculations of Neutron Induced Cross Sections on Tungsten Isotopes," in Los Alamos National Laboratory report LA-8630-PR, "Applied Nuclear Data Research and Development July 1-September 30, 1980" (December 1980), p. 20.

37. A. M. Lane, "Isobaric Spin Dependence of the Optical Potential and Quasi-elastic (p,n) Reactions," Nucl. Phys. 35, 676 (1962).

38. J. Raynal, "Optical Model and Coupled-Channel Calculations in Nuclear Physics," International Atomic Energy Agency report IAEA SMR-9/8 (1970).

39. H. Marshak, A. Langsford, T. Tamura, and C. Y. Wong, "Total Neutron Cross Section of Oriented ^{165}Ho from 2 to 135 MeV," Phys. Rev. C 2, 1862 (1970).

40. T. Kruse, W. Maofske, H. Ogata, W. Savin, M. Slagowitz, M. Williams, P. Stoler, "Elastic and Inelastic Proton Scattering from Heavy Collective Nuclei," Nucl. Phys A 169, 177 (1971).

41. H. Kamitsubo, H. Ohnuma, K. Ono, A. Uchida, M. Shinohara, M. Imaizumi, S. Kobayashi, and M. Sekiguchi, "Elastic Scattering of 55-MeV Protons by Heavy Nuclei," Phys. Lett. 9, 332 (1964).

42. J. Frehaut and J. Jary, "Systematique des Sections Efficaces de Reactions (n,2n) pour des Series d'Isotopes Separes," Proc. Int. Conf. on Neutron and Nucl Data, Harwell, 1978, p. 1038.

43. E. D. Arthur, "Calculation of Neutron Cross Sections on Isotopes of Yttrium and Zirconium," Los Alamos Scientific Laboratory report LA-7789-MS (April 1979).

44. J. C. Dousse, E. D. Arthur, D. M. Drake, J. Gursky, J. D. Moses, N. Stein, and J. W. Sunier, "Coincident Neutron-Proton Emission from Proton Bombardment of ^{87}Sr and ^{91}Zr," Phys. Rev. C 32, 92 (1985).

45. P. Luksch and J. W. Tepel, "Nuclear Data Sheets for A = 87," Nucl. Data Sheets 27, 389 (1979).

46. E. D. Arthur, "Calculation of n+ ^{239}Pu Cross Sections up to Neutron Energies of 20 MeV," in Los Alamos National Laboratory report LA-9841-PR, "Applied Nuclear Data Research and Development Semiannual Progress Report October 1, 1982-March 31, 1983" (August 1983), p. 15.

47. J. Frehaut, A. Bertin, R. Bois, E. Grytakis, C. A. Philis, "(n,2n) Cross Sections of ^{2}H and ^{239}Pu," Proc. Int. Conf. on Nucl. Data for Basic and Applied Sci., Santa Fe, New Mexico, May 1985 (Gordon and Breach), (Proceedings to be published as well in Radiation Effects.)

48. E. D. Arthur, "Improved (n,f) Cross Sections Using Measured Fission Probabilities," Trans. Am. Nucl. Soc. 46, 739 (1984).

49. P. G. Young, "Global and Local Optical Model Parameterizations," Proc. OECD, NEANDC Specialists Meeting on the Use of the Optical Model for the Calculation of Neutron Cross Sections Below 20 MeV, Paris, November 13-15, 1985, to be issued.

50. P. A. Moldauer, "Optical Model of Low Energy Neutron Interactions with Spherical Nuclei," Nucl. Phys. 47, 65 (1963).

51. F. G. Perey and B. Buck, "A Non-Local Potential Model for the Scattering of Neutrons by Nuclei," Nucl. Phys. 32, 353 (1962).

52. C. A. Engelbrecht and H. Fiedeldey, "Nonlocal Potentials and the Energy Dependence of the Optical Model for Neutrons," Ann. Phys. 42, 262 (1967).

53. F. D. Becchetti, Jr., and G. W. Greenlees, "Nucleon-Nucleus Optical-Model Parameters, A > 40, E < 50 MeV," Phys. Rev. 182, 1190 (1969).

54. D. M. Patterson, R. R. Doering, and A. Galonsky, "An Energy-Dependent Lane-Model Nucleon-Nucleus Optical Potential," Nucl. Phys. A 263, 261 (1976).

55. J. Rapaport, V. Kulkarni, and R. W. Finlay, "A Global Optical-Model Analysis of Neutron Elastic Scattering Data," Nucl. Phys. A 330, 15 (1979).

56. R. L. Walter and P. P. Guss, "A Global Optical Model for Neutron Scattering for A>53 and 10 MeV<E<80 MeV," Proc. Int. Conf. Nucl. Data for Basic and Applied Sci., Santa Fe, New Mexico, May 1985 (Gordon and Breach), (Proceedings to be published as well in Radiation Effects.)

57. S. F. Mughabghab, M. Divadeenam, N. E. Holden, "Neutron Resonance Parameters and Thermal Cross Sections," Neutron Cross Sections, Vol. 1, Academic Press, New York (Part A-1981), (Part B-1984).

58. O. Bersillon, "SCAT2: Un Programme de Modele Optique Spherique," in Commissariat a l'Energie Atomique report CEA-N-2227 (1981).

59. Experimental data provided from CSISRS compilation by the National Nuclear Data Center, Brookhaven National Laboratory, Upton, New York.

60. M. Kawai, presented at NEANDC Topical Discussions, Geel, September 1979; see also Y. K. Kuchi and N. Sekine, "Evaluation of Neutron Nuclear Data of Natural Nickel and Its Isotopes," J. Nucl. Sci. Tech. 22, 337 (1985).

61. S. Igarasi et al., "Evaluation of Fission Product Nuclear Data for Fast Reactors," Japanese Atomic Energy Research Institute report JAERI-M 5752 (1974).

62. D. G. Madland and P. G. Young, "Neutron-Nucleus Optical Potential for the Actinide Region," Proc. Int. Conf. on Neutron Physics and Nuclear Data for Reactors and Other Applied Purposes, Harwell, published by OECD, p. 349.

63. C. L. Dunford, "A Unified Model for Analysis of Compound Nuclear Reactions," Atomics International report AI-AEC-12931 (1970).

64. A. Gilbert and A. G. W. Cameron, Can. J. Phys. 43, 1446 (1965).

65. J. L. Cook, H. Ferguson, and A. R. Musgrove, "Nuclear Level Densities in Intermediate and Heavy Nuclei," Aust. J. Phys. 20, 477 (1967).

66. R. C. Harper and W. L. Alford, "Experimental and Theoretical Neutron Cross Sections at 14-MeV," J. Phys. G: Nucl. Phys. 8, 153 (1982).

67. P. P. Guss, R. C. Byrd, C. E. Floyd, C. R. Howell, K. Murphy, G. Tungate, R. S. Pedroni, R. L. Walter, J. P. Delaroche, and T. B. Clegg, "Cross Sections and Analyzing Powers for Fast-Neutron Scattering to the Ground and First Excited States of ^{58}Ni and ^{60}Ni," Nucl. Phys. A 438, 187 (1985).

68. B. Strohmaier, M. Uhl, and W. Reiter, "Neutron Cross Section Calculations for ^{52}Cr, ^{55}Mn, ^{56}Fe, and ^{58,60}Ni for Incident Energies to 30 MeV," IAEA Advisory Group Meeting on Nuclear Data for Radiation Damage Assessment and Related Safety Aspects, Vienna, October 1981.

69. R. E. Shamu, E. M. Bernstein, J. J. Ramirez, and Ch. Lagrange, "Effects of Deformation on Neutron Total Cross Sections of Even-A Nd and Sm Isotopes," Phys. Rev. C 22, 1857 (1980).

70. E. D. Arthur, P. G. Young, A. B. Smith, and C. A. Philis, "New Tungsten Isotope Evaluations for Neutron Energies Between 0.1 and 20 MeV," Trans. Am. Nucl. Soc. 39, 793 (1981).

71. J. P. Delaroche, G. Haouat, J. Lachkar, Y. Patin, J. Sigaud, and J. Hardine, "Deformations, Moments, and Radii of ^{182,183,184,186}W from Fast Neutron Scattering," Phys. Rev. C 23, 136 (1981).

72. P. G. Young, E. D. Arthur, C. Philis, P. Nagel, M. Collin, "Analysis of n+^{165}Ho and ^{169}Tm Reactions," Proc. Nucl. Data for Sci. and Tech. Int. Conf., Antwerp, Belgium, September 1982, p. 792.

73. G. Haouat, J. Lachkar, Ch. Lagrange, J. Jary, J. Sigaud, and Y. Patin, "Neutron Scattering Cross Sections for ^{232}Th, ^{233}U, ^{235}U, ^{238}U, ^{239}Pu, and ^{242}Pu Between 0.6 and 3.4 MeV," Nucl. Sci. Eng. 81, 491 (1982).

74. Ch. Lagrange, "Results of Coupled Channel Calculations for the Neutron Cross Sections of a Set of Actinide Nuclei," NEANDC(E) 228 <L>, October 1982.

75. Ch. Lagrange, O. Bersillon, and D. G. Madland, "Coupled Channel Optical-Model Calculations for Evaluating Neutron Cross Sections of Odd-Mass Actinides," Nucl. Sci. Eng. 83, 396 (1983).

76. S. Joly, D. Drake, and L. Nilsson, "Gamma-ray Strength Functions for ^{104}Rh, ^{170}Tm, and ^{198}Au," Phys. Rev. C 20, 2072 (1979).

77. M. A. Lone, "Photon Strength Functions," in Proc. Third Int. Symp. Neutron Capture Gamma-Ray Spectroscopy and Related Topics, Brookhaven National Laboratory and State Univ. of New York, September 18-22, 1978, R. E. Chrien, Ed. (Plenum Press, New York, 1979), p. 161.

78. V. J. Orphan, N. C. Rasmussen, and T. L. Harper, "Line and Continuum Gamma-Ray Yields from Thermal-Neutron Capture in 75 Elements," Gulf General Atomic report GA-10248 (1970).

79. C. Kalbach and F. M. Mann, "Phenomenology of Continuum Angular Distributions I. Systematics and Parameterization," Phys. Rev. C 23, 112 (1981).

80. A. Bohr and B. R. Mottelson, Nuclear Structure, Vol. II (W. A. Benjamin, Inc., New York, 1975), p. 201.

81. C. Michael Lederer and Virginia Shirley, Eds., Table of Isotopes, Seventh Edition (John Wiley and Sons, Inc., New York, 1978).

82. D. G. Madland, "Search for a Suitable Isomer for the GRASER Program," in Los Alamos National Laboratory report LA-10288-PR, "Applied Nuclear Science Research and Development Semiannual Progress Report October 1, 1983-May 31, 1984" (January 1985), p. 26.

83. D. Strottman, E. D. Arthur, and D. G. Madland, "Nuclear Structure Considerations for Gamma-Ray Lasers," Los Alamos National Laboratory informal document LA-UR-85-2701 (May 1985).

84. R. J. Howerton, "ENSL82 and CDRL82: The 1982 Version of Evaluated Nuclear Structure Libraries ENSL and CDRL," Lawrence Livermore National Laboratory report UCRL-50400 Vol 23. Addendum (1983).

85. Evaluated Nuclear Structure Data File, Version V, available from the National Nuclear Data Center, Brookhaven National Laboratory, Upton, New York.

86. C. J. Gallagher, Jr., and S. A. Moszkowski, "Coupling of Angular Momenta in Odd-Odd Nuclei," Phys. Rev. 111, 1282 (1958).

87. N. D. Newby, Jr., "Selection Rules in the Odd-Even Shift of Certain Nuclear Rotational Bands," Phys. Rev. 125, 2063 (1962).

88. J. Grundl and C. Eisenhauer, "Fission Rate Measurements for Materials Neutron Dosimetry in Reactor Environments," Proc. First ASTM-EURATOM Symp on Reactor Dosimetry, Petten, Holland, Sept. 22-26, 1975, Part I, p. 425.

89. D. G. Madland and J. R. Nix, "New Calculation of Prompt Fission Neutron Spectra and Average Prompt Neutron Multiplicities," Nucl. Sci. Eng. 81, 213 (1982).

90. W. P. Poenitz and T. Tamura, "Investigation of the Prompt-Neutron Spectrum for Spontaneously-Fissioning ^{252}Cf," Proc. Int. Conf. on Nuclear Data for Science and Technology, Antwerp, Belgium, 1982, Reidel, Dordrecht (1983), p. 465.

91. J. W. Boldeman, B. E. Clancy, and D. Culley, "Measurements of the Prompt Fission Neutron Spectrum from the Spontaneous Fission of ^{252}Cf," submitted to Nucl. Sci. Eng. (November 1984).

92. J. Grundl, D. Gilliam, D. McHarry, C. Eisenhauer, and P. Soran, in memorandum to Cross Section Evaluation Working Group (CSEWG) Subcom. on Standards (May 1983).

93. K. Kobayashi, I. Kimura, H. Gotoh, and H. Tominaga, "Measurement of Average Cross Sections for Some Threshold Reactions of Ti, Cr, and Pb in the Californium-252 Spontaneous Fission Neutron Spectrum Field," Annual Reports of the Research Reactor Institute, Kyoto University, Vo. 17, p. 15-21, 1984 (unpublished).

94. D. G. Madland, R. J. LaBauve, and J. R. Nix, "Comparisons of Four Representations of the Prompt Neutron Spectrum for the Spontaneous Fission of ^{252}Cf," Proc. Int. Conf. on Nuclear Data for Basic and Applied Sci., Santa Fe, New Mexico, May 1985 (Gordon and Breach).

95. D. G. Foster, Jr., and R. E. MacFarlane, "Coupled Energy-Angle Distributions of Recoiling Nuclei," in Los Alamos National Laboratory report LA-10288-PR, "Applied Nuclear Science Research and Development Semiannual Progress Report October 1, 1983-May 31, 1984" (January 1985), p. 36.

96. R. E. MacFarlane and D. G. Foster, Jr., "Advanced Nuclear Data for Radiation Damage Calculations," Jour. Nucl. Mat. 122 and 123, 1047 (1984).

97. D. W. Muir, "Calculation of ^{59}Co Cross Sections using GNASH and Comparison with Previously Published Results," pp. 5-6 in "Nuclear Physics Theoretical Group Report No. 50, Progress Report for the Period May 1984 to May 1985," Oxford University Nuclear Physics Laboratory report 39/85 (June 1985).

98. D. W. Muir, "Implementation of GNASH and Auxiliary Codes on the Harwell CRAY-1," Atomic Energy Research Establishment, Harwell, report AERE R 11877 (July 1985).

99. C. Kalbach, "PRECO-B: Programme for Calculating Preequilibrium Particle Spectra" (unpublished). See also C. Kalbach, "The Griffin Model, Complex Particles, and Direct Nuclear Reactions," Z. Phys. A283, 401 (1977).

100. R. E. MacFarlane, D. W. Muir, and R. M. Boicourt, "The NJOY Nuclear Data Processing System Volume I: User's Manual," Los Alamos National Laboratory report LA-9303-M, Vol. I (ENDF-324)(May 1982).

101. R. E. MacFarlane and D. W. Muir, "The NJOY Nuclear Data Processing System, Volume III: The GROUPR, GAMINR, and MODER Modules," Los Alamos National Laboratory report LA-9303, Vol. III (ENDF-324) (to be published in 1986).

102. D. W. Muir, R. E. MacFarlane, "The NJOY Nuclear Data Processing System, Volume IV: The ERRORR and COVR Modules," Los Alamos National Laboratory report LA-9303-M, Vol. IV (ENDF-324) (December 1985).

103. R. W. Roussin, J. R. Knight, J. H. Hubbell, and R. J. Howerton, "Description of the DLC-99/HUGO Package of Photon Interaction Data in ENDF/B-V Format," Oak Ridge National Laboratory report ORNL/RSIC-46 (ENDF-335) (December 1983).

104. J. V. Koppel and D. H. Houston, "Reference Manual for ENDF Thermal Neutron Scattering Data," General Atomics report GA-8774, revised and reissued as ENDF-269 (July 1978).

105. T. R. England and B. F. Rider, "Status of Fission Yield Evaluations," R. E. Chrien and T. W. Burrows, Eds., Proc. NEANDC Specialists Meet. on Yields and Decay Data for Fission Product Nuclides, Brookhaven National Laboratory, Upton, New York, October 24-27, 1983 (Brookhaven National Laboratory report BNL 51778).

106. K. -L. Kratz and G. Herrmann, "Systematics of Neutron Emission Probabilities from Delayed Neutron Precursors," Z. Physik 263, pp. 435-442 (1973).

107. F. M. Mann, M. Schreiber, R. E. Schenter, and T. R. England, "Evaluation of Delayed Neutron Emission Probabilities," Nucl. Scie. Eng. 87, pp. 418-431 (August 1984).

108. T. R. England, W. B. Wilson, R. E. Schenter, and F. M. Mann, "Aggregate Delayed Neutron Intensities and Spectra Using Augmented ENDF/B-V Precursor Data," Nucl. Sci. Eng. 62, pp. 139-155 (October 1983).

109. T. R. England, W. B. Wilson, R. E. Schenter, and F. M. Mann, "ENDF/B-V Summary Data for Fission Products and Actinides," Electric Power Research Institute report NP-3787 (ENDF-332)(December 1984).

110. G. Rudstam, "Six-Group Representation of the Energy Spectra of Delayed Neutrons from Fission," Nucl. Sci. Eng. 80, 238-255 (February 1982).

111. K. -L. Kratz, "Review of Delayed Neutron Spectra," Proc. Consultants Meeting on Delayed Neutron Properties, Vienna, Austria, March 26-30, 1979 [International Atomic Energy Agency report INDC (NDS-107/G + Special) (1979)].

112. F. M. Mann, C. Dunn, and R. E. Schenter, "Beta Decay Properties from a Statistical Model," Trans. Am. Nucl. Soc. 39, 880 (1980). [See also Phys. Rev. C 1, 524 (January 1982).]

113. A. H. Wapstra and G. Audi, "The 1983 Atomic Mass Table," Nucl. Phys. A 432, No. 1 (January 7, 1985).

114. P. Möller and J. R. Nix, "Atomic Masses and Nuclear Ground-State Deformations Calculated with a New Macroscopic-Microscopic Model," Atomic Data and Nuclear Data Tables 26, No. 2, pp. 165-196 (March 1981).

115. R. C. Greenwood and A. J. Caffrey, "Delayed-Neutron Energy Spectra of ^{93,97}Rb and ^{143,145}Cs," Nucl. Sci. Eng. 91, pp. 305-323 (1985).

116. P. L. Reeder, L. J. Alquist, R. L. Kiefer, F. H. Ruddy, and R. A. Warner, "Energy Spectra of Delayed Neutrons from the Separated Precursors Rubidium-93, -94, -95, and Cesium-143," Nucl. Sci. Eng. 75, pp. 140-150 (1980).

117. Sequence of annual progress reports from the Institute for Chemistry, University of Mainz, Germany, 1973-1984.

118. R. A. Warner and P. L. Reeder, "Delayed Neutron Data from TRISTAN," Proc. Int. Conf. on Nucl. Data for Basic and Applied Sci., Santa Fe, New Mexico, May 1985 (Gordon and Breach).

119. T. R. England, R. Wilczynski, and N. L. Whittemore, "CINDER-7: An Interim Report for Users," Los Alamos Scientific Laboratory report LA-5885-MS (April 1975). (CINDER-10 is a major modification of CINDER-7, but is documented only in a series of T-2 progress reports.)

120. A. Sierk, Los Alamos National Laboratory memorandum, T-9, September 24, 1985, to T. England and E. Arthur; subject: Delayed Neutron Spectra.

121. D. G. Madland and T. R. England, "The Influence of Pairing on the Distribution of Independent Yield Strengths in Neutron-Induced Fission," Los Alamos Scientific Laboratory report LA-6430-MS (July 1976).

122. R. L. Walker, "The (α,n) Cross Section of Boron," Phys. Rev. 76, 244 (1949).

123. W. B. Wilson, R. T. Perry, J. E. Stewart, T. R. England, D. G. Madland, and E. D. Arthur, "Development of the SOURCES Code and Data Library for the Calculation of Neutron Sources and Spectra from the (α,n) Reactions, Spontaneous Fission, and β^- Delayed Neutrons," in Los Alamos National Laboratory report LA-9841-PR, "Applied Nuclear Data Research and Development Semi-annual Progress Report October 1, 1982-March 31, 1983" (August 1983), pp. 65-66.

124. R. T. Perry and W. B. Wilson, "On the (α,n) Neutron Production in Boron Containing Systems," Trans. Am. Nucl. Soc. 46, 763 (1984).

125. J. K. Bair and J. G. del Campo, "Neutron Yields from Alpha-Particle Bombardment," Nucl. Sci. Eng. 71, 18 (1979).

126. G. V. Gorshkov, V. A. Zyabkin, and O. S. Tsvetkov, "Neutron Yields from the Reaction (α,n) in Be, B, C, O, F, Mg, Al, Si, and Granite Irradiated with Polonium α Particles," Atomnaya Energiya 13, 65 (1962) (p. 654 of English translation).

127. J. H. Roberts, "Neutron Yields of Several Light Elements Bombarded with Polonium Alpha Particles," US Atomic Energy Commission report MDDC-731 (1944).

128. B. H. Weren and J. E. Faulkner, "(α,n) Neutron Source in Commercial High-Level Waste," Trans. Am. Nucl. Soc. 45, 608 (1983).

129. P. G. Young and D. G. Foster, Jr., "An Evaluation of the Neutron and Gamma-Ray Production Cross Sections from Nitrogen," Los Alamos Scientific Laboratory report LA-4725 (ENDF-173) (September 1972).

130. J. F. Ziegler, Helium Stopping Powers and Ranges in All Elemental Matter, Vol. 4 of The Stopping and Ranges of Ions in Matter series (Pergamon Press, New York, 1977).

131. R. T. Lancet, J. C. Mills, "SAFR: A Marriage of Safety and Innovation in LMR Design," Tran. Am. Nucl. Soc. 50 (TANSAO 50 1-644), p. 336 (1985).

132. R. Kinsey, Comp., "ENDF-201: ENDF/B Summary Documentation," Brookhaven National Laboratory report BNL-NCS17541 (ENDF-201), 3rd Ed. ENDF/B-V (1979).

133. R. E. MacFarlane, "TRANSX-CTR: A Code for Interfacing MATXS Cross Section Libraries to Nuclear Transport Codes for Fusion System Analysis," Los Alamos National Laboratory report LA-9863-MS (February 1984).

134. R. D. O'Dell, "Standard Interface Files and Procedures for Reactor Physics Codes, Version II," Los Alamos Scientific Laboratory report LA-6941-MS (September 1977).

135. K. L. Derstine, "DIF3D: A Code to Solve One-, Two-, and Three-Dimensional Finite-Difference Diffusion Theory Problems," Argonne National Laboratory report ANL-82-64 (April 1982).

136. F. M. Mann, "Transmutations of Alloys in MFE Facilities as Calculated by REAC," Hanford Engineering Development Laboratory report HEDL-TME 81-37 (August 1982).

Printed in the United States of America
Available from
National Technical Information Service
US Department of Commerce
5285 Port Royal Road
Springfield, VA 22161
Microfiche (A01)

Page Range	NTIS Price Code	Page Range	NTIS Price Code	Page Range	NTIS Price Code	Page Range	NTIS Price Code
001-025	A02	151-175	A08	301-325	A14	451-475	A20
026-050	A03	176-200	A09	326-350	A15	476-500	A21
051-075	A04	201-225	A10	351-375	A16	501-525	A22
076-100	A05	226-250	A11	376-400	A17	526-550	A23
101-125	A06	251-275	A12	401-425	A18	551-575	A24
126-150	A07	276-300	A13	426-450	A19	576-600	A25
						601-up*	A99

*Contact NTIS for a price quote.

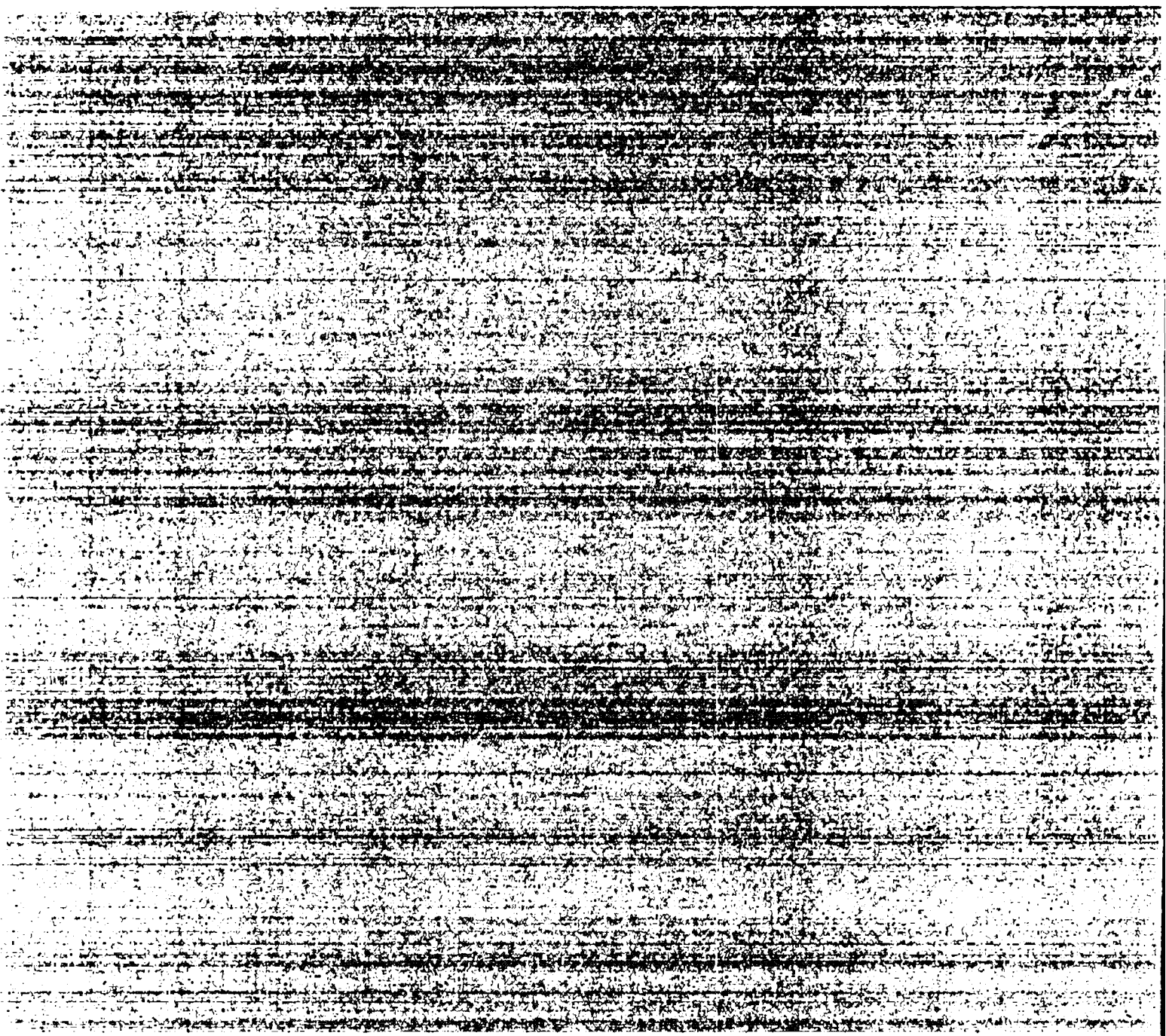

Los Alamos